Hyperreactive B cells instruct their elimination by T cells to curb autoinflammation and lymphomagenesis

Diehl, Carina; Soberón, Valeria; Baygün, Seren; Chu, Yuanyuan; Mandelbaum, Jonathan; Kraus, Laura; Engleitner, Thomas; Rudelius, Martina; Fangazio, Marco; Daniel, Christoph; ...

Source / Izvornik: **Immunity, 2025, 58, 124 - 142.**

Journal article, Published version
Rad u časopisu, Objavljena verzija rada (izdavačev PDF)

https://doi.org/10.1016/j.immuni.2024.11.023

Permanent link / Trajna poveznica: https://urn.nsk.hr/urn:nbn:hr:184:719667

Article

Immunity

Hyperreactive B cells instruct their elimination by T cells to curb autoinflammation and lymphomagenesis

Graphical abstract

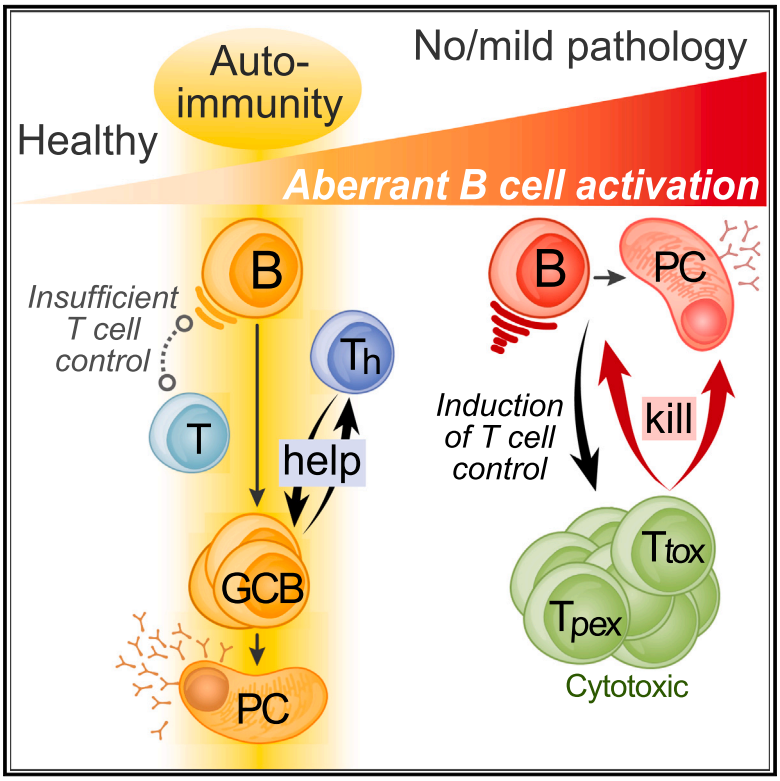

Authors

Carina Diehl, Valeria Soberón, Seren Baygün, ..., Laura Pasqualucci, Oliver Weigert, Marc Schmidt-Supprian

Correspondence

marc.supprian@tum.de

In brief

Aberrant immune signal strength in B cells is associated with autoimmune diseases and lymphoma. Diehl et al. show that hyperreactive B cells trigger cytotoxic T cell-mediated elimination. Less reactive B cells escape this tolerance mechanism, revealing a narrow reactivity window for the emergence of autoimmunity.

Highlights

- Mildly hyperreactive B cells (B-A20$^{+/-}$) drive lethal female sex-biased autoimmunity
- Strong hyperreactivity (B-A20$^{-/-}$ with BAFF, BCLxL, or NIK gain) causes mild disorders
- Hyperreactive B cells induce cytotoxic T cells and stem-like Tpex cells
- Lack of T cells reveals B cell-intrinsic lymphoproliferative and oncogenic potentials

Diehl et al., 2025, Immunity *58*, 124–142
January 14, 2025
https://doi.org/10.1016/j.immuni.2024.11.023

CellPress

CellPress
OPEN ACCESS

Immunity

Article

Hyperreactive B cells instruct their elimination by T cells to curb autoinflammation and lymphomagenesis

Carina Diehl,[1,2,20] Valeria Soberón,[1,2,3,4,20] Seren Baygün,[1,2,3,20] Yuanyuan Chu,[1,4,20] Jonathan Mandelbaum,[5] Laura Kraus,[1,2] Thomas Engleitner,[2,3,6] Martina Rudelius,[7] Marco Fangazio,[5] Christoph Daniel,[8] Sabrina Bortoluzzi,[1,2] Sabine Helmrath,[1,2] Pankaj Singroul,[1,2] Vanessa Gölling,[1,2] Francisco Osorio Barrios,[1,2] Gönül Seyhan,[1,2] Lena Oßwald,[1,2,9] Maike Kober-Hasslacher,[1,4] Theodor Zeng,[1,2] Rupert Öllinger,[2,3,6] Ali M. Afzali,[10] Thomas Korn,[10] Mohsen Honarpisheh,[11] Maciej Lech,[11] Qurrat Ul Ain,[12] Joachim Pircher,[12,13] Vanna Imširović,[14] Vedrana Jelenčić,[14] Felix M. Wensveen,[14] Verena Passerini,[15] Stefanie Bärthel,[2,3,16] Govind Bhagat,[17] David Dominguez-Sola,[18] Dieter Saur,[2,3,16] Katja Steiger,[3,19] Roland Rad,[2,3,6] Laura Pasqualucci,[5,17] Oliver Weigert,[3,15] and Marc Schmidt-Supprian[1,2,3,4,21,*]

[1]Institute of Experimental Hematology, School of Medicine, Technical University of Munich, 81675 Munich, Germany
[2]Center for Translational Cancer Research (TranslaTUM), School of Medicine, Technical University of Munich, 81675 Munich, Germany
[3]German Cancer Consortium (DKTK), 69120 Heidelberg, Germany
[4]Max-Planck Institute of Biochemistry, 82152 Planegg, Germany
[5]Institute for Cancer Genetics, Department of Pathology and Cell Biology, Columbia University, New York, NY 10032, USA
[6]Institute of Molecular Oncology and Functional Genomics, School of Medicine, Technical University of Munich, 81675 Munich, Germany
[7]Institute of Pathology, Faculty of Medicine, Ludwig-Maximilians-University, 80337 Munich, Germany
[8]Department of Nephropathology, Faculty of Medicine, Friedrich-Alexander University (FAU) Erlangen-Nuremberg, 91054 Erlangen, Germany
[9]Department of Medicine III, School of Medicine, Technical University of Munich, 81675 Munich, Germany
[10]Institute for Experimental Neuroimmunology, Department of Neurology, School of Medicine, Technical University of Munich, 81675 Munich, Germany
[11]Renal Division, Department of Medicine IV, Faculty of Medicine, Ludwig-Maximilians-University, 80336 Munich, Germany
[12]Department of Medicine I, Faculty of Medicine, Ludwig-Maximilians-University, 81377 Munich, Germany
[13]Partner site Munich Heart Alliance, DZHK (German Centre for Cardiovascular Research), 80802 Munich, Germany
[14]Department of Histology and Embryology, Faculty of Medicine, University of Rijeka, 51000 Rijeka, Croatia
[15]Laboratory for Experimental Leukemia and Lymphoma Research (ELLF), Faculty of Medicine, Department of Medicine III, Ludwig-Maximilians-University, 81377 Munich, Germany
[16]Chair of Translational Cancer Research and Institute of Experimental Cancer Therapy, School of Medicine, Technical University of Munich, 81675 Munich, Germany
[17]Herbert Irving Comprehensive Cancer Center, Columbia University, New York, NY 10032, USA
[18]Departments of Oncological Sciences and Pathology, Tisch Cancer Institute, Lipschultz Precision Immunology Institute, Graduate School of Biomedical Sciences, Icahn School of Medicine at Mount Sinai, New York, NY 10029, USA
[19]Institute of Pathology, School of Medicine, Technical University of Munich, 81675 Munich, Germany
[20]These authors contributed equally
[21]Lead contact
*Correspondence: marc.supprian@tum.de
https://doi.org/10.1016/j.immuni.2024.11.023

SUMMARY

B cell immunity carries the inherent risk of deviating into autoimmunity and malignancy, which are both strongly associated with genetic variants or alterations that increase immune signaling. Here, we investigated the interplay of autoimmunity and lymphoma risk factors centered around the archetypal negative immune regulator *TNFAIP3*/A20 in mice. Counterintuitively, B cells with moderately elevated sensitivity to stimulation caused fatal autoimmune pathology, while those with high sensitivity did not. We resolved this apparent paradox by identifying a rheostat-like cytotoxic T cell checkpoint. Cytotoxicity was instructed by and directed against B cells with high intrinsic hyperresponsiveness, while less reactive cells were spared. Removing T cell control restored a linear relationship between intrinsic B cell reactivity and lethal lymphoproliferation, lymphomagenesis, and autoinflammation. We thus identify powerful T cell-mediated negative feedback control of inherited and acquired B cell pathogenicity and define a permissive window for autoimmunity to emerge.

INTRODUCTION

Up to five percent of the general population develops autoimmune diseases worldwide, and the incidence is rising. Lymphocytes can accumulate thousands of somatic mutations as individuals age.[1,2] This steadily increases the likelihood of disease development, especially when somatic mutations and germline variants affect the same gene or pathway.[3–5] B cells are at especially high risk of acquiring somatic alterations due to developmentally programmed DNA breaks and tremendous proliferation during clonal expansion in the germinal center (GC). Together with preexisting susceptibilities and epigenetic changes, acquired alterations can contribute to autoimmunity and cause lymphomas, the most prevalent form of blood cancer. Often, such alterations cause enhanced immune signals.[6–8] Consistent with the fact that patients with B cell-mediated autoimmune diseases carry an increased risk to develop lymphoma,[9] mutations in autoreactive B cells can resemble mutations frequently found in malignant B cells.[10,11] Together, accumulated inherited predispositions, acquired mutations, and epigenetic reprogramming are thought to progressively cause the breakdown or evasion of several checkpoints in both disease spectra.[7] How the immune system reacts to this dynamic genetic and epigenetic variability remains a fundamental question. T cells can play complex and sometimes opposing roles in B cell-mediated pathologies by either providing help[12,13] or promoting immune surveillance.[14–16] The factors tilting the balance between pathogenic and protective T cell responses remain incompletely understood.

To study the consequences of B cell hyperreactivity in these complex related immune pathologies, we employed deficiency for the key negative feedback regulator of immune signals, tumor necrosis factor alpha-induced protein 3 (*TNFAIP3*/A20). A20 restricts prolonged ubiquitin-mediated signaling[17,18] downstream of key B cell activating modules—namely, Toll-like receptors (TLRs), CD40, and antigen receptors. Alterations reducing A20 expression and functions are prominently associated with both human autoimmunity and lymphoma.[18–24] However, A20 ablation in B lymphocytes induced only mild autoimmune phenotypes in aged mice,[25–27] and its role during lymphomagenesis is unresolved. We therefore combined mono- (modest hyperreactivity *in vitro*) and bi-allelic (strong hyperreactivity *in vitro*)[25–27] A20 deficiency in B cells with additional prototypical autoimmune and lymphoma-predisposing events. Paradoxically, modest B cell hyperactivation caused lethal disease, faithfully recapitulating human autoimmune pathology, whereas strong B cell hyperreactivity had substantially less or even protective effects. This was due to the differential induction of, and/or increased susceptibility to, potent cytotoxic T cell responses. Thus, T cell-mediated negative feedback control of B cell activation emerges as a central factor balancing protective against pathologic functions in B cell immunity.

RESULTS

Loss of A20 in GCB cells or all B cells is insufficient to cause lymphomagenesis

TNFAIP3/A20 inactivating alterations are prevalent in human lymphoma, including diffuse large B cell lymphoma (DLBCL)[19,21] and marginal zone lymphoma.[20] However, validation of A20 as a tumor suppressor in lymphoma is lacking. To this end, we generated mice in which *Tnfaip3*/A20 is ablated specifically in germinal center B (GCB) cells—the cell of origin of most B cell lymphomas—using a conditional A20 allele ($A20^{F}$) and *Cγ1Cre* mice (GCB-A20$^{-/-}$ refers to *Cγ1Cre* $A20^{F/F}$, and GCB-A20$^{wt/-}$ refers to *Cγ1Cre* $A20^{wt/F}$, and in the following, deficiency refers to both mono- and bi-allelic loss). To test whether A20 ablation synergizes with other genetic alterations associated with A20 loss in human lymphoma,[28] we also included a Bcl6-transgene (*IμHABCL6* = Bcl6^{tg}), which causes the development of GC-derived lymphomas that share features of the human disease.[29] Mice were evaluated for immune responses to the T cell-dependent antigen sheep red blood cells (SRBCs) and for lymphomagenesis under repeated antigenic stimulation.[29]

10 days after SRBC immunization, both heterozygous and homozygous ablation of A20 in GCB cells led to elevated plasma cell production, but only heterozygous loss increased GCB cells (Figure S1A). BCL6 overexpression impaired plasma cell generation as reported,[29] and A20 deficiency showed a trend toward enhanced GCB cell production in Bcl6^{tg} mice (Figure S1B). However, we did not detect significant effects of GCB cell-specific A20 deficiency on the event-free survival of mice and the occurrence of lymphomas in the presence and absence of the Bcl6^{tg}, as determined by phenotypic, immunohistochemical, and clonality analyses (Figures 1A–1C, S1D, and S1E).

A20 deficiency in lymphoma can also occur at earlier stages of B cell development, as exemplified by the association of lymphoma complicating primary Sjögren's syndrome (SjS) with a germline hypomorphic *TNFAIP3*/A20 coding variant.[3,30] Ablation of A20 in all B cells (in *CD19Cre* $A20^{F/F}$ = B-A20$^{-/-}$ mice) shortened the lifespan of mice, but heterozygous loss (in *CD19Cre* $A20^{wt/F}$ = B-A20$^{wt/-}$ mice) had an even stronger effect (Figure 1D). Histopathological examination of mice showing signs of illness or taken for analysis at over 80 weeks of age revealed marginal zone B cell hyperplasia, plasmacytosis, and polyclonal lymphoproliferations in B-A20$^{-/-}$ and B-A20$^{wt/-}$ mice (Figures 1E and S1F). However, clonality analyses by Southern blot and amplicon sequencing did not uncover significantly more (mutated) B cell clones compared with control mice (Figure S1H; Table S2). Most frequently, B cell-specific A20 deficiency led to T cell hyperplasia and extramedullary hematopoiesis (Figures 1E and S1G).

Therefore, mono- or bi-allelic loss of A20 in mouse B or GCB cells was not sufficient to cause overt lymphomagenesis or to accelerate the development of lymphomas driven by deregulated Bcl6 expression.

B cell-specific A20 haploinsufficiency, but not its complete absence, causes female sex-biased autoimmune disease

As lymphomagenesis could not explain the increased mortality of B cell-specific A20-deficient mice, we considered autoimmunity as the underlying cause. Given the strong female sex bias in human autoimmune diseases,[31] we stratified the survival of our mouse cohort by sex, revealing reduced life expectancy in female compared with male B-A20$^{wt/-}$ mice but no sex bias in the other groups (Figures 1F and S1I). Analysis of aged mice (>17 months) revealed that female B-A20$^{wt/-}$ mice were

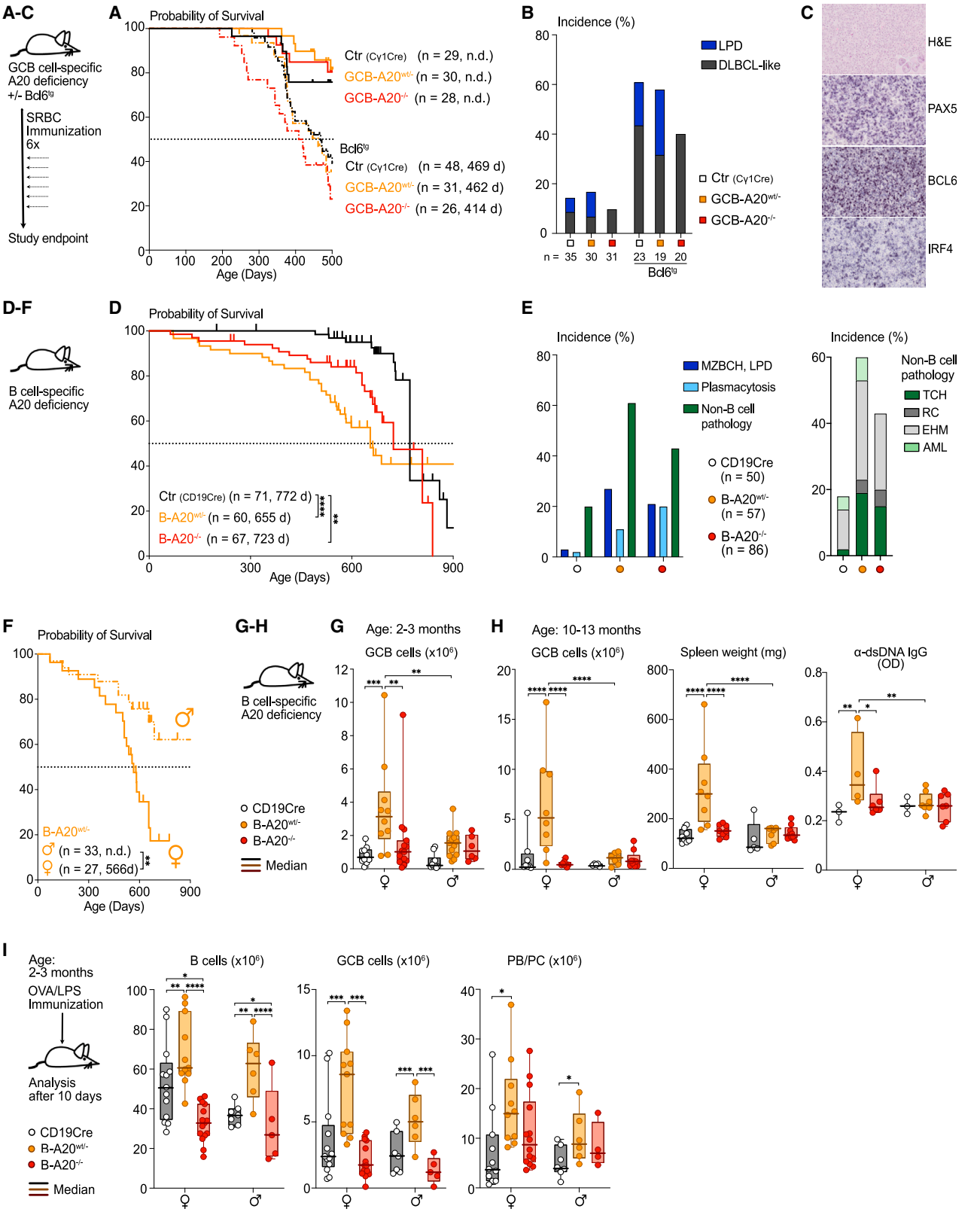

Figure 1. *In vivo* A20 haploinsufficiency causes stronger B cell hyperreactivity than its knockout

(A) Kaplan-Meier survival curves in GCB cell-specific A20-deficient mice with median survival times. Mice were immunized with sheep red blood cells (SRBCs) every 8 weeks until 12 months of age.

(legend continued on next page)

uniquely characterized by pronounced splenomegaly but did not yield further sex-biased alterations (Table S2). However, at the median age of the analyzed mice, around half of the female B-A20$^{wt/-}$ mice had died, possibly related to autoimmune pathologies. This prompted us to analyze younger mouse cohorts. At 2–3 months of age, B-A20$^{-/-}$ mice showed the strongest signs of inflammation in both sexes, including increased spleen size and plasmacytic cell numbers (Figure S1J; Table S2). However, female B-A20$^{wt/-}$ mice were distinguished by containing more spontaneous GCB cells (over 2-fold) compared with all other groups (Figures 1G and S1J). The GCB cell hyperplasia in female B-A20$^{wt/-}$ mice was more pronounced at ~10 months of age, which correlated with splenomegaly and elevated levels of anti-nuclear autoantibodies (ANAs), anti-double-stranded DNA (dsDNA), and anti-cardiolipin (CL) immunoglobulin G (IgG) autoantibodies (Figures 1H, S1K, and S1L). These results reveal that the female sex collaborates with A20 haploinsufficiency in B cells to drive autoreactive GCB cell differentiation, autoantibody formation, and progressive autoinflammation.

B cells lacking A20 (A20$^{-/-}$) are profoundly hyperreactive to stimulation *in vitro* but not in response to immunization with NP-haptenated proteins in alum *in vivo*.[25–27] To monitor acute responses of A20-deficient B cells to inflammatory stimuli, we performed immunizations with ovalbumin together with the innate trigger lipopolysaccharide (LPS). Immunization increased the numbers of B, GCB, and plasmacytic cells (plasmablasts and plasma cells) in male and female B-A20$^{wt/-}$ mice compared with controls (Figure 1I). By contrast, B-A20$^{-/-}$ mice did not produce elevated numbers of B or GCB cells but showed a trend toward more plasmacytic cells (Figure 1I). A higher tendency for plasmablast generation of A20$^{-/-}$ B cells was confirmed *in vitro* through the induction of plasmacytic differentiation in induced GCB cell cultures on fibroblast layers providing BAFF and CD40L (iGB[32]) (Figure S1M).

Collectively, the female sex collaborates with B cell-specific A20 haploinsufficiency in progressive age-associated lethal autoinflammation.

Augmenting the survival of A20 haploinsufficient B cells causes fatal SLE-like autoimmunity

Protection against FAS receptor (FAS)-induced apoptosis via increased BCLxL production was proposed as a mechanism explaining the effects of A20 deficiency.[27] Although we confirmed increased BCLxL levels in A20$^{-/-}$ B and GCB cells *in vivo* (Figure S2A), A20 deficiency did not protect iGB cells from apoptosis upon exposure to fibroblasts expressing FAS ligand (FASL)[33] (Figure 2A). Also, the addition of an *Eμ-BclxL* transgene (B-BclxL^{tg}) for BCLxL overexpression had no effect (Figure S2B). Nonetheless, B-BclxL^{tg}-A20$^{wt/-}$ mice developed splenomegaly early in life with increased B cell numbers and massive spontaneous GC formation (Figures 2B and S2C). A pronounced expansion of highly class-switched plasmacytic cells (Figures 2B and 2C) was accompanied by correspondingly high serum levels of plasma cell-derived soluble BCMA (sBCMA) along with elevated interleukin (IL)-10 and decreased transforming growth factor β (TGF-β) serum levels (Figures 2D and S2D), typical for the systemic autoimmune inflammation in human systemic lupus erythematosus (SLE).[34,35] Furthermore, IgG1, IgG2b, and IgG2c serum levels, as well as ANAs, anti-dsDNA, and anti-single-stranded DNA (ssDNA) autoantibodies were elevated (Figures 2E and S2E; Table S2). Accordingly, the lifespan of B-BclxL^{tg}-A20$^{wt/-}$ mice was dramatically reduced (Figure 2F). Histopathologic examination of the kidneys revealed immune complex deposition (Figure 2G), plasma cell and macrophage infiltration, as well as increased pathological glomerular alterations (Figures S2F and S2G) and defective renal filtration in some cases (Figure S2H). The mice developed antiphospholipid syndrome manifested by elevated serum levels of anti-CL and anti-serin-prothrombin autoantibodies (Figure 2H), as well as microthrombi in the kidneys (Figure 2I). Inducing arterial vessel damage *in vivo* led to enhanced thrombus formation in B-BclxL^{tg}-A20$^{wt/-}$ mice (Figure 2J). The only significant sex bias detected was slightly elevated ANA levels in female mice (Figure S2E).

By contrast, B-BclxL^{tg}-A20$^{-/-}$ mice did not develop pathologies up to 500 days of age and resembled the B-BclxL^{tg} controls in most aspects (Figures 2 and S2). The ratio of plasmacytic to GCB cells in B-BclxL^{tg}-A20$^{-/-}$ mice (1.8) was more than 2-fold higher than in B-BclxL^{tg} controls (0.7) (Figure 2B), confirming an enhanced differentiation of A20 knockout B cells into the plasma cell lineage. The reduced class-switching observed in BclxL^{tg}-A20$^{-/-}$ plasma cells (Figure 2C), together with massively increased IgM serum levels (Table S2), indicated increased extrafollicular differentiation. The inflammatory, autoimmune, and lifespan phenotypes caused by A20 deficiency in all B cells were recapitulated in mice with GCB cell-specific ablation of A20 (Figures S2I—S2K).

Ablation of activation-induced deaminase (AID) in AID$^{-/-}$ B-BclxL^{tg}-A20$^{wt/-}$ mice, preventing immunoglobulin class-switching and somatic hypermutation,[36] reduced the numbers of splenocytes, GCB cells, and plasmacytic cells by more than half compared with AID-sufficient controls (Figures S2L and S2M). In addition, these mice contained dramatically reduced serum levels of SLE-associated cytokines (Figure S2N), no immune

(B) Depiction of pathological alterations. LPD, lymphoproliferative disease; DLBCL-like, diffuse large B cell lymphoma.
(C) Staining of tissue sections of a representative DLBCL-like case as indicated.
(D) Kaplan-Meier survival curves in B cell-specific A20-deficient mice with median survival times.
(E) Depiction of pathological alterations of B cell populations and non-B cell-related pathologies in aged (>80 weeks) mice. MZBCH, marginal zone B cell hyperplasia; LPD, lymphoproliferative disease; TCH, T cell hyperplasia; RC, regressive changes; EMH, extramedullary hematopoiesis; AML, acute myeloid leukemia.
(F) Kaplan-Meier survival curves of B-A20$^{wt/-}$ mice separated according to sex with median survival times.
(G) Absolute numbers of GCB cells at 2–3 months of age.
(H) Absolute numbers of GCB cells and splenocytes, as well as serum levels of autoantibodies against double-stranded (ds) DNA at 10–13 months of age.
(I) Absolute numbers of naive B, GCB, and plasmacytic cells (PB/PC, plasmablast/plasma cell) in mice 10 days after immunization with ovalbumin (OVA)/LPS/alum.
$^{*}p < 0.05$, $^{**}p \leq 0.01$, $^{***}p \leq 0.001$, $^{****}p \leq 0.0001$. See also Figure S1. For additional information on mouse numbers, ages, and detailed statistics, see Table S1.

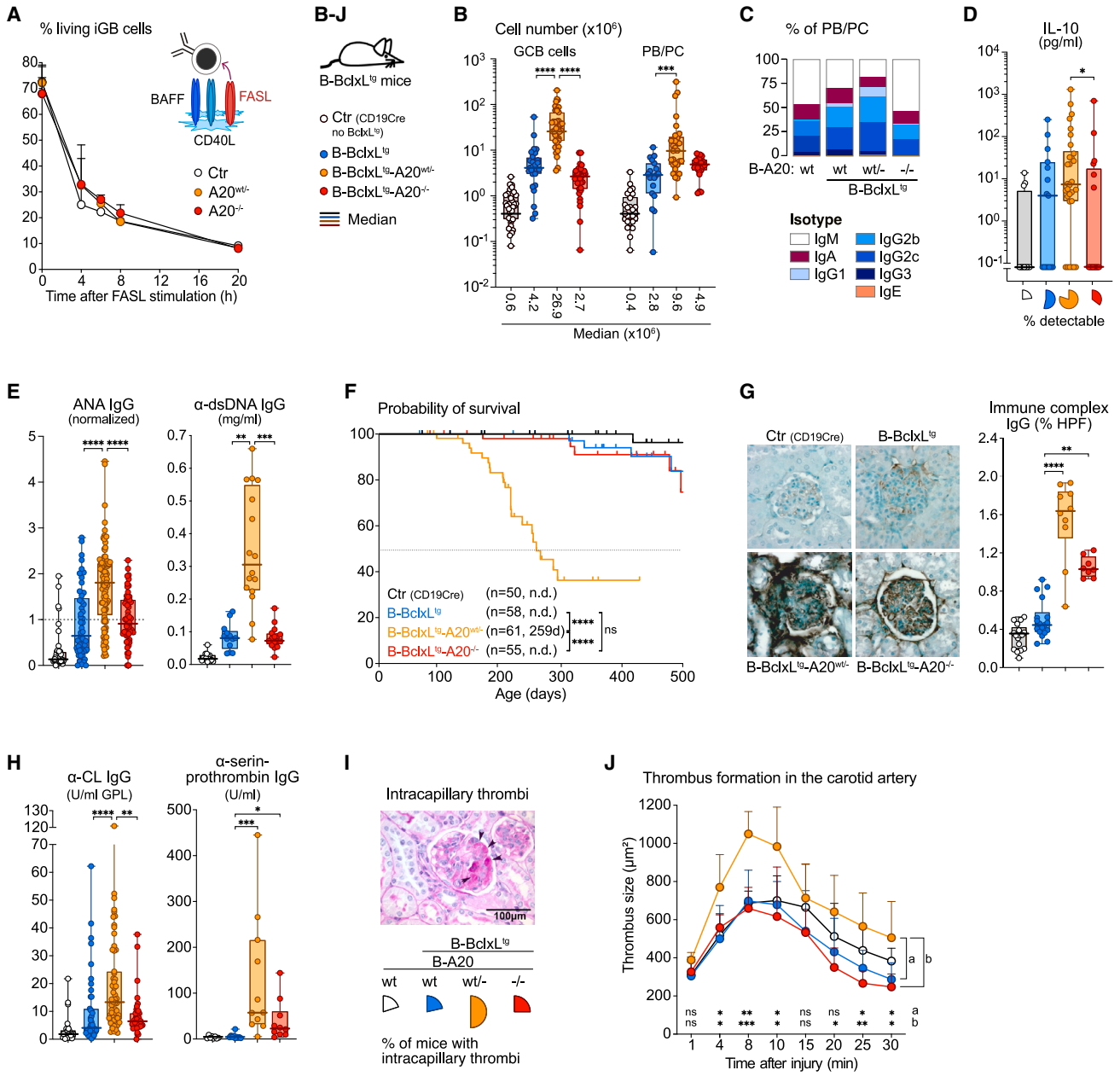

Figure 2. Augmenting the survival of mildly hyperactive B cells causes fatal SLE-like autoimmunity

(A) Fraction of living *in vitro* germinal center B (iGB) cells over time after co-culture with FASL-expressing 40LB feeder cells. Mean values and SD are shown.

(B) Absolute numbers of splenic GCB and plasmablasts/plasma cells (PBs/PCs).

(C) Isotype distribution of splenic plasmacytic cells.

(D) Serum concentration of IL-10 (pg/mL). Pie charts depict the percentage of samples with concentrations above the detection limit.

(E) Serum levels of anti-nuclear IgG autoantibodies (ANA, normalized to positive control) and anti-double-stranded DNA IgG antibodies (α-dsDNA, mg/mL).

(F) Kaplan-Meier survival curves of B cell-specific A20-deficient BclxL^{tg} mice with survival times.

(G) Representative pictures and quantified IgG immune complex deposition (% of high-power field [HPF]) in kidney glomeruli.

(H) Serum concentration of anti-cardiolipin IgG (α-CL, equal to U/mL; IgG phospholipid units [GPL]) and anti-serin-prothrombin IgG (U/mL) antibodies.

(I) Exemplary picture for intracapillary thrombi (highlighted by arrows) in PAS-stained kidney from a B-BclxL^{tg}-A20$^{wt/-}$ mouse. Pie charts depict the percentage of mice with intracapillary thrombi in the kidneys. Scale bar, 100 µm.

(J) Thrombus size over time after injury of the carotid artery. Significant differences per time point are depicted for B-BclxL^{tg}-A20$^{wt/-}$ versus B-BclxL^{tg}-A20$^{-/-}$ and B-BclxL^{tg} mice. Mean values and SD are shown.

ns: $p > 0.05$, *$p < 0.05$, **$p \leq 0.01$, ***$p \leq 0.001$, ****$p \leq 0.0001$. See also Figure S2 and Tables S1 and S2.

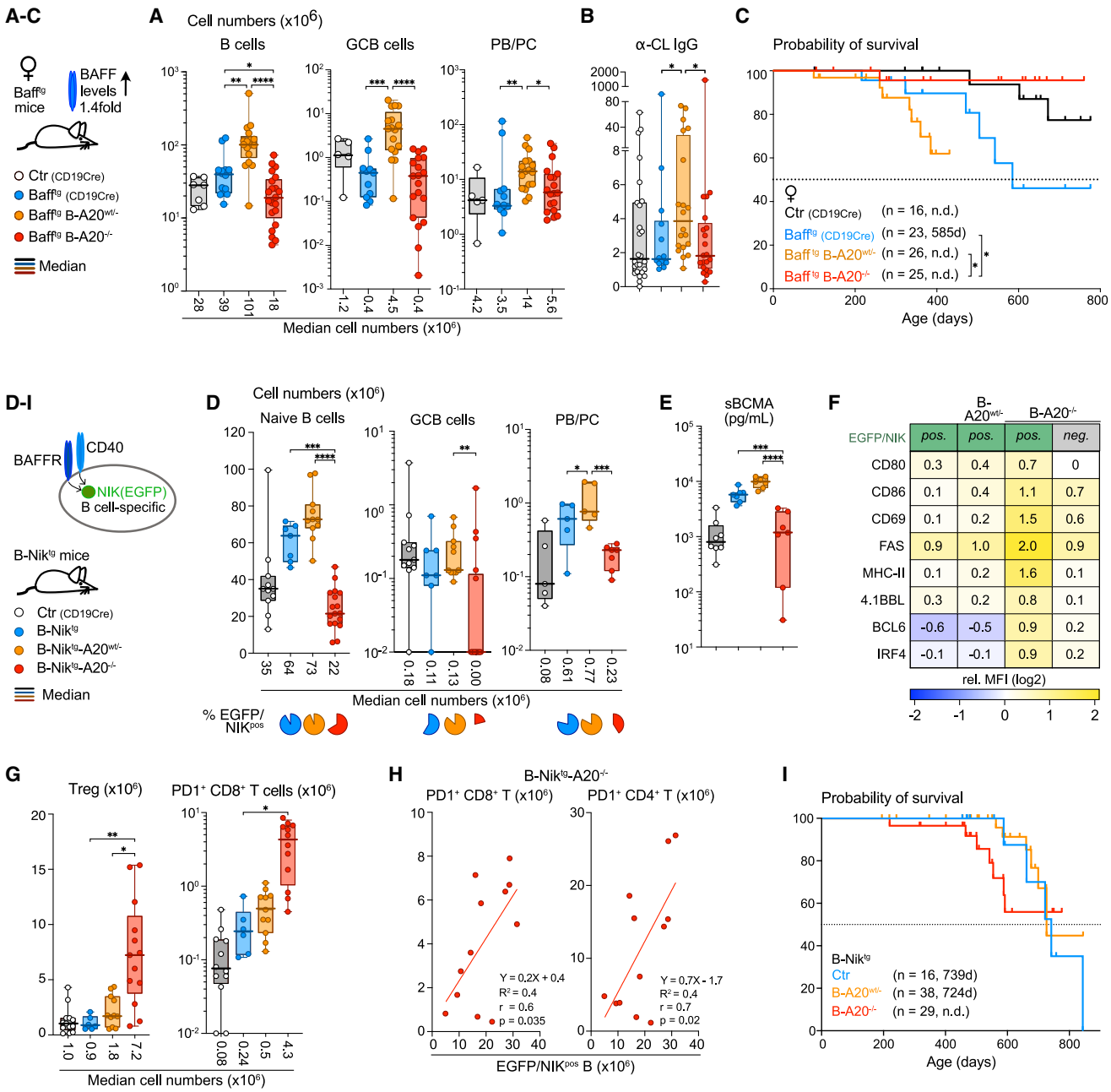

Figure 3. B cell-specific A20 haploinsufficiency exacerbates BAFF-driven autoimmunity, while extended hyperreactivity causes loss of B and plasma cells

(A) Absolute numbers of splenic naive B, GCB, and plasmablasts/plasma cells (PBs/PCs) in BAFF-transgenic A20-deficient female mice.

(B) Serum levels of anti-cardiolipin (α-CL, equal to U/mL GPL) IgG antibodies in BAFF-transgenic A20-deficient female mice.

(C) Kaplan-Meier survival curves of BAFF transgenic A20-deficient female mice with median survival times.

(D) Absolute numbers of splenic naive B, GCB, and plasmacytic cells (PB/PC) in B cell-specific NIK-transgenic A20-deficient mice. Pie charts depict the percentage of EGFP/NIK^{pos} cells.

(E) Serum concentration of soluble BCMA (sBCMA, ng/mL).

(F) Heatmap representing the $\log_2$fold change of protein expression in B cells from B-Nik^{tg}-A20 mice relative to CD19Cre control B cells measured by flow cytometry (see Table S3).

(G) Absolute numbers of splenic regulatory T cells (Treg, CD25$^+$ CD4$^+$ TCRβ$^+$—confirmed with Foxp3 staining) and splenic PD1$^+$ CD8$^+$ T cells.

(H) Simple linear regression and Pearson correlation between absolute EGFP/NIK^{pos} B cells and PD1$^+$ CD8$^+$ and CD4$^+$ T cells. Simple linear regression equation, R-squared (R^2), and Pearson's correlation coefficient (r) and the *p* value (*p*) are indicated.

(I) Kaplan-Meier survival curves of B cell-specific NIK-transgenic A20-deficient mice with median survival times.

*$p < 0.05$, **$p \leq 0.01$, ***$p \leq 0.001$, ****$p \leq 0.0001$. See also Figure S3 and Tables S1 and S3.

cell infiltration in the kidneys (Figure S2O), and an increased lifespan (Figure S2P).

Overall, the mild hyperreactivity of A20-haploinsufficient B cells combined with blocked apoptosis induces a lethal autoimmune pathology recapitulating human SLE, while stronger hyperreactivity does not.

Only B cell-specific A20 haploinsufficiency exacerbates BAFF-driven autoimmunity

To evaluate whether the nonlinear effects of A20 deficiency in B cells also occur in multifactorial autoimmunity, we introduced elevated levels of the B cell survival cytokine BAFF (*TNFSF13B*), which is a hallmark of human autoimmune diseases, particularly SLE and SjS.[37] We chose to focus on female BAFF-transgenic (Baff^{tg}) mice,[38] which contain ~1.4-fold more BAFF in their serum than female wild-type mice[39] (Figure S3A), closely recapitulating the effect of a *TNFSF13B* single-nucleotide polymorphism associated with human SLE.[40] Female Baff^{tg} B-A20$^{wt/-}$ mice displayed splenomegaly with hyperplasia of B, GCB, and plasmacytic cells (Figures 3A and S3B). They produced elevated levels of anti-CL autoantibodies and, to a lesser extent, ANAs, and developed kidney pathology (Figures 3B, S3C, and S3D). Furthermore, we observed lymphocytic infiltrations in the salivary gland, which is typical for SjS (Figure S3E). By contrast, Baff^{tg} B-A20$^{-/-}$ female mice contained fewer mature B cells and equal numbers of GCB and plasmacytic cells compared with Baff^{tg} controls. Moreover, they lacked autoantibody production, kidney pathology, and salivary gland infiltrations. Baff^{tg} B-A20$^{wt/-}$ mice had a reduced survival compared with Baff^{tg} controls; however, Baff^{tg} B-A20$^{-/-}$ mice survived significantly longer (Figure 3C).

Haploinsufficiency of A20 thus cooperates with mildly increased BAFF levels in the development of autoimmune/autoinflammatory pathologies, whereas A20 homozygous loss has protective effects and disadvantages B cells in this setting.

Extended hyperreactivity abolishes autoimmunity and causes loss of B and plasma cells correlating with PD1$^+$ T cell expansion

The loss of mature A20$^{-/-}$ B cells in Baff^{tg} mice suggested that increased BAFF signaling generates a disadvantage for these cells *in vivo*, which might relate to the reduced disease severity in the mice. To explore this possibility further, we introduced B cell-specific expression of a nuclear factor κB (NF-κB) inducing kinase (NIK) transgene (B-Nik^{tg}).[41] This model provides broader B cell hyperreactivity as NIK amplifies alternative NF-κB activation downstream of BAFF receptor (BAFF-R)[41] but also CD40.[42] Enhanced NIK expression causes B cell hyperplasia[41] and the development of lymphomas resembling DLBCL in conjunction with BCL6 overexpression.[42] Combining A20 deficiency with enhanced NIK expression in B cells thus results in concurrent amplification of canonical and alternative NF-κB activating signals, rendering them strongly hyperreactive to stimulation.

Compared with B-Nik^{tg} controls, B-Nik^{tg}-A20$^{wt/-}$ mice revealed trends toward increased B and plasmacytic cells, but not GCB cells (Figures 3D and S3F). B-Nik^{tg}-A20$^{-/-}$ mice contained very few B and plasmacytic cells in their immunological organs, and they were essentially devoid of spontaneous Nik^{pos}-A20$^{-/-}$ GCB cells (Figures 3D and S3F–S3H). In addition, many of the remaining B lineage cells did not express the conditional Nik transgene, monitored through the co-expressed EGFP (Figures 3D and S3F–S3H). This suggested that B cells with combined A20 ablation and NIK expression were selectively lost. sBCMA (Figure 3E) and serum immunoglobulin levels (Figure S3I) fully reflected the plasma cell paucity in B-Nik^{tg}-A20$^{-/-}$ mice. Likely due to the lack of B cells consuming BAFF in these mice, BAFF levels were elevated >10-fold (Figure S3J), which could reinforce the disadvantage of NIK^{pos}-A20$^{-/-}$ B cells. Flow cytometric analyses revealed pronounced cellular activation of the remaining NIK^{pos}-A20$^{-/-}$ B cells (Figure 3F; Table S3). Although B cell numbers were reduced in B-Nik^{tg}-A20$^{-/-}$ mice, T cell numbers were elevated compared with controls, mainly due to an expansion of regulatory T cells, as well as PD1$^+$ CD4$^+$ and CD8$^+$ T cells (Figures 3G and S3K). The linear correlation between the number of PD1$^+$ T cells and the size of the NIK^{pos}-A20$^{-/-}$ B cell pool (Figure 3H) suggested a causal functional relationship.

These phenotypes remained largely stable in aged B-Nik^{tg} cohorts, except for the expansion of splenic plasma cells and myeloid cells (Table S3). Histopathology revealed hyperplastic to neoplastic plasma cell expansions, as well as sporadic B cell neoplasms (Figures S3L and S3M; Table S3). ANA serum levels remained below those of CD19Cre controls in all aged B-Nik^{tg} cohorts, and elevated anti-CL autoantibody levels in B-Nik^{tg}-A20$^{wt/-}$ mice were the only autoimmune/autoinflammatory feature observed (Figure S3N; data not shown). Independent of A20 zygosity, all B-Nik^{tg} cohorts had a normal lifespan (Figure 3I).

We conclude that enhancing B cell hyperreactivity through amplification of NIK-mediated signals does not exacerbate A20 haploinsufficiency-driven autoimmune pathology but leads to dramatic B cell paucity in the complete absence of A20.

T cell ablation unleashes dramatic expansion and plasmacytic differentiation of hyperreactive B cells with high auto-reactive potential

The expansion of PD1$^+$ T cells in B-Nik^{tg}-A20$^{-/-}$ mice suggested an ongoing T cell response, potentially related to the loss of B lineage cells. We therefore introduced complete T cell deficiency through CD3ε ablation. The absence of T cells led to mature splenic B cell hyperplasia in all B-Nik^{tg} groups (Figure 4A), with a >30-fold increase in the number of highly class-switched plasmacytic cells in spleens and mesenteric lymph nodes (mLNs) of CD3ε$^{-/-}$ B-Nik^{tg}-A20$^{-/-}$ mice, mirrored by similarly elevated serum levels of sBCMA (Figures 4A and S4A–S4C). Correspondingly, the serum concentrations of all immunoglobulin isotypes were increased in CD3ε$^{-/-}$ B-Nik^{tg}-A20$^{-/-}$ mice (Figure 4B). In the absence of T cells, NIK^{pos} A20$^{-/-}$ B cells displayed an activated phenotype (Figures 4C, S4D, and S4E; Table S4). CD3ε$^{-/-}$ B-Nik^{tg}-A20$^{-/-}$ mice showed substantial autoinflammation, as evidenced by enhanced serum levels of IL-6, tumor necrosis factor (TNF), and IL-10 (Figure 4D), massive splenomegaly (Figures 4E and S4F), and elevated serum levels of ANA and anti-CL IgGs (Figure 4F).

These findings begged the question of whether T cells also restrain BclxL^{tg}-A20-deficient B and plasma cells. Antibody-mediated T cell depletion led to a decrease in plasmacytic cells in B-BclxL^{tg}-A20$^{wt/-}$ mice but an increase in B-BclxL^{tg}-A20$^{-/-}$ mice (Figure S4G). Analogously, genetic T cell deficiency in CD3ε$^{-/-}$ B-BclxL^{tg}-A20$^{wt/-}$ mice abrogated GCB cells, as expected, and reduced plasmacytic cell numbers (Figure 4G;

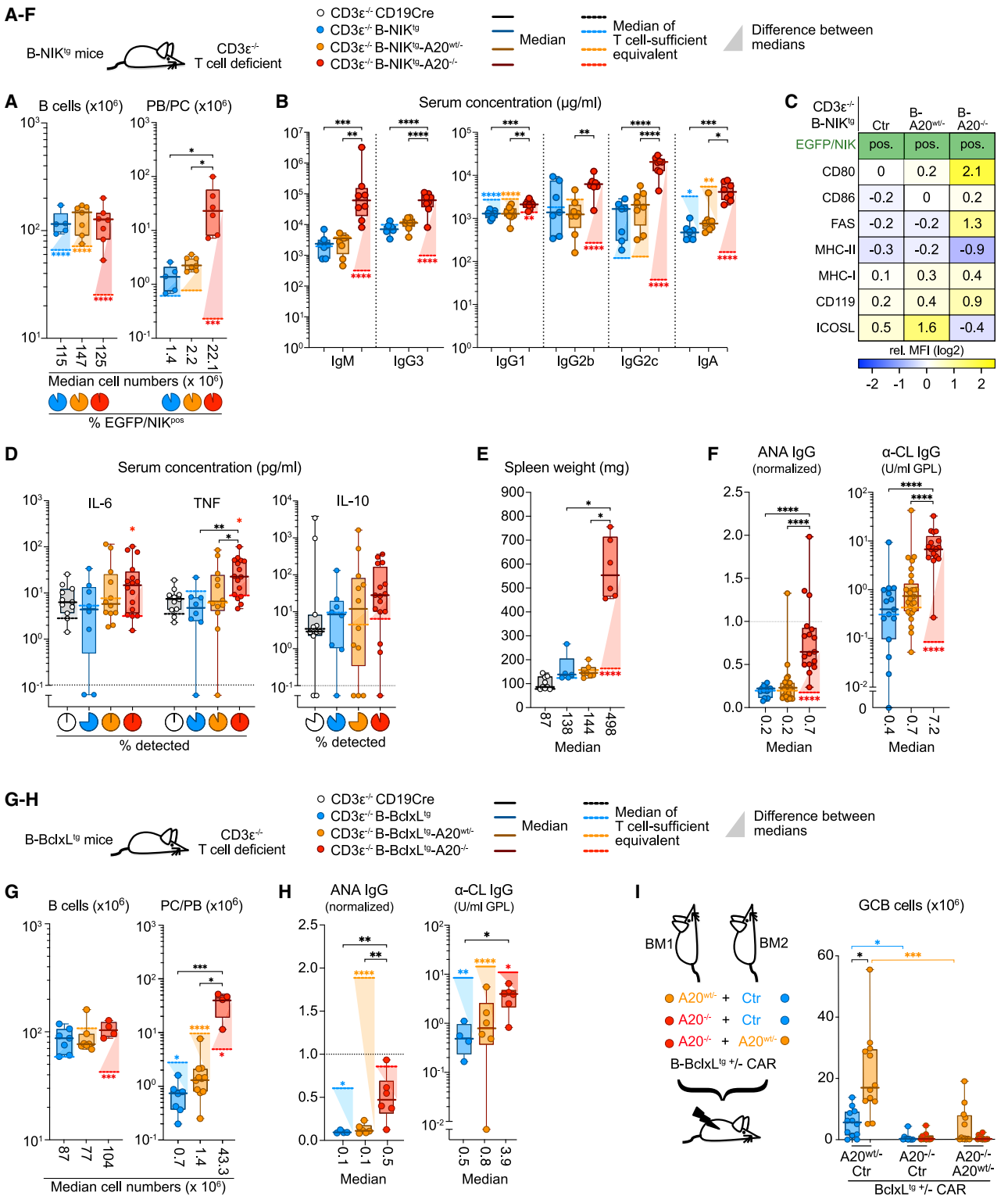

Figure 4. Absence of T cells unleashes dramatic expansion and plasmacytic differentiation of hyperreactive B cells

(A) Absolute numbers of splenic total B cells and plasmablasts/plasma cells (PBs/PCs) in young CD3ε$^{-/-}$ B-Nik^{tg} mice. Pie charts depict the percentage of EGFP/NIK^{pos} cells.

(B) Serum concentration of immunoglobulins in CD3ε$^{-/-}$ B-Nik^{tg} mice.

(C) Heatmap representing the $\log_2$fold change of protein expression in B cells from CD3ε$^{-/-}$ B-Nik^{tg} mice relative to CD19Cre control B cells measured with flow cytometry (see Table S4).

(legend continued on next page)

data not shown). By contrast, compared with their T cell-sufficient counterparts, CD3ε$^{-/-}$ B-BclxL^{tg}-A20$^{-/-}$ mice generated a 10-fold increase of mature naive B and plasmacytic cells, which displayed a class-switching bias toward IgG2c and IgG2b (Figures 4G, S4H, and S4I). Although autoantibody production was reduced in all T cell-deficient B-BclxL^{tg} groups (Figure 4H), in line with the relevance of T cell-dependent GC reactions for their pathology, within the CD3ε$^{-/-}$ B-BclxL^{tg} groups, B-A20$^{-/-}$ mice contained the highest levels of autoantibodies. T cell deficiency in B-A20$^{-/-}$ and B-A20$^{wt/-}$ mice revealed similar trends (Figures S4J–S4L; Table S4).

Our results implied that either T cells restrain the autoreactivity of BclxL^{tg}-A20$^{-/-}$ B cells more than that of BclxL^{tg}-A20$^{wt/-}$ B cells and/or that A20-haploinsufficient BclxL^{tg} B cells are better at generating and/or receiving T cell help. To clarify this matter, we generated mixed bone marrow chimeras resulting in mice containing pairwise combinations of BclxL^{tg}, BclxL^{tg}-A20$^{wt/-}$, and BclxL^{tg}-A20$^{-/-}$ B cells (Figure 4I). BclxL^{tg}-A20$^{wt/-}$ B cells caused enhanced spontaneous GC reactions and displayed a cell-intrinsic competitive advantage in all B cell subsets when paired with BclxL^{tg} B cells. On the other hand, the presence of BclxL^{tg}-A20$^{-/-}$ B cells led to very low numbers of GCB, plasmacytic, and B cells of both co-transplanted genotypes and markedly enhanced the ratios of PD1^{+} CD4^{+} and CD8^{+} T cells to B cells (Figures 4I, S4M, and S4N). These results suggest that BclxL^{tg}-A20$^{-/-}$ B cells induce a self-restraining immune response that also efficiently curtails highly autoreactive (BclxL^{tg}-A20$^{wt/-}$) as well as mildly autoreactive (BclxL^{tg}) B cells.

In summary, depending on the extent of the intrinsic B cell hyperreactivity, T cells can play opposing roles. *In vitro*, A20$^{-/-}$ B cells react much stronger to stimulation than A20$^{wt/-}$ B cells.[25,27] The apparently opposite result *in vivo* is due to the presence of T cells. In B-Nik^{tg}-A20$^{-/-}$ mice, where B cells amplify alternative and canonical NF-κB activating signals, T cells efficiently and continuously suppress dramatic autoinflammation, accumulation of plasma cells, and autoantibody production. In B-BclxL^{tg}-A20$^{wt/-}$ mice, where B cells possess mild intrinsic hyperreactivity, T cells drive lethal GC-mediated autoimmunity, which is abolished in their absence. Overall, the graded effects in the different groups of compound mutant mice suggest that increased intrinsic B cell reactivity gradually shifts the overall T cell response from B cell help to B cell destruction.

Lack of T cells reveals the transforming potential of immune-signal-amplifying genetic alterations

Our studies indicated that *in vivo* hyperactive B cells induce self-restraining T cell responses. Indeed, the survival of the T cell-deficient mouse cohorts dramatically decreased, in correlation with the intrinsic hyperreactivity of their B cells: B-Nik^{tg}-A20$^{-/-}$ > B-Nik^{tg}-A20$^{wt/-}$, B-Nik^{tg}, B-BclxL^{tg}-A20$^{-/-}$ > B-BclxL^{tg}-A20$^{wt/-}$, B-A20$^{-/-}$ > B-A20$^{wt/-}$, B-BclxL^{tg} > Ctrl (Figure 5A). Premature death corresponded with the time of onset of massive lymphoproliferation in the spleen and lymph nodes (LNs), with dissemination to the liver, pancreas, and rarely the lungs (Figure S5A; Table S5). Except for NIK^{pos}-A20$^{-/-}$ lymphoproliferations, which showed no evidence of clonality, the B cell expansions were mostly clonal, as assessed by PCR assays and BCR sequencing, which also revealed absent or low-level somatic hypermutation (Figures 5B and S5B; Table S5). Histologically, the expansions resembled lymphomas of large B cells (Figures 5C and S5C). Neoplastic B cells from all CD3ε$^{-/-}$ B-Nik^{tg} cohorts were uniformly IgM positive, expressed high levels of FAS, CD80, OX40L, and IRF4, elevated BLIMP1, low or no CD138, and Ki67 staining indicated their aggressive expansion (Figures 5D, S5D, and S5E). Common features defining NIK^{pos}-A20$^{wt/-}$ and NIK^{pos} neoplasms, including their resemblance of GCB cells (BCL6^{hi}, CD38^{lo}), were unique to the malignantly expanded populations in sick mice (Figures 5E and S5D–S5F). By contrast, NIK^{pos}-A20$^{-/-}$ neoplasms closely resembled premalignant B cells in healthy mice of the same genotype (Figures 5E and S5F), and histological analyses suggested multifocal cellular expansion over time (Figure S5G). This demonstrates that normal physiological endogenous triggers are sufficient to cause lymphoproliferation of B cells with very high sensitivity to stimulation (NIK^{pos}-A20$^{-/-}$) in the absence of additional clonal events.

Our results highlight the role of A20 as a haploinsufficient tumor suppressor, confirm NIK as a proto-oncogene in B cells, and reveal that T cells can completely suppress pathology over a wide range of genetic B cell hyperreactivity.

CD40 signals activate NIK^{pos}-A20$^{-/-}$ B cells in the presence and absence of T cells

Next, we set out to characterize the transcriptional reprogramming and the *in vivo* triggers causing spontaneous lymphoproliferation of NIK^{pos}-A20-deficient B cells in the absence of T cells. Bulk RNA sequencing (RNA-seq) revealed that graded loss of A20 in NIK^{pos} B cells correlated with enhanced expression of

(D) Serum concentration of IL-6, TNF, and IL-10 in CD3ε$^{-/-}$ B-Nik^{tg} mice. Pie charts depict the percentage of samples with concentrations above the detection limit.

(E) Spleen weight of young CD3ε$^{-/-}$ B-Nik^{tg} mice.

(F) Serum levels of anti-nuclear IgG antibodies (ANA, normalized to positive control) and anti-cardiolipin IgG (α-CL, equal to U/mL GPL) antibodies in CD3ε$^{-/-}$ B-Nik^{tg} mice.

(G) Absolute numbers of splenic total B and plasmacytic cells (PB/PC) in young CD3ε$^{-/-}$ B-BclxL^{tg} mice.

(H) Serum levels of anti-nuclear IgG antibodies (ANA, normalized to positive control) and anti-cardiolipin (α-CL, equal to U/mL GPL) IgG antibodies in CD3ε$^{-/-}$ B-BclxL^{tg} mice.

(I) Schematic depiction: competitive bone marrow chimeras were generated by mixing B and T cell-depleted bone marrow cells from mice of the indicated genotypes in a 1:1 ratio in pairwise combinations, followed by adoptive transfer into sublethally irradiated Rag2$^{-/-}$ mice. B cells of the two different genotypes in one chimera were differentiated by the expression or absence of the truncated human coxsackie adenovirus receptor (CAR).[43] Boxplots represent the absolute numbers of GCB cells of the indicated genotypes in the chimeras, 6 weeks after transplantation.

(A–H) Median values are indicated below some graphs. Continuous lines depict medians, dotted lines depict medians of the corresponding T cell-sufficient counterpart (see Figures 2 and 3), and shaded triangles highlight the difference between medians.

*$p < 0.05$, **$p \leq 0.01$, ***$p \leq 0.001$, ****$p \leq 0.0001$. See also Figure S4 and Tables S1 and S4.

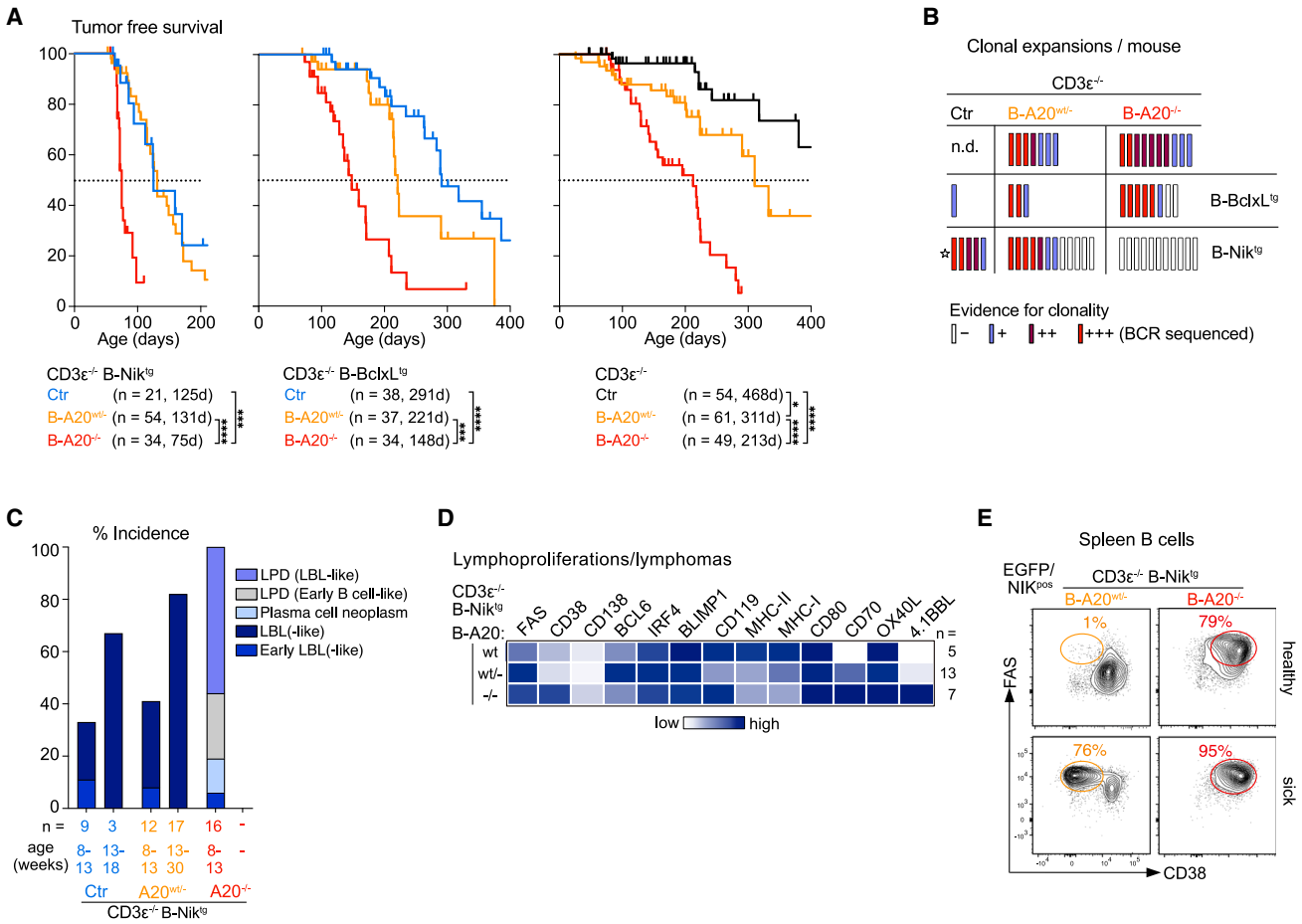

Figure 5. Lack of T cells reveals the transforming potential of immune-signal-amplifying alterations

(A) Kaplan-Meier survival curves for CD3ε$^{-/-}$ B-Nik^{tg}, CD3ε$^{-/-}$ B-BclxL^{tg}, and CD3ε$^{-/-}$ mice with B cell-specific A20 deficiency. Median survival times are shown.

(B) Tumor clonality classified based on the amplification of the BCR heavy-chain (JH1–4) and kappa-light-chain rearrangements (Vκdeg-Jκ5BR, Jκdeg-Jκ5AR). – no evidence for clonality, + evidence for clonality, ++ clonal, +++ clonality confirmed by BCR sequencing in 18 out of 19 tested lymphomas, * histiocytic sarcoma. See Figure S5B and Table S5.

(C) Incidence of lymphoma-like pathology in CD3ε$^{-/-}$ B-Nik^{tg} mice divided by A20 genotype and age: 8–13 weeks and older than 13 weeks; LBL, large B cell lymphoma; LPD, lymphoproliferative disease.

(D) Expression intensity of markers on B cell lymphoma (CD38^{low} FAS^{high}, IgD^{low} IgM^{pos}, [EGFP^{pos}] B220^{low}, or CD62L^{low}) and lymphoproliferations (B-Nik^{tg}-A20$^{-/-}$: EGFP^{pos} FAS^{high} or CD62L^{low}) in the spleen or mesenteric lymph nodes (mLNs) determined by flow cytometry. The heatmap summarizes the mean signal intensity per genotype. Classification of signal intensity: 1, negative/low; 2, intermediate; 3, high. For further information and calculation of expression scores, see Table S5.

(E) Representative fluorescence-activated cell sorting (FACS) plots depicting FAS and CD38 surface expression in splenic EGFP/NIK-expressing B cells from healthy and sick CD3ε$^{-/-}$ B-Nik^{tg} mice with heterozygous or homozygous A20 deletion in B cells.

*$p < 0.05$, ***$p \leq 0.001$, ****$p \leq 0.0001$. See also Figure S5 and Tables S1 and S5.

gene signatures representing plasma cell identity, B cell activation, and SLE. This increase was not linear, as NIK^{pos}-A20$^{-/-}$ B cells contained by far the most dramatic changes (Figures 6A, 6B, S6A, and S6B). Single-cell RNA-seq (scRNA-seq) analysis of A20-deficient NIK^{pos} and control NIK^{pos} B cells identified a cluster of NIK^{pos}-A20$^{-/-}$ B cells resembling activated B cells present in both the presence and absence of T cells (B-act, Figures 6C and S6C–S6E). By integrating *in vitro* and *in vivo* transcriptomic data, we established A20-repressed gene sets unique to LPS activation, unique to CD40 activation, or common to LPS, αCD40, and αIgM stimulation (Figure S6F; Table S6). Projection onto the scRNA-seq data revealed that elevated expression of these gene sets is a universal feature of nearly all NIK^{pos}-A20$^{-/-}$ B cells in mice lacking T cells (Figure 6D). The strongest activation at the single-cell level was seen for the *CD40-activated* gene set in the B-act cluster (Figure 6D), and the wide range of expression intensities suggested a dynamic regulation *in vivo*. Expression of the *CD40-activated* signature was similar in the presence and absence of T cells, indicating that NIK^{pos}-A20$^{-/-}$ B cells receive comparable CD40(-like) signals. B cells expressing Epstein-Barr virus (EBV)-derived LMP1, mimicking constitutive CD40 signaling, trigger a potent Eomesodermin (EOMES)-driven cytotoxic T cell response via a defined group of cell surface receptors.[44]

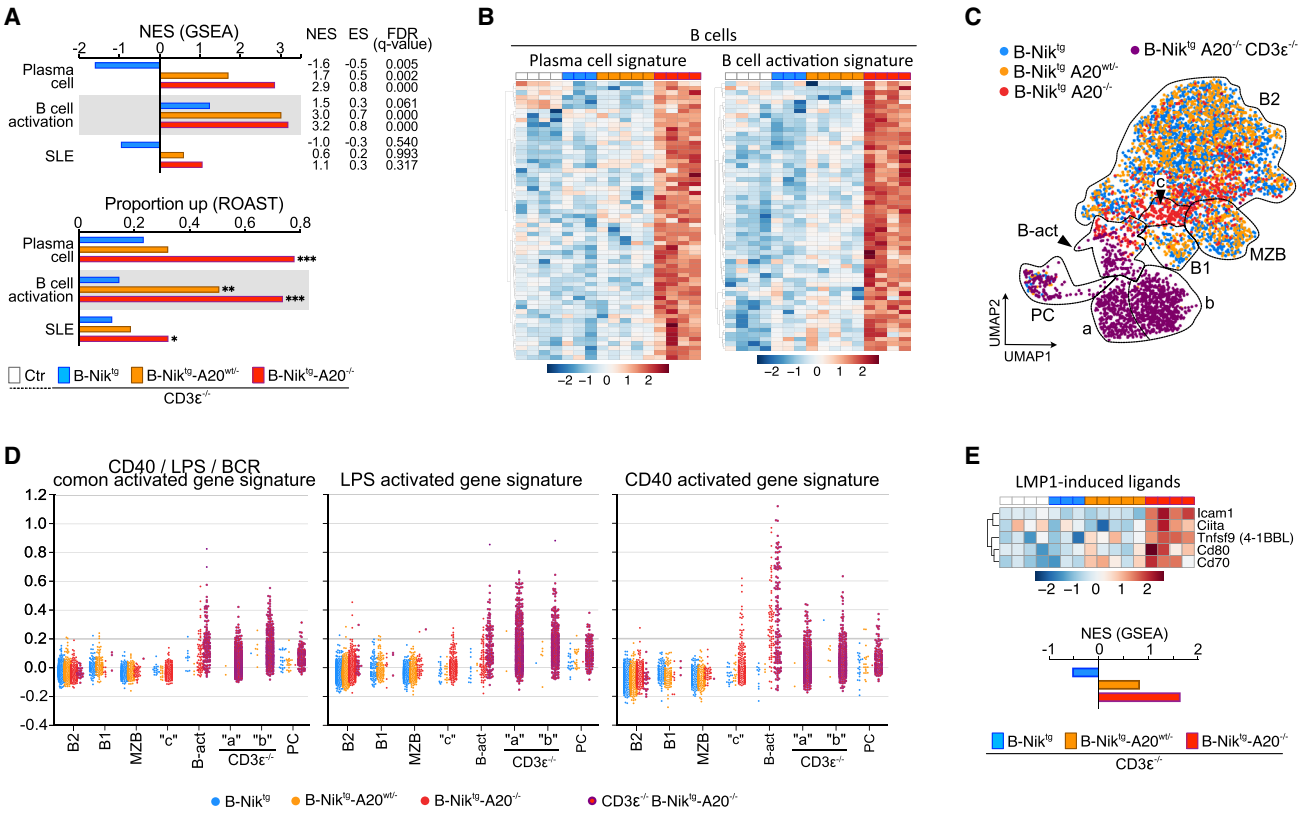

Figure 6. CD40 triggers activation of NIK^{pos}-A20$^{-/-}$ B cells in the presence and absence of T cells

(A) Normalized enrichment scores (NESs, calculated with gene set enrichment analysis [GSEA]) and proportions of upregulated gene sets (calculated with rotation gene set tests [ROASTs], false discovery rate [FDR] corrected *p* values for each pairwise comparison) describing plasma cell identity, B cell activation, and a gene set upregulated in B cells from human SLE patients[69] (Table S6). RNA sequencing data of NIK^{pos}, NIK^{pos}-A20$^{wt/-}$, and NIK^{pos}-A20$^{-/-}$ mature follicular B cells purified from CD3ε$^{-/-}$ mice compared with control B cells (2 CD3ε$^{-/-}$ and 2 CD19Cre^{ERT2} mice) were analyzed.

(B) Expression of plasma cell identity genes and B cell activation genes in NIK^{pos}, NIK^{pos}-A20$^{wt/-}$, and NIK^{pos}-A20$^{-/-}$ mature follicular B cells purified from CD3ε$^{-/-}$ mice. The heatmaps depict only genes that are significantly different between the groups ($p$adj < 0.01, $\log_2$fold change > 0.8).

(C) Uniform manifold approximation and projection (UMAP) plot of scRNA-seq dataset of CD79a^{+} B cells from the indicated mice. Colors represent genotypes. Populations were identified based on the expression of marker genes (Figures S6C and S6D). MZB, marginal zone B cells; PC, plasmablasts/plasma cells; a and b, CD3ε$^{-/-}$ B-Nik^{tg}-A20$^{-/-}$ dominated clusters; c, B-Nik^{tg}-A20$^{-/-}$ dominated cluster.

(D) Enrichment score per cell for A20-suppressed gene sets activated commonly by αCD40, αIgM, or LPS, only by LPS, or only by CD40, depicted by clusters (label) and genotypes (color).

(E) Heatmap showing expression of and NES scores of LMP1-induced costimulatory ligands in mature follicular B cells purified from mice of the indicated genotypes. NES scores in comparison to control B cells (2 CD3ε$^{-/-}$ and 2 CD19Cre^{ERT2} mice) were derived through GSEA.

*p < 0.05, **$p \leq 0.01$, ***$p \leq 0.001$. See also Figure S6 and Table S1. Gene sets are listed in Table S6.

Congruent with enhanced CD40(-like) signals, several of these receptors were also expressed on NIK^{pos}-A20$^{-/-}$ B cells from T cell-deficient mice (Figures 5D and 6E).

Our data revealed strongly enhanced transcriptional activation of NIK^{pos}-A20$^{-/-}$ B cells in the absence of T cells, in agreement with the notion that T cells suppress/eliminate activated B cells. Furthermore, they pinpointed CD40 as a key hub inducing strong activation of a subset of these cells.

Hyperreactive B cells induce negative feedback control via cytotoxic T cells and FASL

In line with enhanced co-stimulatory molecule expression implicated in induced cytotoxic T cell differentiation on NIK^{pos}-A20$^{-/-}$ B cells, the T cell response triggered in B-Nik^{tg}-A20$^{-/-}$ and, to a lesser extent, in B-Nik^{tg}-A20$^{wt/-}$ mice is characterized by a marked expansion of EOMES^{hi} CD4^{+} and CD8^{+} T cells (Figure 7A). Investigating T cells of the B-Nik^{tg} mouse groups by scRNA-seq (Figures 7B, S7A, and S7B) showed two cytotoxic clusters containing CD4^{+} and CD8^{+} T cells expressing *Eomes* together with *Perforin1* (*Perf1*), granzymes, and *Fasl* (Figure 7C). One cluster (Ttoxic) expressed a cytotoxic gene signature correlating with increased B cell reactivity (decreased A20 gene dosage) (Figures 7D and S7C; Table S6). While there was no strong evidence for functional exhaustion and dysfunction (Figure S7D; Table S6), the other *Eomes*-expressing cluster was characterized by high expression of genes typical for precursors of exhausted cells (Tpex), including *Myb* (Figures 7E and S7E; Table S6), which controls the function of stem-like (sl)-Tpex cells in the context of chronic viral infections.[45] The induction of such cells, of which some also showed characteristic

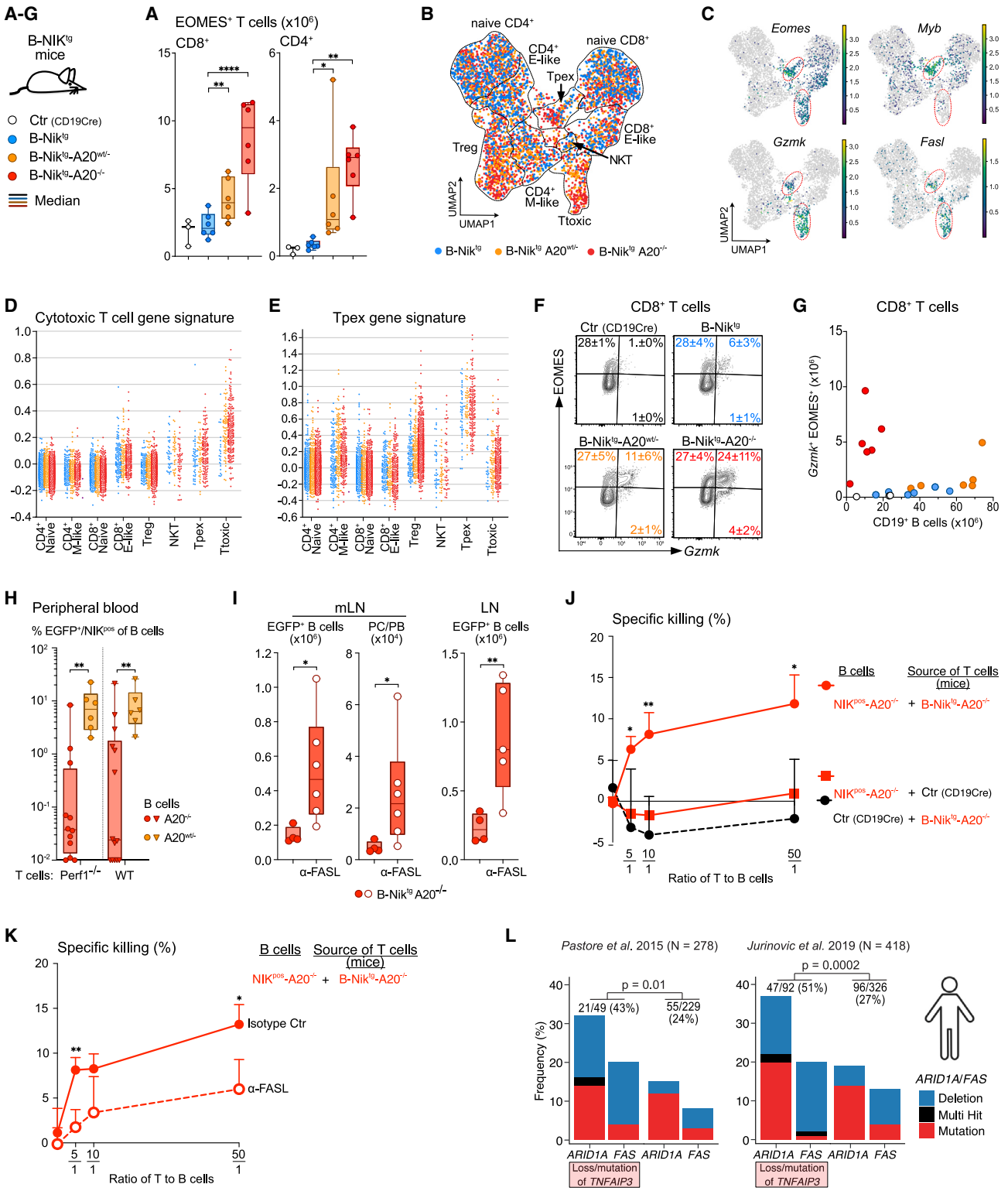

Figure 7. Hyperreactive B cells induce negative feedback control via cytotoxic T cells and FASL

(A) Absolute number of EOMES$^+$ CD8$^+$ and CD4$^+$ T cells in B-Nik^{tg} mice.

(B) UMAP plot of scRNA-seq dataset of CD3$^+$ T cells from B-Nik^{tg}, B-Nik^{tg}-A20$^{wt/-}$, and B-Nik^{tg}-A20$^{-/-}$ mice. Colors represent genotypes. Populations were identified based on the expression of marker genes. Treg, regulatory T cells; M-like, memory-like; E-like, effector-like; NKT, natural killer T cells; Tpex, precursor of exhausted T cells; T-toxic, cytotoxic T cells. Undefined cells lie within clusters with unclear cell type affiliation.

(legend continued on next page)

evidence for recent T cell receptor (TCR) signals (Figure S7F; Table S6), probably reflects the chronic battle of T cells against the aberrant B cells. We validated elevated expression of *Gzmk*, *Gzmb*, and *Perf1* mRNAs in *ex vivo*-isolated T cells. This also revealed that the ratio of cytotoxic CD4$^+$ and CD8$^+$ T cells to B cells was much higher in B-Nik^{tg}-A20$^{-/-}$ mice compared with B-Nik^{tg}-A20$^{wt/-}$ and B-Nik^{tg} mice (Figures 7F, 7G, S7G, and S7H Data S1).

To confirm that NIK^{pos}-A20$^{-/-}$ B cells directly trigger cytotoxic T cell differentiation, we set up co-cultures of anti-CD40-activated B cells with T cells isolated from wild-type mice. *Ex vivo*-isolated NIK^{pos}-A20$^{-/-}$ B cells had higher co-stimulatory molecule expression implicated in triggering cytotoxic T cell differentiation (CD70, 4-1BBL, OX40L[44,46]) compared with controls, and CD40 signals further amplified the differences (Figure S7I). Accordingly, NIK^{pos}-A20$^{-/-}$ B cells triggered robust differentiation of EOMES$^+$ CD8$^+$ and CD4$^+$ T cells, while control B cells did not (Figure S7J).

To functionally interrogate the contribution of the granzyme/perforin system in eliminating NIK^{pos}-A20$^{-/-}$ B cells, we generated mixed bone marrow chimeras in which the B cells were either NIK^{pos}-A20$^{-/-}$ or NIK^{pos}-A20$^{wt/-}$, and the T cells were either wild type or Perf1$^{-/-}$, incapable of perforin-dependent cytotoxic killing (scheme in Figure S7K). The reconstitution of NIK^{pos}-A20-deficient B cells was low in the resulting chimeras, and the proportion of NIK^{pos}-A20$^{-/-}$ B cells was >10 times lower than that of NIK^{pos}-A20$^{wt/-}$ B cells in peripheral blood and spleen. Furthermore, there was no difference between chimeras containing wild-type or Perf1$^{-/-}$ T cells (Figures 7H and S7K), indicating that the perforin/granzyme system in T cells is not uniquely required to kill B cells in B-Nik^{tg}-A20$^{-/-}$ mice. The high expression of the CD40 target FAS on B cells, together with the elevated *Fasl* expression in T cells of B-Nik^{tg}-A20$^{-/-}$ mice, suggested an important role for FAS-mediated killing. Repeated injections of FASL-blocking antibodies for 1 week resulted in elevated numbers of NIK^{pos}-A20$^{-/-}$ B and plasmacytic cells in mLNs and LNs, with a similar trend in the spleen (Figures 7I and S7L). To directly demonstrate T cell-mediated killing of NIK^{pos}-A20$^{-/-}$ B cells, we co-cultured *ex vivo*-isolated anti-CD40/BAFF/IL-4-stimulated B cells with T cells isolated from B-Nik^{tg}-A20$^{-/-}$ or control mice. Only T cells from B-Nik^{tg}-A20$^{-/-}$ mice induced apoptosis in NIK^{pos}-A20$^{-/-}$ B cells, monitored by activated caspase-3 staining, but not in controls (Figures 7J and Data S1). The addition of FASL-blocking antibodies revealed a significant contribution of FASL:FAS interactions to T cell-mediated cytotoxicity (Figure 7K). Furthermore, T cells isolated from control mice and *in vitro* differentiated to become cytotoxic through co-culture with NIK^{pos}-A20$^{-/-}$ iGB cells preferentially killed NIK^{pos}-A20$^{-/-}$ iGB compared with control iGB cells (Figures S7M and S7N).

Our data thus indicate that FAS-induced killing represents an important mechanism in the immune surveillance of hyperactive B cells.

Genetic lesions inactivating *TNFAIP3*/A20 and FAS frequently co-occur in follicular lymphoma

To explore whether loss of A20 could also be linked to FAS-mediated immune surveillance in humans, we investigated the relationship between genetic alterations inactivating A20 and loss of FAS in follicular lymphoma (FL) in two large independent cohorts (GALLIUM,[47] n = 418 cases, and the GLSG/BCCA cohorts,[48] n = 278 cases). These tumors carry deletions and inactivating mutations of *TNFAIP3*/A20,[49,50] but also heavily depend on T cell support.[51] Thus, we hypothesized that they might more frequently harbor somatic alterations that selectively cause resistance to T cell killing rather than completely disengage from T cells. We found that A20 deficiency, detected in 22% and 17% of the cases in our cohorts, was significantly associated with loss of *FAS*, either directly through inactivating mutations/copy-number loss or indirectly through mutations/deletions affecting *ARID1A*, which controls FAS expression[52] (Figures 7L and S7O). These data support a scenario in which, in FL, loss of A20 triggers or enhances FAS-mediated immune surveillance, followed by immune escape.

Collectively, we demonstrated that strongly hyperactive B cells trigger a potent T cell immune checkpoint, whose cytotoxic response is calibrated to the aberrant activation status of the B cells.

DISCUSSION

During evolution, opposing selection pressures balance the need for efficient protective immune cell activation with the

(C) Normalized gene expression of *Eomes*, *Myb, Gzmk*, and *FasL* projected onto the scRNA-seq T cells UMAP.
(D and E) Enrichment score per cell for (D) cytotoxic T cell and (E) Tpex signature gene sets separated by clusters (label) and genotypes (color).
(F) Representative FACS plots depicting EOMES (protein) and *Gzmk* or *Gzmb* (mRNA) signal in CD8$^+$ T cells from control, B-Nik^{tg}, B-Nik^{tg}-A20$^{wt/-}$, and B-Nik^{tg}-A20$^{-/-}$ mice. Numbers show the mean percentages and SD of n = 6 mice per genotype.
(G) Dotplots showing the absolute number of *Gzmk*/EOMES double-positive CD8$^+$ T cells in correlation with the absolute number of CD19$^+$ B cells per mouse.
(H) Percentage of EGFP/NIK-expressing A20-deficient B cells harboring a conditional NIK transgene in the peripheral blood of mixed bone marrow chimeras containing *Perf1*$^{-/-}$ or wild-type T cells, measured 10 weeks after transplantation. Chimeras were generated by mixing bone marrow cells from CD3ε$^{-/-}$ B-Nik^{tg}-A20$^{wt/-}$ or CD3ε$^{-/-}$ B-Nik^{tg}-A20$^{-/-}$ mice with *Perf1*$^{-/-}$ or wild-type bone marrow.
(I) Absolute number of EGFP/NIK-expressing B cells and plasmablasts/plasma cells (PBs/PCs) in mLN and LN from B-Nik^{tg}-A20$^{-/-}$ mice treated with FASL-depleting antibody for 7 days (white dots) and PBS-treated control mice (red dots).
(J) Specific killing [% of active caspase-3$^+$ B cells in T-B cell co-cultures] − [% of active caspase-3$^+$ B cells in only-B cell cultures] of *in vitro*-stimulated primary Nik^{tg}-A20$^{-/-}$ and Ctr (wild type or CD19Cre) B cells by T cells. T cells were isolated *ex vivo* from B-Nik^{tg}-A20$^{-/-}$ (4 biological replicates) or Ctr (2 biological replicates) mice and co-cultured with B cells for 18 h. Data represent mean values and SD of biological replicates, which were measured as average of technical triplicates. Statistical differences were assessed between NIK^{pos}-A20$^{-/-}$ and Ctr B cells co-cultured with T cells isolated from B-Nik^{tg}-A20$^{-/-}$ mice.
(K) The indicated T:B co-cultures (4 biological replicates performed and depicted as described in J) were treated with anti-FASL or isotype control antibody. Mean values and SD are shown.
(L) Frequency and type of *FAS* and *ARID1A* alterations in different *TNFAIP3* genetic backgrounds in two independent FL cohorts. Number and percentages of cases with *FAS* and/or *ARID1A* alterations of *TNFAIP3*-deficient and intact cases are indicated.
*p < 0.05, **$p \leq 0.01$, ****$p \leq 0.0001$. See also Figure S7 and Table S1. Gene sets are listed in Table S6.

prevention of self-reactivity and uncontrolled immune cell expansion. The large number of B cells carrying autoreactive specificities in healthy individuals[53] are in constant danger of developing into expanding autoreactive B cell clones, especially when they carry preexisting germline variants and undergo somatic mutations and epigenetic reprogramming. All these mechanisms reduce the expression and/or function of A20 in human B cells in autoimmunity, particularly in SLE, SjS, and rheumatoid arthritis.[3,10,18,54–56] Here, we demonstrate that female sex and reduced A20 levels specifically in B cells caused progressive lethal autoinflammation. It seems likely that escape of X inactivation by TLR7,[57] as well as incomplete X inactivation of other immune genes as observed in human SLE patients,[58,59] contributes to the sex bias we observed. BAFF levels are elevated in around 30% of SLE patients,[37] and our data indicate that a minor increase in soluble BAFF levels is sufficient to cause strongly enhanced autoreactive responses of A20 haploinsufficient B cells in female mice.

Once aberrant B cell hyperreactivity surpasses a certain threshold, a cytotoxic T cell response is instructed, most likely intertwined with enhanced plasmacytic differentiation, which reduces the chances of high-affinity autoantibody generation in GCs. Triggering and engagement of this T cell checkpoint is finely tuned to the activation status and potential pathogenicity of the B cells, where hyperactive plasmacytic cells could be particularly prone to trigger cytotoxic immune surveillance. The induction of $CD4^+$ and $CD8^+$ sl-Tpex can explain the remarkable life-long persistence of the protective T cell response in mice. We thus propose a negative feedback immune checkpoint against B cell hyperreactivity, induced by the pathogenic B cells themselves with A20 acting as a key player in this checkpoint.

Loss and/or inactivation of A20 through chromosomal deletions, point mutations, epigenetic alterations, microRNAs (miRNAs), and other post-transcriptional mechanisms is a hallmark of Hodgkin and non-Hodgkin lymphoma.[60,61] In our studies, T cell-mediated protection against deadly malignancy arising from A20-deficient B cells remained intact upon additional overexpression of BCLxL, which occurs frequently in human non-Hodgkin lymphoma,[62] or of NIK, which arises in human lymphoma through chromosomal gains or translocation of NIK or loss of TRAF3.[60] This fits with observations of frequent A20 deficiency in human lymphomas arising in the context of immune deficiency, including posttransplant DLBCL[63] and AIDS-related lymphoma.[64] Our results thus define A20 as a haploinsufficient tumor suppressor in B cells and indicate that tight immune control can provide life-long protection against malignant disease.

The cytotoxic T cell responses elicited by A20-deficient NIK-overexpressing B cells contained features similar to those induced by LMP1-transformed B cells,[44] whose immune control does not require FAS[65] but relies on the perforin/granzyme killing machinery.[66] We observed the reverse for strongly hyperreactive ($B\text{-}Nik^{tg}\text{-}A20^{-/-}$) B cells, similar to the control of Blimp1-deficient or BCL6-overexpressing lymphomas.[14] Germline and acquired deficiencies in FAS are implicated in both autoimmunity and lymphoma,[4,7,67] as well as in the connection between the two.[68] In mice, lymphoproliferation of FAS-deficient B cells absolutely requires the presence of $\alpha\beta$T cells,[12] highlighting an obligate pathogenic role for T cell help in this context. By contrast, in our study, lymphoproliferation of strongly hyperreactive B cells occurred in the absence of T cells and could be prevented by protective T cell immune surveillance.

B cell-induced negative immune feedback control likely also affects later stages of human lymphomagenesis, as suggested by our demonstration that, in human FL, *TNFAIP3*/A20 inactivation directly correlates with mutations affecting the expression of *FAS*. In the context of autoimmunity, our data are consistent with reports on elevated cytotoxic $CD8^+$ T cells in children with SLE,[69] as well as elevated FASL expression on T cells[70] and anti-FASL autoantibodies[71] in SLE patients.

We propose that cytotoxic T cell-mediated negative feedback elimination, induced by and targeted against hyperactive B cells, is a fundamental aspect of adaptive immunity. This mechanism allows the immune system to control the devastating pathogenic potential of hyperactive B cells that probably constantly arise due to clonal expansion, developmental DNA damage, as well as acquired epigenetic and genetic alterations in the context of inherited susceptibilities. A20 haploinsufficiency may represent the peak of allowable B cell hyperreactivity that favors GC entry and remains sufficiently under the radar of the inducible T cell control, explaining its prevalence in autoimmunity. It is tempting to speculate that enhancing endogenous T cell responses against autoreactive B cells could be exploited for therapeutic purposes in autoimmunity.

Limitations of the study

Our results show that as B cells become increasingly hyperreactive to co-stimulatory signals, they shift the overall T cell response from the provision of help to cytotoxic immune surveillance. We did not investigate the involvement of auto-antigens, but we envision roles for the recently described B cell-derived autoantigens[72] and activation-induced autoantigens. While we describe a role for FASL:FAS-mediated killing in this process, we did not disentangle the individual contributions of different T cell subsets and additional mechanisms restraining the B cells. For example, we observed an induction of regulatory T cells by hyperreactive B cells, which could restrain anti-B cell T cell responses but could also act directly on the B cells. Finally, to what degree and how this mechanism impacts human autoimmunity and lymphoma biology warrants future study.

RESOURCE AVAILABILITY

Lead contact

Further information and requests for resources and reagents should be directed to and will be fulfilled by the lead contact, Dr. Marc Schmidt-Supprian (marc.supprian@tum.de).

Materials availability

This study did not generate new, unique reagents.

Data and code availability

- Bulk RNA-seq data and single-cell RNA-seq data have been deposited at ENA and are publicly available as of the date of publication. Microarray data have been submitted to GEO. Accession numbers are listed in the key resources table.
- This paper does not report original code.
- Any additional information required to reanalyze the data reported in this paper is available from the lead contact upon request.

ACKNOWLEDGMENTS

We thank C. Mugler, J. Knogler, M. Mittermeier, J. Schröder, V. Weber, T. Ries, O. Seelbach, M. Mielke, and A. Hering for excellent technical support; R. Trapp for help with mouse analyses; N. de Andrade Krätzig for data repository management; D. Krappmann and G. Schneider for advice/critical reading of the manuscript. We thank S. Kalled, J. Browning, and G.v. Loo for providing mice; H. Blum and S. Krebs for microarray processing; J. Finney and G. Kelsoe for Bach2-expressing retroviral plasmids; and D. Kitamura for 40LB and 40LB-FASL cells.

This study was supported by the following: The German Research Foundation (DFG) through project nos. 273068069, 232863826, 13759457, 435874434, 210592381, and 490846870 to M.S.-S.; 452844127 to M.S.-S. and O.W.; 387509280 to C. Daniel.; the ERC under the European Union's Horizon 2020 research and innovation program (grant agreement 682435) to M.S.-S.; and Else-Kröner Excellence Fellowship (Project-ID 2021_EKES.13) to O.W.

AUTHOR CONTRIBUTIONS

Conceptualization: M.S.-S., C. Diehl, V.S., S. Baygün, Y.C., and L.P.; methodology: R.Ö., R.R., S. Bärthel, and D.S.; investigation: C. Diehl, V.S., S. Baygün, Y.C., L.K., P.S., S.H., V.G., F.O.B., G.S., A.M.A., L.O., T.Z., Q.U.A., M.H., V.I., V.J., F.M.W., M.K.-H., J.M., D.D.-S, G.B., and M.F.; data analysis and interpretation: C. Diehl, V.S., S. Baygün, Y.C., M.S.-S., M.R., C. Daniel, M.H., M.L., K.S., T.E., V.P., L.K., S. Bortoluzzi, S. Bärthel, T.K., J.M., D.D.-S, G.B., M.F., L.P., and A.M.A.; funding acquisition: M.S.-S., O.W., K.S., C. Daniel, and L.P.; supervision: M.S.-S., J.P., F.M.W., D.S., R.R., O.W., and L.P.; writing: M.S.-S., C. Diehl, V.S., S. Baygün, and L.P.

DECLARATION OF INTERESTS

The authors declare no competing interests.

STAR★METHODS

Detailed methods are provided in the online version of this paper and include the following:

- KEY RESOURCES TABLE
- EXPERIMENTAL MODEL AND SUBJECT DETAILS
  - Mice
- METHOD DETAILS
  - Organ collection and fixation or single cell suspension generation
  - Flow cytometry
  - RNA flow cytometry (PrimeFlow)
  - Flow-cytometry based purification of cells
  - Tumor phenotype
  - ELISA
  - Albuminuria
  - Total protein content in urine
  - BUN
  - Legendplex assay
  - 3' RNA and single cell RNA sequencing
  - Lymphoma clonality assessment
  - Immunizations
  - Antibody injections
  - Bone marrow chimeras
  - Ferric(III)chloride induced thrombus formation in the murine carotid artery model
  - Histopathological analyses
  - iGB culture and FASL induced killing assay
  - *In vitro* cytotoxic T cell differentiation with primary B cells
  - *In vitro* killing assays
  - *In vitro* stimulation of B cells for RNA gene array analysis
  - 3' RNA and single cell RNA sequencing data analysis
  - Mutational analysis of follicular lymphoma
  - Generation of gene lists
- QUANTIFICATION AND STATISTICAL ANALYSIS

SUPPLEMENTAL INFORMATION

Supplemental information can be found online at https://doi.org/10.1016/j.immuni.2024.11.023.

Received: February 21, 2024
Revised: August 14, 2024
Accepted: November 26, 2024
Published: December 26, 2024

REFERENCES

1. Machado, H.E., Mitchell, E., Øbro, N.F., Kübler, K., Davies, M., Leongamornlert, D., Cull, A., Maura, F., Sanders, M.A., Cagan, A.T.J., et al. (2022). Diverse mutational landscapes in human lymphocytes. Nature *608*, 724–732. https://doi.org/10.1038/s41586-022-05072-7.
2. Zhang, L., Dong, X., Lee, M., Maslov, A.Y., Wang, T., and Vijg, J. (2019). Single-cell whole-genome sequencing reveals the functional landscape of somatic mutations in B lymphocytes across the human lifespan. Proc. Natl. Acad. Sci. USA *116*, 9014–9019. https://doi.org/10.1073/pnas.1902510116.
3. Nocturne, G., Boudaoud, S., Miceli-Richard, C., Viengchareun, S., Lazure, T., Nititham, J., Taylor, K.E., Ma, A., Busato, F., Melki, J., et al. (2013). Germline and somatic genetic variations of TNFAIP3 in lymphoma complicating primary Sjögren's syndrome. Blood *122*, 4068–4076. https://doi.org/10.1182/blood-2013-05-503383.
4. Magerus-Chatinet, A., Neven, B., Stolzenberg, M.-C., Daussy, C., Arkwright, P.D., Lanzarotti, N., Schaffner, C., Cluet-Dennetiere, S., Haerynck, F., Michel, G., et al. (2011). Onset of autoimmune lymphoproliferative syndrome (ALPS) in humans as a consequence of genetic defect accumulation. J. Clin. Invest. *121*, 106–112. https://doi.org/10.1172/JCI43752.
5. Vijg, J., and Dong, X. (2020). Pathogenic Mechanisms of Somatic Mutation and Genome Mosaicism in Aging. Cell *182*, 12–23. https://doi.org/10.1016/j.cell.2020.06.024.
6. Rawlings, D.J., Metzler, G., Wray-Dutra, M., and Jackson, S.W. (2017). Altered B cell signalling in autoimmunity. Nat. Rev. Immunol. *17*, 421–436. https://doi.org/10.1038/nri.2017.24.
7. Goodnow, C.C. (2007). Multistep pathogenesis of autoimmune disease. Cell *130*, 25–35. https://doi.org/10.1016/j.cell.2007.06.033.
8. Corneth, O.B.J., Neys, S.F.H., and Hendriks, R.W. (2022). Aberrant B Cell Signaling in Autoimmune Diseases. Cells *11*, 3391. https://doi.org/10.3390/cells11213391.
9. Edward B, M. (2018). Autoimmunity and Lymphoma: A Brief Review. J. Rheum. Dis. Treat. *4*, 062. https://doi.org/10.23937/2469-5726/1510062.
10. Singh, M., Jackson, K.J.L., Wang, J.J., Schofield, P., Field, M.A., Koppstein, D., Peters, T.J., Burnett, D.L., Rizzetto, S., Nevoltris, D., et al. (2020). Lymphoma Driver Mutations in the Pathogenic Evolution of an Iconic Human Autoantibody. Cell *180*, 878–894.e19. https://doi.org/10.1016/j.cell.2020.01.029.
11. Bende, R.J., Slot, L.M., Kwakkenbos, M.J., Wormhoudt, T.A.M., Jongejan, A., Verstappen, G.M., van Kampen, A.C.M., Guikema, J.E.J., Kroese, F.G.M., and van Noesel, C.J.M. (2023). Lymphoma-associated mutations in autoreactive memory B cells of patients with Sjögren's syndrome. J. Pathol. *259*, 264–275. https://doi.org/10.1002/path.6039.
12. Hao, Z., Duncan, G.S., Seagal, J., Su, Y.-W., Hong, C., Haight, J., Chen, N.-J., Elia, A., Wakeham, A., Li, W.Y., et al. (2008). Fas receptor expression in germinal-center B cells is essential for T and B lymphocyte homeostasis. Immunity *29*, 615–627. https://doi.org/10.1016/j.immuni.2008.07.016.
13. Boice, M., Salloum, D., Mourcin, F., Sanghvi, V., Amin, R., Oricchio, E., Jiang, M., Mottok, A., Denis-Lagache, N., Ciriello, G., et al. (2016). Loss of the HVEM Tumor Suppressor in Lymphoma and Restoration by

Modified CAR-T Cells. Cell *167*, 405–418.e13. https://doi.org/10.1016/j.cell.2016.08.032.

14. Afshar-Sterle, S., Zotos, D., Bernard, N.J., Scherger, A.K., Rödling, L., Alsop, A.E., Walker, J., Masson, F., Belz, G.T., Corcoran, L.M., et al. (2014). Fas ligand-mediated immune surveillance by T cells is essential for the control of spontaneous B cell lymphomas. Nat. Med. *20*, 283–290. https://doi.org/10.1038/nm.3442.
15. Scott, D.W., and Gascoyne, R.D. (2014). The tumour microenvironment in B cell lymphomas. Nat. Rev. Cancer *14*, 517–534. https://doi.org/10.1038/nrc3774.
16. Fangazio, M., Ladewig, E., Gomez, K., Garcia-Ibanez, L., Kumar, R., Teruya-Feldstein, J., Rossi, D., Filip, I., Pan-Hammarström, Q., Inghirami, G., et al. (2021). Genetic mechanisms of HLA-I loss and immune escape in diffuse large B cell lymphoma. Proc. Natl. Acad. Sci. USA *118*, e2104504118. https://doi.org/10.1073/pnas.2104504118.
17. Shembade, N., Ma, A., and Harhaj, E.W. (2010). Inhibition of NF-kappaB signaling by A20 through disruption of ubiquitin enzyme complexes. Science *327*, 1135–1139. https://doi.org/10.1126/science.1182364.
18. Martens, A., and van Loo, G. (2020). A20 at the Crossroads of Cell Death, Inflammation, and Autoimmunity. Cold Spring Harb. Perspect. Biol. *12*, a036418. https://doi.org/10.1101/cshperspect.a036418.
19. Kato, M., Sanada, M., Kato, I., Sato, Y., Takita, J., Takeuchi, K., Niwa, A., Chen, Y., Nakazaki, K., Nomoto, J., et al. (2009). Frequent inactivation of A20 in B-cell lymphomas. Nature *459*, 712–716. https://doi.org/10.1038/nature07969.
20. Novak, U., Rinaldi, A., Kwee, I., Nandula, S.V., Rancoita, P.M.V., Compagno, M., Cerri, M., Rossi, D., Murty, V.V., Zucca, E., et al. (2009). The NF-κB negative regulator TNFAIP3 (A20) is inactivated by somatic mutations and genomic deletions in marginal zone lymphomas. Blood *113*, 4918–4921. https://doi.org/10.1182/blood-2008-08-174110.
21. Compagno, M., Lim, W.K., Grunn, A., Nandula, S.V., Brahmachary, M., Shen, Q., Bertoni, F., Ponzoni, M., Scandurra, M., Califano, A., et al. (2009). Mutations of multiple genes cause deregulation of NF-kappaB in diffuse large B-cell lymphoma. Nature *459*, 717–721. https://doi.org/10.1038/nature07968.
22. Musone, S.L., Taylor, K.E., Lu, T.T., Nititham, J., Ferreira, R.C., Ortmann, W., Shifrin, N., Petri, M.A., Kamboh, M.I., Manzi, S., et al. (2008). Multiple polymorphisms in the TNFAIP3 region are independently associated with systemic lupus erythematosus. Nat. Genet. *40*, 1062–1064. https://doi.org/10.1038/ng.202.
23. Graham, R.R., Cotsapas, C., Davies, L., Hackett, R., Lessard, C.J., Leon, J.M., Burtt, N.P., Guiducci, C., Parkin, M., Gates, C., et al. (2008). Genetic variants near TNFAIP3 on 6q23 are associated with systemic lupus erythematosus. Nat. Genet. *40*, 1059–1061. https://doi.org/10.1038/ng.200.
24. Schmitz, R., Hansmann, M.-L., Bohle, V., Martin-Subero, J.I., Hartmann, S., Mechtersheimer, G., Klapper, W., Vater, I., Giefing, M., Gesk, S., et al. (2009). TNFAIP3 (A20) is a tumor suppressor gene in Hodgkin lymphoma and primary mediastinal B cell lymphoma. J. Exp. Med. *206*, 981–989. https://doi.org/10.1084/jem.20090528.
25. Chu, Y., Vahl, J.C., Kumar, D., Heger, K., Bertossi, A., Wójtowicz, E., Soberon, V., Schenten, D., Mack, B., Reutelshöfer, M., et al. (2011). B cells lacking the tumor suppressor TNFAIP3/A20 display impaired differentiation and hyperactivation and cause inflammation and autoimmunity in aged mice. Blood *117*, 2227–2236. https://doi.org/10.1182/blood-2010-09-306019.
26. Hövelmeyer, N., Reissig, S., Xuan, N.T., Adams-Quack, P., Lukas, D., Nikolaev, A., Schlüter, D., and Waisman, A. (2011). A20 deficiency in B cells enhances B-cell proliferation and results in the development of autoantibodies. Eur. J. Immunol. *41*, 595–601. https://doi.org/10.1002/eji.201041313.
27. Tavares, R.M., Turer, E.E., Liu, C.L., Advincula, R., Scapini, P., Rhee, L., Barrera, J., Lowell, C.A., Utz, P.J., Malynn, B.A., et al. (2010). The ubiquitin modifying enzyme A20 restricts B cell survival and prevents autoimmunity. Immunity *33*, 181–191. https://doi.org/10.1016/j.immuni.2010.07.017.
28. Schmitz, R., Wright, G.W., Huang, D.W., Johnson, C.A., Phelan, J.D., Wang, J.Q., Roulland, S., Kasbekar, M., Young, R.M., Shaffer, A.L., et al. (2018). Genetics and Pathogenesis of Diffuse Large B-Cell Lymphoma. N. Engl. J. Med. *378*, 1396–1407. https://doi.org/10.1056/NEJMoa1801445.
29. Cattoretti, G., Pasqualucci, L., Ballon, G., Tam, W., Nandula, S.V., Shen, Q., Mo, T., Murty, V.V., and Dalla-Favera, R. (2005). Deregulated BCL6 expression recapitulates the pathogenesis of human diffuse large B cell lymphomas in mice. Cancer Cell *7*, 445–455. https://doi.org/10.1016/j.ccr.2005.03.037.
30. Nezos, A., Gkioka, E., Koutsilieris, M., Voulgarelis, M., Tzioufas, A.G., and Mavragani, C.P. (2018). TNFAIP3 F127C Coding Variation in Greek Primary Sjogren's Syndrome Patients. J. Immunol. Res. *2018*, 6923213. https://doi.org/10.1155/2018/6923213.
31. Jiwrajka, N., and Anguera, M.C. (2022). The X in seX-biased immunity and autoimmune rheumatic disease. J. Exp. Med. *219*, e20211487. https://doi.org/10.1084/jem.20211487.
32. Nojima, T., Haniuda, K., Moutai, T., Matsudaira, M., Mizokawa, S., Shiratori, I., Azuma, T., and Kitamura, D. (2011). In-vitro derived germinal centre B cells differentially generate memory B or plasma cells in vivo. Nat. Commun. *2*, 465. https://doi.org/10.1038/ncomms1475.
33. Moutai, T., Yamana, H., Nojima, T., and Kitamura, D. (2014). A novel and effective cancer immunotherapy mouse model using antigen-specific B cells selected in vitro. PLoS One *9*, e92732. https://doi.org/10.1371/journal.pone.0092732.
34. Becker-Merok, A., Eilertsen, G.Ø., and Nossent, J.C. (2010). Levels of transforming growth factor-beta are low in systemic lupus erythematosus patients with active disease. J. Rheumatol. *37*, 2039–2045. https://doi.org/10.3899/jrheum.100180.
35. Chun, H.-Y., Chung, J.-W., Kim, H.-A., Yun, J.-M., Jeon, J.-Y., Ye, Y.-M., Kim, S.-H., Park, H.-S., and Suh, C.-H. (2007). Cytokine IL-6 and IL-10 as Biomarkers in Systemic Lupus Erythematosus. J. Clin. Immunol. *27*, 461–466. https://doi.org/10.1007/s10875-007-9104-0.
36. Muramatsu, M., Kinoshita, K., Fagarasan, S., Yamada, S., Shinkai, Y., and Honjo, T. (2000). Class Switch Recombination and Hypermutation Require Activation-Induced Cytidine Deaminase (AID), a Potential RNA Editing Enzyme. Cell *102*, 553–563. https://doi.org/10.1016/s0092-8674(00)00078-7.
37. Möckel, T., Basta, F., Weinmann-Menke, J., and Schwarting, A. (2021). B cell activating factor (BAFF): Structure, functions, autoimmunity and clinical implications in Systemic Lupus Erythematosus (SLE). Autoimmun. Rev. *20*, 102736. https://doi.org/10.1016/j.autrev.2020.102736.
38. Mackay, F., Woodcock, S.A., Lawton, P., Ambrose, C., Baetscher, M., Schneider, P., Tschopp, J., and Browning, J.L. (1999). Mice transgenic for BAFF develop lymphocytic disorders along with autoimmune manifestations. J. Exp. Med. *190*, 1697–1710. https://doi.org/10.1084/jem.190.11.1697.
39. McCarthy, D.D., Kujawa, J., Wilson, C., Papandile, A., Poreci, U., Porfilio, E.A., Ward, L., Lawson, M.A.E., Macpherson, A.J., McCoy, K.D., et al. (2011). Mice overexpressing BAFF develop a commensal flora–dependent, IgA-associated nephropathy. J. Clin. Invest. *121*, 3991–4002. https://doi.org/10.1172/JCI45563.
40. Steri, M., Orrù, V., Idda, M.L., Pitzalis, M., Pala, M., Zara, I., Sidore, C., Faà, V., Floris, M., Deiana, M., et al. (2017). Overexpression of the Cytokine BAFF and Autoimmunity Risk. N. Engl. J. Med. *376*, 1615–1626. https://doi.org/10.1056/NEJMoa1610528.
41. Sasaki, Y., Calado, D.P., Derudder, E., Zhang, B., Shimizu, Y., Mackay, F., Nishikawa, S., Rajewsky, K., and Schmidt-Supprian, M. (2008). NIK overexpression amplifies, whereas ablation of its TRAF3-binding domain replaces BAFF:BAFF-R-mediated survival signals in B cells. Proc. Natl. Acad. Sci. USA *105*, 10883–10888. https://doi.org/10.1073/pnas.0805186105.
42. Zhang, B., Calado, D.P., Wang, Z., Fröhler, S., Köchert, K., Qian, Y., Koralov, S.B., Schmidt-Supprian, M., Sasaki, Y., Unitt, C., et al. (2015). An Oncogenic Role for Alternative NF-κB Signaling in DLBCL Revealed

upon Deregulated BCL6 Expression. Cell Rep. *11*, 715–726. https://doi.org/10.1016/j.celrep.2015.03.059.

43. Heger, K., Kober, M., Rieß, D., Drees, C., de Vries, I., Bertossi, A., Roers, A., Sixt, M., and Schmidt-Supprian, M. (2015). A novel Cre recombinase reporter mouse strain facilitates selective and efficient infection of primary immune cells with adenoviral vectors. Eur. J. Immunol. *45*, 1614–1620. https://doi.org/10.1002/eji.201545457.

44. Choi, I.-K., Wang, Z., Ke, Q., Hong, M., Paul, D.W., Fernandes, S.M., Hu, Z., Stevens, J., Guleria, I., Kim, H.-J., et al. (2021). Mechanism of EBV inducing anti-tumour immunity and its therapeutic use. Nature *590*, 157–162. https://doi.org/10.1038/s41586-020-03075-w.

45. Tsui, C., Kretschmer, L., Rapelius, S., Gabriel, S.S., Chisanga, D., Knöpper, K., Utzschneider, D.T., Nüssing, S., Liao, Y., Mason, T., et al. (2022). MYB orchestrates T cell exhaustion and response to checkpoint inhibition. Nature *609*, 354–360. https://doi.org/10.1038/s41586-022-05105-1.

46. Choi, I.-K., Wang, Z., Ke, Q., Hong, M., Qian, Y., Zhao, X., Liu, Y., Kim, H.-J., Ritz, J., Cantor, H., et al. (2018). Signaling by the Epstein–Barr virus LMP1 protein induces potent cytotoxic CD4+ and CD8+ T cell responses. Proc. Natl. Acad. Sci. USA *115*, E686–E695. https://doi.org/10.1073/pnas.1713607115.

47. Jurinovic, V., Kridel, R., Staiger, A.M., Szczepanowski, M., Horn, H., Dreyling, M.H., Rosenwald, A., Ott, G., Klapper, W., Zelenetz, A.D., et al. (2016). Clinicogenetic risk models predict early progression of follicular lymphoma after first-line immunochemotherapy. Blood *128*, 1112–1120. https://doi.org/10.1182/blood-2016-05-717355.

48. Pastore, A., Jurinovic, V., Kridel, R., Hoster, E., Staiger, A.M., Szczepanowski, M., Pott, C., Kopp, N., Murakami, M., Horn, H., et al. (2015). Integration of gene mutations in risk prognostication for patients receiving first-line immunochemotherapy for follicular lymphoma: a retrospective analysis of a prospective clinical trial and validation in a population-based registry. Lancet Oncol. *16*, 1111–1122. https://doi.org/10.1016/S1470-2045(15)00169-2.

49. Ross, C.W., Ouillette, P.D., Saddler, C.M., Shedden, K.A., and Malek, S.N. (2007). Comprehensive Analysis of Copy Number and Allele Status Identifies Multiple Chromosome Defects Underlying Follicular Lymphoma Pathogenesis. Clin. Cancer Res. *13*, 4777–4785. https://doi.org/10.1158/1078-0432.CCR-07-0456.

50. Okosun, J., Bödör, C., Wang, J., Araf, S., Yang, C.-Y., Pan, C., Boller, S., Cittaro, D., Bozek, M., Iqbal, S., et al. (2014). Integrated genomic analysis identifies recurrent mutations and evolution patterns driving the initiation and progression of follicular lymphoma. Nat. Genet. *46*, 176–181. https://doi.org/10.1038/ng.2856.

51. Kridel, R., Sehn, L.H., and Gascoyne, R.D. (2012). Pathogenesis of follicular lymphoma. J. Clin. Invest. *122*, 3424–3431. https://doi.org/10.1172/JCI63186.

52. Antoniolli, M., Solovey, M., Bararia, D., Strobl, C.D., Keay, W.D., Hildebrand, J.A., Heide, M., Passerini, V., Wange, L., Enard, W., et al. (2021). ARID1A Controls a Novel Transcriptional Network Regulating FAS in Follicular Lymphoma. Blood *138* (*Suppl 1*), 3492. https://doi.org/10.1182/blood-2021-148862.

53. Wardemann, H., Yurasov, S., Schaefer, A., Young, J.W., Meffre, E., and Nussenzweig, M.C. (2003). Predominant Autoantibody Production by Early Human B Cell Precursors. Science *301*, 1374–1377. https://doi.org/10.1126/science.1086907.

54. Zammit, N.W., Siggs, O.M., Gray, P.E., Horikawa, K., Langley, D.B., Walters, S.N., Daley, S.R., Loetsch, C., Warren, J., Yap, J.Y., et al. (2019). Denisovan, modern human and mouse TNFAIP3 alleles tune A20 phosphorylation and immunity. Nat. Immunol. *20*, 1299–1310. https://doi.org/10.1038/s41590-019-0492-0.

55. Yu, M.-P., Xu, X.-S., Zhou, Q., Deuitch, N., and Lu, M.-P. (2020). Haploinsufficiency of A20 (HA20): updates on the genetics, phenotype, pathogenesis and treatment. World J. Pediatr. *16*, 575–584. https://doi.org/10.1007/s12519-019-00288-6.

56. Sokhi, U.K., Liber, M.P., Frye, L., Park, S., Kang, K., Pannellini, T., Zhao, B., Norinsky, R., Ivashkiv, L.B., and Gong, S. (2018). Dissection and function of autoimmunity-associated TNFAIP3 (A20) gene enhancers in humanized mouse models. Nat. Commun. *9*, 658. https://doi.org/10.1038/s41467-018-03081-7.

57. Souyris, M., Cenac, C., Azar, P., Daviaud, D., Canivet, A., Grunenwald, S., Pienkowski, C., Chaumeil, J., Mejía, J.E., and Guéry, J.-C. (2018). TLR7 escapes X chromosome inactivation in immune cells. Sci. Immunol. *3*, eaap8855. https://doi.org/10.1126/sciimmunol.aap8855.

58. Yu, B., Qi, Y., Li, R., Shi, Q., Satpathy, A.T., and Chang, H.Y. (2021). B cell-specific XIST complex enforces X-inactivation and restrains atypical B cells. Cell *184*, 1790–1803.e17. https://doi.org/10.1016/j.cell.2021.02.015.

59. Pyfrom, S., Paneru, B., Knox, J.J., Cancro, M.P., Posso, S., Buckner, J.H., and Anguera, M.C. (2021). The dynamic epigenetic regulation of the inactive X chromosome in healthy human B cells is dysregulated in lupus patients. Proc. Natl. Acad. Sci. USA *118*, e2024624118. https://doi.org/10.1073/pnas.2024624118.

60. Pasqualucci, L., and Klein, U. (2022). NF-κB Mutations in Germinal Center B-Cell Lymphomas: Relation to NF-κB Function in Normal B Cells. Biomedicines *10*, 2450. https://doi.org/10.3390/biomedicines10102450.

61. Ortega-Molina, A., Boss, I.W., Canela, A., Pan, H., Jiang, Y., Zhao, C., Jiang, M., Hu, D., Agirre, X., Niesvizky, I., et al. (2015). The histone lysine methyltransferase KMT2D sustains a gene expression program that represses B cell lymphoma development. Nat. Med. *21*, 1199–1208. https://doi.org/10.1038/nm.3943.

62. Adams, C.M., Mitra, R., Gong, J.Z., and Eischen, C.M. (2017). Non-Hodgkin and Hodgkin Lymphomas Select for Overexpression of BCLW. Clin. Cancer Res. *23*, 7119–7129. https://doi.org/10.1158/1078-0432.CCR-17-1144.

63. Ferreiro, J.F., Morscio, J., Dierickx, D., Vandenberghe, P., Gheysens, O., Verhoef, G., Zamani, M., Tousseyn, T., and Wlodarska, I. (2016). EBV-Positive and EBV-Negative Posttransplant Diffuse Large B Cell Lymphomas Have Distinct Genomic and Transcriptomic Features. Am. J. Transplant. *16*, 414–425. https://doi.org/10.1111/ajt.13558.

64. Giulino, L., Mathew, S., Ballon, G., Chadburn, A., Barouk, S., Antonicelli, G., Leoncini, L., Liu, Y.F., Gogineni, S., Tam, W., et al. (2011). A20 (TNFAIP3) genetic alterations in EBV-associated AIDS-related lymphoma. Blood *117*, 4852–4854. https://doi.org/10.1182/blood-2010-10-310995.

65. Zhang, B., Kracker, S., Yasuda, T., Casola, S., Vanneman, M., Hömig-Hölzel, C., Wang, Z., Derudder, E., Li, S., Chakraborty, T., et al. (2012). Immune surveillance and therapy of lymphomas driven by Epstein-Barr virus protein LMP1 in a mouse model. Cell *148*, 739–751. https://doi.org/10.1016/j.cell.2011.12.031.

66. Wirtz, T., Weber, T., Kracker, S., Sommermann, T., Rajewsky, K., and Yasuda, T. (2016). Mouse model for acute Epstein–Barr virus infection. Proc. Natl. Acad. Sci. USA *113*, 13821–13826. https://doi.org/10.1073/pnas.1616574113.

67. Mizuno, T., Zhong, X., and Rothstein, T.L. (2003). Fas-induced apoptosis in B cells. Apoptosis *8*, 451–460. https://doi.org/10.1023/a:1025534223168.

68. Grønbaek, K., Straten, P.T., Ralfkiaer, E., Ahrenkiel, V., Andersen, M.K., Hansen, N.E., Zeuthen, J., Hou-Jensen, K., and Guldberg, P. (1998). Somatic Fas mutations in non-Hodgkin's lymphoma: association with extranodal disease and autoimmunity. Blood *92*, 3018–3024.

69. Nehar-Belaid, D., Hong, S., Marches, R., Chen, G., Bolisetty, M., Baisch, J., Walters, L., Punaro, M., Rossi, R.J., Chung, C.-H., et al. (2020). Mapping systemic lupus erythematosus heterogeneity at the single-cell level. Nat. Immunol. *21*, 1094–1106. https://doi.org/10.1038/s41590-020-0743-0.

70. Kovacs, B., Liossis, S.N., Dennis, G.J., and Tsokos, G.C. (1997). Increased Expression of Functional Fas-Ligand in Activated T Cells from Patients with Systemic Lupus Erythematosus. Autoimmunity *25*, 213–221. https://doi.org/10.3109/08916939708994730.

71. Suzuki, N., Ichino, M., Mihara, S., Kaneko, S., and Sakane, T. (1998). Inhibition of FAS/FAS ligand-mediated apoptotic cell death of lymphocytes in vitro by circulating anti-FAS ligand autoantibodies in patients with systemic lupus erythematosus. Arthritis Rheum. *41*, 344–353. https://doi.org/10.1002/1529-0131(199802)41:2<344::AID-ART19>3.0.CO;2-J.

72. Lin, Y., Wan, Z., Liu, B., Yao, J., Li, T., Yang, F., Sui, J., Zhao, Y., Liu, W., Zhou, X., et al. (2024). B cell-reactive triad of B cells, follicular helper and regulatory T cells at homeostasis. Cell Res. *34*, 295–308. https://doi.org/10.1038/s41422-024-00929-0.

73. Nakagawa, M.M., Thummar, K., Mandelbaum, J., Pasqualucci, L., and Rathinam, C.V. (2015). Lack of the ubiquitin-editing enzyme A20 results in loss of hematopoietic stem cell quiescence. J. Exp. Med. *212*, 203–216. https://doi.org/10.1084/jem.20132544.

74. Vereecke, L., Sze, M., Mc Guire, C.M., Rogiers, B., Chu, Y., Schmidt-Supprian, M., Pasparakis, M., Beyaert, R., and van Loo, G. (2010). Enterocyte-specific A20 deficiency sensitizes to tumor necrosis factor–induced toxicity and experimental colitis. J. Exp. Med. *207*, 1513–1523. https://doi.org/10.1084/jem.20092474.

75. Grillot, D.A., Merino, R., Pena, J.C., Fanslow, W.C., Finkelman, F.D., Thompson, C.B., and Nunez, G. (1996). bcl-x exhibits regulated expression during B cell development and activation and modulates lymphocyte survival in transgenic mice. J. Exp. Med. *183*, 381–391. https://doi.org/10.1084/jem.183.2.381.

76. Rickert, R.C., Roes, J., and Rajewsky, K. (1997). B lymphocyte-specific, Cre-mediated mutagenesis in mice. Nucleic Acids Res. *25*, 1317–1318. https://doi.org/10.1093/nar/25.6.1317.

77. Casola, S., Cattoretti, G., Uyttersprot, N., Koralov, S.B., Seagal, J., Hao, Z., Waisman, A., Egert, A., Ghitza, D., and Rajewsky, K. (2006). Tracking germinal center B cells expressing germ-line immunoglobulin gamma1 transcripts by conditional gene targeting. Proc. Natl. Acad. Sci. USA *103*, 7396–7401. https://doi.org/10.1073/pnas.0602353103.

78. Malissen, M., Gillet, A., Ardouin, L., Bouvier, G., Trucy, J., Ferrier, P., Vivier, E., and Malissen, B. (1995). Altered T cell development in mice with a targeted mutation of the CD3-epsilon gene. EMBO J. *14*, 4641–4653. https://doi.org/10.1002/j.1460-2075.1995.tb00146.x.

79. Kägi, D., Ledermann, B., Bürki, K., Seiler, P., Odermatt, B., Olsen, K.J., Podack, E.R., Zinkernagel, R.M., and Hengartner, H. (1994). Cytotoxicity mediated by T cells and natural killer cells is greatly impaired in perforin-deficient mice. Nature *369*, 31–37. https://doi.org/10.1038/369031a0.

80. Schmidt-Supprian, M., Tian, J., Ji, H., Terhorst, C., Bhan, A.K., Grant, E.P., Pasparakis, M., Casola, S., Coyle, A.J., and Rajewsky, K. (2004). I kappa B kinase 2 deficiency in T cells leads to defects in priming, B cell help, germinal center reactions, and homeostatic expansion. J. Immunol. *173*, 1612–1619. https://doi.org/10.4049/jimmunol.173.3.1612.

81. Kober-Hasslacher, M., Oh-Strauß, H., Kumar, D., Soberon, V., Diehl, C., Lech, M., Engleitner, T., Katab, E., Fernández-Sáiz, V., Piontek, G., et al. (2020). c-Rel gain in B cells drives germinal center reactions and autoantibody production. J. Clin. Invest. *130*, 3270–3286. https://doi.org/10.1172/JCI124382.

82. Parekh, S., Ziegenhain, C., Vieth, B., Enard, W., and Hellmann, I. (2016). The impact of amplification on differential expression analyses by RNA-seq. Sci. Rep. *6*, 25533. https://doi.org/10.1038/srep25533.

83. Macosko, E.Z., Basu, A., Satija, R., Nemesh, J., Shekhar, K., Goldman, M., Tirosh, I., Bialas, A.R., Kamitaki, N., Martersteck, E.M., et al. (2015). Highly Parallel Genome-wide Expression Profiling of Individual Cells Using Nanoliter Droplets. Cell *161*, 1202–1214. https://doi.org/10.1016/j.cell.2015.05.002.

84. Arnaout, R., Lee, W., Cahill, P., Honan, T., Sparrow, T., Weiand, M., Nusbaum, C., Rajewsky, K., and Koralov, S.B. (2011). High-resolution description of antibody heavy-chain repertoires in humans. PLoS One *6*, e22365. https://doi.org/10.1371/journal.pone.0022365.

85. Calado, D.P., Zhang, B., Srinivasan, L., Sasaki, Y., Seagal, J., Unitt, C., Rodig, S., Kutok, J., Tarakhovsky, A., Schmidt-Supprian, M., et al. (2010). Constitutive Canonical NF-κB Activation Cooperates with Disruption of BLIMP1 in the Pathogenesis of Activated B Cell-like Diffuse Large Cell Lymphoma. Cancer Cell *18*, 580–589. https://doi.org/10.1016/j.ccr.2010.11.024.

86. Schenten, D., Nish, S.A., Yu, S., Yan, X., Lee, H.K., Brodsky, I., Pasman, L., Yordy, B., Wunderlich, F.T., Brüning, J.C., et al. (2014). Signaling through the Adaptor Molecule MyD88 in CD4$^+$ T Cells Is Required to Overcome Suppression by Regulatory T Cells. Immunity *40*, 78–90. https://doi.org/10.1016/j.immuni.2013.10.023.

87. Mandelbaum, J., Bhagat, G., Tang, H., Mo, T., Brahmachary, M., Shen, Q., Chadburn, A., Rajewsky, K., Tarakhovsky, A., Pasqualucci, L., et al. (2010). BLIMP1 is a tumor suppressor gene frequently disrupted in activated B cell-like diffuse large B cell lymphoma. Cancer Cell *18*, 568–579. https://doi.org/10.1016/j.ccr.2010.10.030.

88. Morse, H.C., Anver, M.R., Fredrickson, T.N., Haines, D.C., Harris, A.W., Harris, N.L., Jaffe, E.S., Kogan, S.C., MacLennan, I.C.M., Pattengale, P.K., et al. (2002). Bethesda proposals for classification of lymphoid neoplasms in mice. Blood *100*, 246–258. https://doi.org/10.1182/blood.v100.1.246.

89. Rehg, J.E., Bush, D., and Ward, J.M. (2012). The Utility of Immunohistochemistry for the Identification of Hematopoietic and Lymphoid Cells in Normal Tissues and Interpretation of Proliferative and Inflammatory Lesions of Mice and Rats. Toxicol. Pathol. *40*, 345–374. https://doi.org/10.1177/0192623311430695.

90. Willard-Mack, C.L., Elmore, S.A., Hall, W.C., Harleman, J., Kuper, C.F., Losco, P., Rehg, J.E., Rühl-Fehlert, C., Ward, J.M., Weinstock, D., et al. (2019). Nonproliferative and Proliferative Lesions of the Rat and Mouse Hematolymphoid System. Toxicol. Pathol. *47*, 665–783. https://doi.org/10.1177/0192623319867053.

91. Finney, J., and Kelsoe, G. (2021). Continuous Culture of Mouse Primary B Lymphocytes by Forced Expression of Bach2. J. Immunol. *207*, 1478–1492. https://doi.org/10.4049/jimmunol.2100172.

92. Ritchie, M.E., Phipson, B., Wu, D., Hu, Y., Law, C.W., Shi, W., and Smyth, G.K. (2015). limma powers differential expression analyses for RNA-sequencing and microarray studies. Nucleic Acids Res. *43*, e47. https://doi.org/10.1093/nar/gkv007.

93. Wu, D., Lim, E., Vaillant, F., Asselin-Labat, M.-L., Visvader, J.E., and Smyth, G.K. (2010). ROAST: rotation gene set tests for complex microarray experiments. Bioinformatics *26*, 2176–2182. https://doi.org/10.1093/bioinformatics/btq401.

94. Subramanian, A., Tamayo, P., Mootha, V.K., Mukherjee, S., Ebert, B.L., Gillette, M.A., Paulovich, A., Pomeroy, S.L., Golub, T.R., Lander, E.S., et al. (2005). Gene set enrichment analysis: a knowledge-based approach for interpreting genome-wide expression profiles. Proc. Natl. Acad. Sci. USA *102*, 15545–15550. https://doi.org/10.1073/pnas.0506580102.

95. Gautier, L., Cope, L., Bolstad, B.M., and Irizarry, R.A. (2004). affy—analysis of Affymetrix GeneChip data at the probe level. Bioinformatics *20*, 307–315. https://doi.org/10.1093/bioinformatics/btg405.

96. Hiddemann, W., and Cheson, B.D. (2014). How we manage follicular lymphoma. Leukemia *28*, 1388–1395. https://doi.org/10.1038/leu.2014.91.

97. Marcus, R., Davies, A., Ando, K., Klapper, W., Opat, S., Owen, C., Phillips, E., Sangha, R., Schlag, R., Seymour, J.F., et al. (2017). Obinutuzumab for the First-Line Treatment of Follicular Lymphoma. N. Engl. J. Med. *377*, 1331–1344. https://doi.org/10.1056/NEJMoa1614598.

98. Talevich, E., Shain, A.H., Botton, T., and Bastian, B.C. (2016). CNVkit: Genome-Wide Copy Number Detection and Visualization from Targeted DNA Sequencing. PLoS Comput. Biol. *12*, e1004873. https://doi.org/10.1371/journal.pcbi.1004873.

99. Shen, P., Roch, T., Lampropoulou, V., O'Connor, R.A., Stervbo, U., Hilgenberg, E., Ries, S., Dang, V.D., Jaimes, Y., Daridon, C., et al. (2014). IL-35-producing B cells are critical regulators of immunity during autoimmune and infectious diseases. Nature *507*, 366–370. https://doi.org/10.1038/nature12979.

100. Alfei, F., Kanev, K., Hofmann, M., Wu, M., Ghoneim, H.E., Roelli, P., Utzschneider, D.T., von Hoesslin, M., Cullen, J.G., Fan, Y., et al. (2019). TOX reinforces the phenotype and longevity of exhausted T cells in

chronic viral infection. Nature *571*, 265–269. https://doi.org/10.1038/s41586-019-1326-9.

101. Bortoluzzi, S., Dashtsoodol, N., Engleitner, T., Drees, C., Helmrath, S., Mir, J., Toska, A., Flossdorf, M., Öllinger, R., Solovey, M., et al. (2021). Brief homogeneous TCR signals instruct common iNKT progenitors whose effector diversification is characterized by subsequent cytokine signaling. Immunity *54*, 2497–2513.e9. https://doi.org/10.1016/j.immuni.2021.09.003.

102. Nakagawa, M.M., and Rathinam, C.V. (2019). A20 deficiency in hematopoietic stem cells causes lymphopenia and myeloproliferation due to elevated Interferon-γ signals. Sci. Rep. *9*, 12658. https://doi.org/10.1038/s41598-019-49038-8.

103. Robbiani, D.F., Bothmer, A., Callen, E., Reina-San-Martin, B., Dorsett, Y., Difilippantonio, S., Bolland, D.J., Chen, H.T., Corcoran, A.E., Nussenzweig, A., et al. (2008). AID is required for the chromosomal breaks in c-myc that lead to c-myc/IgH translocations. Cell *135*, 1028–1038. https://doi.org/10.1016/j.cell.2008.09.062.

104. Love, M.I., Huber, W., and Anders, S. (2014). Moderated estimation of fold change and dispersion for RNA-seq data with DESeq2. Genome Biol. *15*, 550. https://doi.org/10.1186/s13059-014-0550-8.

STAR★METHODS

KEY RESOURCES TABLE

REAGENT or RESOURCE	SOURCE	IDENTIFIER
Antibodies		
Anti-mouse 4-1BB Ligand (CD137L) Biotin	BioLegend	Cat#: 107103; RRID:AB_313304
Anti-mouse Albumin	Bethyl Laboratories	Cat#: A90-134A; RRID:AB_2891982
Anti-mouse Albumin HRP Conjugate	Bethyl Laboratories	Cat#: A90-134P; RRID:AB_67127
Anti-mouse B220 purified	BD	Cat#: 550286; RRID:AB_393581
Anti-mouse/human B220 purified	BD	Cat#: 553084; RRID:AB_394614
Anti-mouse/human B220 BV510	BioLegend	Cat#: 103248; RRID:AB_2650679
Anti-mouse/human B220 BV650	BioLegend	Cat#: 103241; RRID:AB_2738720
Anti-mouse B220 eFluor 450	eBioscience	Cat#: 48-0452-82; RRID:AB_1548761
Anti-mouse B220 FITC	eBioscience	Cat#: 11-0452-63; RRID:AB_465052
Anti-mouse B220 PE	eBioscience	Cat#: 12-0452-83; RRID:AB_465672
Anti-mouse B220 PE/Cy7	eBioscience	Cat#: 25-0452-82; RRID:AB_469627
Anti-mouse/human B220 PerCP-Cy5.5	eBioscience	Cat#: 45-0452-82; RRID:AB_1107006
Anti-mouse/human Bcl-6 purified	Cell Signaling Technology	Cat# 5650, RRID:AB_10949970
Anti-mouse Bcl-6 purified	Santa Cruz	Cat#: sc-858; RRID:AB_2063450
Anti-mouse Bcl-6 PE	BD	Cat#: 561522; RRID:AB_10717126
Anti-mouse Bcl-6 PE/Cy7	BD	Cat#: 563582; RRID:AB_2738292
Anti-human Bcl-xL PE	SouthernBiotech	Cat#: 10030-09; RRID:AB_2794104
Anti-mouse Blimp1 BV421	BD	Cat#: 564270; RRID:AB_2738720
Anti-mouse Blimp1 PE	BioLegend	Cat#: 150005; RRID:AB_2565991
Anti-mouse/human Active Caspase-3 PE	BD	Cat#: 570183; RRID:AB_393906
Anti-mouse CD119 (IFN gamma receptor 1) Biotin	eBioscience	Cat#: 13-1191-82; RRID:AB_2572773
Anti-mouse CD119 (IFN gamma receptor 1) PE	eBioscience	Cat#: 12-1191-80; RRID:AB_1210730
Anti-mouse CD11b Biotin	eBioscience	Cat#: 13-0112-82; RRID:AB_466359
Anti-mouse CD11c Biotin	eBioscience	Cat#: 14-0114-82; RRID:AB_467115
Anti-mouse CD138 purified	BD	Cat#: 553712; RRID:AB_394998
Anti-mouse CD138 APC	BD	Cat#:558626; RRID:AB_1645216
Anti-mouse CD138 Biotin	BD	Cat#: 553713; RRID:AB_394999
Anti-mouse CD138 BV421	BioLegend	Cat#: 142508; RRID:AB_11203544
Anti-mouse CD138 PE	BioLegend	Cat#: 142503; RRID:AB_10915989
Anti-mouse CD138 purified	BD	Cat#: 553712; RRID:AB_394998
Anti-mouse CD152 (CTLA) PE/Cy7	Thermo	Cat#: 25-1522-82, RRID:AB_2688105
Anti-mouse CD16/CD32	eBioscience	Cat#: 14-0161-86; RRID:AB_467135
Anti-mouse CD19 AF700	eBioscience	Cat#: 56-0193-82; RRID:AB_837083
Anti-mouse CD19 APC	eBioscience	Cat#: 17-0191-82; RRID:AB_469358
Anti-mouse CD19 APC-eFluor780	eBioscience	Cat#: 47-0193-82; RRID:AB_10853189
Anti-mouse CD19 BV510	BioLegend	Cat#: 115545; RRID:AB_2562136
Anti-mouse CD19 eFluor 450	eBioscience	Cat#: 48-0193-82; RRID:AB_2734905
Anti-mouse CD19 PE	eBioscience	Cat#: 12-0193-82; RRID:AB_657659
Anti-mouse CD25 APC	eBioscience	Cat#: 17-0251-82; RRID:AB_469366
Anti-mouse CD25 eFluor 450	eBioscience	Cat#: 48-0251-82; RRID:AB_10698312
Anti-mouse CD252 (OX40L) Alexa Fluor 674	BioLegend	Cat#: 108809; RRID:AB_2256388
Anti-mouse CD267 (TACI) APC	eBioscience	Cat#: 17-5942-81; RRID:AB_842758
Anti-mouse CD275 (ICOSL) Biotin	eBioscience	Cat#: 104611; RRID:AB_2750466
Anti-mouse CD278 (ICOS) Biotin	eBioscience	Cat#: 13-9942-81; RRID:AB_467001

(*Continued on next page*)

Continued

REAGENT or RESOURCE	SOURCE	IDENTIFIER
Anti-mouse CD279 (PD-1) FITC	eBioscience	Cat#: 11-9985-85; RRID:AB_465472
Anti-mouse CD279 (PD-1) PE/Cy7	eBioscience	Cat# 25-9985-80; RRID:AB_10853672
Anti-mouse CD28 APC	BioLegend	Cat#: 102109; RRID:AB_312874
Anti-human CD3 purified	DCS Innovative Diagnostik-Systeme	Cat#: CI597C01; RRID: N/A
Anti-human CD3 purified	LabVision/Neomarkers	Cat#: RM-9107-S; RRID:AB_149922
Anti-mouse CD366 (Tim-3) Pe/Dazzle594	BioLegend	Cat#: 134014; RRID:AB_2632737
Anti-mouse CD38 APC	eBioscience	Cat#: 104611; RRID:AB_2750466
Anti-mouse CD38 APC/Cy7	BioLegend	Cat#: 102727; RRID:AB_2616967
Anti-mouse CD38 PE/Cy7	BioLegend	Cat#: 102717; RRID:AB_2072892
Anti-mouse CD4 purified	InVivoMAb	Cat#: BE0119; RRID:AB_10950382
Anti-mouse CD4 Biotin	eBioscience	Cat#: 13-0042-82; RRID:AB_466329
Anti-mouse CD4 BV605	BioLegend	Cat#: 100451; RRID:AB_2564591
Anti-mouse CD4 BV711	BioLegend	Cat#: 100549 RRID:AB_2564586
Anti-mouse CD4 PE-Cy7	eBioscience	Cat#: 15-0041-82; RRID:AB_468695
Anti-mouse/rat CD40 purified	eBioscience	Cat#: 14-0402-82; RRID:AB_467228
Anti-mouse CD40 purified	Biolegend	Cat#: 157504; RRID:AB_2814091
Anti-mouse CD40 purified	Leinco Technologies	Cat#: C2825; RRID:AB_2829586
Anti-mouse CD43 Biotin	BD	Cat#: 553269; RRID:AB_2255226
Anti-human/mouse CD44 APCeF780	eBioscience	Cat#: 47-0441-82; RRID:AB_1272244
Anti-human/mouse CD44 PE/Cy7	eBioscience	Cat#: 25-0441-82; RRID:AB_469623
Anti-mouse CD45 purified	BD	Cat#: 553076; RRID:AB_394606
Anti-mouse CD62L BV510	BioLegend	Cat#: 104441 RRID:AB_2561537
Anti-mouse CD69 APC	Thermo	Cat#: 17-0691-80; RRID:AB_1210795
Anti-mouse CD70 PE/Cy7	BioLegend	Cat#: 104611; RRID:AB_2750466
Anti-mouse CD80 APC	eBioscience	Cat#: 17-0801-82; RRID:AB_469417
Anti-mouse CD80 BV650	BioLegend	Catalog # 104732; RRID:AB_2686972
Anti-mouse CD83 PE	eBioscience	Catalog # 12-0831-82; RRID:AB_465758
Anti-mouse CD86 APC	eBioscience	Cat#: 17-0862-82; RRID:AB_469419
Anti-mouse CD86 BV785	BioLegend	Cat#: 105043; RRID:AB_2566722
Anti-mouse/rat CD8a BUV395	BD	Cat#: 565968; RRID:AB_2739421
Anti-mouse/rat CD8a BUV737	BD	Cat#: 612759; RRID:AB_2870090
Anti-mouse CD8a purified	InVivoMAb	Cat#: BE0061; RRID: N/A
Anti-mouse CD8a Biotin	eBioscience	Cat#: 13-0081-82; RRID:AB_AB_466346
Anti-mouse CD8a PE	eBioscience	Cat#: 12-0081-82; RRID:AB_465530
Anti-mouse CD8a PerCP/eF710	eBioscience	Cat#: 46-0081-82; RRID:AB_1834433
Anti-mouse CD9 Biotin	BD	Cat#: 558749; RRID:AB_397103
Anti-mouse CD93 (AA4.1) APC	eBioscience	Cat#: 17-5892-83; RRID:AB_469467
Anti-mouse CD93 (AA4.1) Biotin	eBioscience	Cat#: 13-5892-82; RRID:AB_466767
Anti-mouse CD95 (FAS) Biotin	BD	Cat#: 554256; RRID:AB_395328
Anti-mouse CD95 (FAS) BV421	BD	Cat#: 562633; RRID:AB_2737690
Anti-mouse CD95 (FAS) BV605	BD	Catalog # 740367; RRID:AB_2740099
Anti-mouse CD95 (FAS) BV650	BD	Catalog # 740507; RRID:AB_2740227
Anti-mouse CD95 (FAS) PE	BD	Catalog # 554258; RRID:AB_395330
Anti-mouse CXCR4 (CD184) BUV395	BD	Cat# 740265; RRID:AB_2740007
Anti-mouse EOMES APC	Thermo Fisher	Cat# 17-4875-82; RRID:AB_2866428
Anti-mouse FASL purified	InVivoMAb	Cat#: BE0319; RRID:AB_2819046
Anti-mouse/rat Foxp3 PE	eBioscience	Cat#: 12-5773-82; RRID:AB_465936
Anti-mouse GPIbβ-X488	Emfret	Cat#: X488; RRID:AB_2890921

(*Continued on next page*)

Continued

REAGENT or RESOURCE	SOURCE	IDENTIFIER
Anti-mouse/human/rat IBA1 purified	FUJIFILM Wako	Cat#: 019-19741; RRID:AB_839504
Anti-mouse IgA Biotin	BD	Cat#: 556978; RRID:AB_396543
Anti-mouse IgA PE	eBioscience	Cat#: 12-5994-81; RRID:AB_466115
Anti-mouse IgD Biotin	eBioscience	Cat#: 13-5993-82; RRID:AB_466860
Anti-mouse IgD eFluor 450	eBioscience	Cat#: 15361820; RRID:AB_1272202
Anti-mouse IgE BV510	BD	Cat#: 747734; RRID:AB_2872207
Anti-mouse IgG Biotin	Vector Laboratories	Cat#: BA-9200; RRID:AB_2827937
Anti-mouse IgG HRP Conjugate	Southern Biotech	Cat#: 41030-05; RRID: N/A
Anti-mouse IgG-Fc Fragment HRP Conjugate	Bethyl Laboratories	Cat#: A90-131P; RRID:AB_67175
Anti-rat IgG	Vector Laboratories	Cat#: AI-4001; RRID:AB_2336209
Anti-goat IgG	Vector Laboratories	Cat#: AI-5000; RRID:AB_2336125
Anti-mouse IgG1 FITC	BD	Cat#: 553443; RRID:AB_394862
Anti-mouse IgG2a BV605	BD	Cat#: 564024; RRID:AB_2738549
Anti-mouse IgG3 BV421	BD	Cat#: 565808; RRID:AB_2739364
Anti-mouse IgM PE/Cy7	eBioscience	Cat#: 25-5790-81; RRID:AB_469654
Anti-mouse IgM PerCP	Dianova	Cat#: 115-126-075; RRID:AB_2338639
Anti-mouse IgM Super Bright 780	eBioscience	Cat#: 78-5790-82; RRID:AB_2735061
Anti-mouse IgM, μ chain specific AffiniPure	Jackson ImmunoResearch	Cat#: 115-005-020; RRID:AB_2338450
Anti-mouse IRF4 purified	Santa Cruz	Cat#: sc-6059; RRID: AB_2127145
Anti-human/mouse/rat IRF4 purified	Santa Cruz	Cat#: sc-48338; RRID:AB_627828
Anti-human/mouse IRF4 eFluor 450	eBioscience	Cat#: 48-9858-82; RRID:AB_2574135
Anti-human/mouse IRF4 PerCP-eFluor 450	eBioscience	Cat# 46-9858-80; RRID:AB_2573911
Anti-human/mouse/rat Ki-67 purified	Abcam	Cat#: ab16667; RRID:AB_302459
Anti-human/rat Ki-67 purified	Lab Vision	Cat#: RM9106; RRID:AB_2341197
Anti-mouse/human Mac-2 (Galectin-3) purified	BioLegend	Cat#: 125402; RRID:AB_1134238
Anti-mouse MHCI eF450	eBioscience	Cat#: 48-5958-82; RRID:AB_10804025
Anti-mouse MHCII (I-A/I-E) PE	eBioscience	Cat#: 12-5321-82; RRID:AB_465928
Anti-mouse MHCII AF700	BioLegend	Cat#: 107621; RRID:AB_493726
Anti-mouse NK1.1 BUV395	BD	Cat#: 564144; RRID:AB_2738618
Anti-mouse NK1.1 BV650	BioLegend	Cat#: 108736; RRID:AB_2563159
Anti-human/mouse/rat Pax5 purified	NeoMarkers	Cat#: RB-9406-P; RRID:AB_721785
Anti-human/mouse Pax5	BioLegend	Cat#: 649710; RRID:AB_2562573
Anti-mouse TACI/TNFRSF13B PE	R&D	Cat#: FAB1041P; RRID:AB_2271808
Anti-mouse TCRβ Biotin	eBioscience	Cat#: 13-5961-82; RRID:AB_466819
Anti-mouse TCRβ BV510	BioLegend	Cat#: 109234; RRID:AB_2562350
Anti-mouse TCRβ BV605	BD	Cat#: 562840; RRID:AB_2687544
Anti-mouse TCRβ PE	eBioscience	Cat#: 12-5961-82; RRID:AB_466066
Anti-mouse Ter119 Biotin	eBioscience	Cat#: 13-5921-82; RRID:AB_466797
Anti-mouse Thy1 purified	Absolute Antibody	Cat#: Ab00212-2.0; RRID: N/A
Purified Armenian Hamster Isotype Control Antibody	BioLegend	Cat#: 400985; RRID: N/A
Streptavidin BUV395 Conjugate	BD	Cat#: 564176; RRID:AB_2869553
Streptavidin BV650 Conjugate	BioLegend	Cat#: 405231; RRID: N/A
Streptavidin eFluor 450 Conjugate	eBioscience	Cat#: 48-4317-82; RRID:AB_10359737
Streptavidin PE-Cy7 Conjugate	eBioscience	Cat#: 25-4317-82; RRID:AB_10116480
Streptavidin PerCP-Cy5.5 Conjugate	eBioscience	Cat#: 45-4317-82; RRID:AB_10311495
Chemicals, peptides, and recombinant proteins		
2-mercaptoethanol	Gibco	Cat#: 31350-010
2-mercaptoethanol	Merck	Cat#: 8.05740-0250

(*Continued on next page*)

Continued

REAGENT or RESOURCE	SOURCE	IDENTIFIER
7-Aminoactinomycin D (7-AAD)	eBioscience	Cat#: 00-6993-50
ACK Lysing Buffer	Gibco	Cat#: A1049201
Alkaline phosphatase	Roche	Cat#: 10713023001
BSA	Carl-Roth	Cat#: 0163.4
BSA HyClone	GE Healthcare	Cat#: SH30574.02
Celltrace™ Violet Cell Proliferation Kit	Thermo Scientific	Cat#: C34571
Cytofix/Cytoperm Fixation solution	BD	Cat#: 554722
Dulbecco's phosphate buffered saline (DPBS)	Gibco	Cat#: 14190-169
Dulbecco's phosphate buffered saline (DPBS), 10x	Gibco	Cat#: 14200075
EDTA, 0.5M	Promega	Cat#: 0000142515
UltraPure™ 0.5M EDTA, pH 8.0	Invitrogen	Cat#: 15575020
Eosin	Dako	Cat#: CS70130-2
Fetal Bovine Serum (FBS)	Gibco	Cat#: 10270-106
Fetal Bovine Serum (FBS)	Sigma	Cat#:
Fetal Bovine Serum (FBS)	PAN-Biotech	Cat#: P30-3032
Hematoxylin	Dako	Cat#: CS70030-2
Heparin	Sigma-Aldrich	Cat#: 9041-08-1
HEPES, 1M	Gibco	Cat#: 15630-056
iFluor® 840 maleimide	AAT Bioquest	Cat#: 1402
Imject™ Alum Adjuvant	Thermo Scientific	Cat#: 77161
L-Glutamine	Gibco	Cat#: 25030-081
Lipopolysaccharide (LPS)	Sigma-Aldrich	Cat#: L2630
LIVE/DEAD™ Fixable Near-IR Dead Cell Stain Kit	Invitrogen	Cat#: L10119
Mouse Albumin	Sigma-Aldrich	Cat#: A3139
Mouse Albumin	Sigma-Aldrich	Cat#: 126674
Non-essential amino acids (NEAA)	Invitrogen	Cat#: L10119
NP-CGG (Chicken Gamma Globulin), Ratio 20-29	Biosearch Technologies	Cat#: N-5055C
Ovalbumine (OVA)	Sigma-Aldrich	Cat#: S7951
p-Nitrophenyl Phosphate	Roche	Cat#: 10004847101
Penicillin-Streptomycin	Gibco	Cat#: 15140122
Perm/wash buffer	BD	Cat#: 554723
Percoll PLUS	Cytiva	Cat#: 89428-528
Cultrex® Poly-L-Lysine	Trevigen	Cat#: 3438-200-01
PromoFluor-840, maleimide (fixable live-dead dye)	BioConnect	Cat#: PK-PF840-3-01
Recombinant Human BAFF	Peprotech	Cat#: 310-13
Recombinant Murine IL-2	Peprotech	Cat#: 210-12
Recombinant Murine IL-21	Peprotech	Cat#: 210-21
Recombinant Murine IL-4	Peprotech	Cat#: 214-14
RetroNectin Recombinant Human Fibronectin Fragment	Takara Bio	Cat#: T100B
Maxima Reverse Transcriptase	Thermo Scientific	Cat#: EP0742
RLT Buffer	Qiagen	Cat#: 79216
Roti®-Histofix 4 %	Carl Roth	Cat#: P087.4
RPMI medium 1640	Gibco	Cat#: 21875-034
Sodium Chloride (NaCl)	Carl Roth	Cat#: 3.957
Sodium pyruvate	Gibco	Cat#: 11360-039
TCL Buffer, 2x	Qiagen	Cat#: 1070498
Tris	Carl-Roth	Cat#: 5429.2
Trypan Blue 0.4%	Gibco	Cat#: 15250061

(*Continued on next page*)

Continued

REAGENT or RESOURCE	SOURCE	IDENTIFIER
Critical commercial assays		
ANA Screen 8 ELISA	IBL International	Cat#: RE75421
ReCombi ANA Screen	Varelisa	Cat#: 125 96
Annexin V apoptosis detection kit (APC)	eBioscience	Cat#: 88-8007-72
Cardiolipin IgG ELISA	IBL International	Cat#: RE70511
Cardiolipin Screen ELISA	IBL International	Cat#: RE70501
CaspGLOW™ Fluorescein Active Caspase Staining Kit	BioVision	Cat#: K180; Abcam Cat#: ab65611
CaspGLOW™ Red Active Caspase Staining Kit	BioVision	Cat#: K190; Abcam Cat#: ab65616
Chromium Next GEM Chip G Single Cell Kit, 16rxns	10x Genomics	Cat#: 1000127
Chromium Next GEM Single Cell 3' GEM, Library & Gel Bead Kit v3.1, 16 rxns	10x Genomics	Cat#: 1000121
Creatinine FS kit	DiaSys	Cat#: 117119910021
Foxp3/Transcription Factor Staining Buffer Set	eBioscience	Cat#: 00-5523-00
GeneChip™ Mouse Genome 430A 2.0 Array	Affymetrix	Cat#: 900498
High Sensitivity DNA Kit	Agilent	Cat#: 5067-4626
Legendplex custom produced panel (IFNα, IFNβ, IL-1α, IL-1β, IL-3, IL-7 IL-9, IL-18, IL-21, IL-22, IL-27, IL-33)	BioLegend	no Cat#
Legendplex Mouse B cell Panel Standard	BioLegend	Cat#: 740831
MicroBeads Anti-Biotin	Miltenyi Biotec	Cat#: 130-090-485
MicroBeads Anti-PE	Miltenyi Biotec	Cat#: 130-048-801
Mouse Albumin Quantitation Set	Bethyl Laboratories	Cat#: E99-134
Mouse BAFF/BLyS/TNFSF13B Quantikine ELISA Kit	R&D Biosystems	Cat#: MBLYS0
Mouse IgA ELISA Kit	Bethyl Laboratories	Cat#: E99-103
Mouse IgG ELISA Kit	Bethyl Laboratories	Cat#: E90-131
Mouse IgG1 ELISA Kit	Bethyl Laboratories	Cat#: E90-105
Mouse IgG2b ELISA Kit	Bethyl Laboratories	Cat#: E90-109
Mouse IgG2c ELISA Kit	Bethyl Laboratories	Cat#: E90-136
Mouse IgG3 ELISA Kit	Bethyl Laboratories	Cat#: E90-111
Mouse IgM ELISA Kit	Bethyl Laboratories	Cat#: E99-101
NEBNext® Ultra™ II FS kit	New England Biolabs	Cat#: E6177L
Pan B Cell Isolation Kit, mouse	Miltenyi Biotec	Cat#: 130-095-813
Pierce™ BCA Protein Assay Kit	Thermo Scientific	Cat#: 23227
PrimeFlow™ RNA Assay Kit	Invitrogen	Cat#: 88-18005-210
PromoFluor-840, NIR maleimide	BioConnect	Cat#: PK-PF840-3-01
RNase-free DNase set	Qiagen	Cat#: 79254
RNeasy Plus Micro Kit	Qiagen	Cat#: 74034
RNeasy Plus Mini Kit	Qiagen	Cat#: 74134
Serin-Prothrombin IgG/IgM ELISA	IBL International	Cat#: RE70611
Single Index Kit T Set A, 96 rxn	10x Genomics	Cat#: 1000213
Sm-Ak ELISA	IBL International	Cat#: RE75221
ssDNA ELISA Screen	IBL International	Cat#: RE70231
Urea FS kit	DiaSys	Cat#: 131019990314
Deposited data		
Raw data files for bulk RNA sequencing: NIK^{pos} Follicular B cells	This paper	ENA: PRJEB58057
Raw data files for bulk RNA sequencing: NIK^{pos} Plasma cells	This paper	ENA: PRJEB58058
Raw data files for single cell RNA sequencing	This paper	ENA: PRJEB81204
Raw data files for Affymetrix gene array	This paper	GEO: GSE280298

(*Continued on next page*)

Continued

REAGENT or RESOURCE	SOURCE	IDENTIFIER
Experimental models: Organisms/strains		
B-Nik^{tg}: C57BL/6-Gt(ROSA)26Sortm6(Map3k14)Rsky/J	Sasaki et al.[41]	N/A
A20$^{F/F}$: Tnfaip3tm1.1Gvl	Vereecke et al.[74]	N/A
A20$^{F/F}$: Tnfaip3tm1.1Lpq	Nakagawa and Rathinam[73,102]	N/A
BCL6^{tg}: IμHABCL6	Cattoretti et al.[29]	N/A
B-BclxL^{tg}: Tg(Emu-BCL2L1)87Nnz	Grillot et al.[75]	N/A
CD19-Cre: B6.129P2(C)-Cd19tm1(cre)Cgn/J	Rickert et al.[76]	N/A
Cγ1-Cre: B6.129P2(Cg)-Ighg1tm1(cre)Cgn/J	Casola et al.[77]	N/A
Aid-Cre: B6.129P2-Aicdatm1(cre)Mnz/J	Robbiani et al.[103]	N/A
MyD88$^{F/F}$: Myd88 tm1.1Medz	Schenten et al.[86]	N/A
CD3e$^{-/-}$: CD3e<tm1Mal>	Malissen et al.[78]	N/A
Baff^{tg}: Tg(Tnfsf13b)1Fma	Mackay et al.[38]	N/A
Perf1$^{-/-}$: C57BL/6-Prf1tm1Sdz/J	Kägi et al.[79]	N/A
Oligonucleotides		
J558Fr3:	Integrated DNA Technologies (IDT)	N/A
5′-CAGCCTGACATCTGAGGACTCTGC-3′	–	N/A
JH4Hint:	IDT	N/A
5′-CTCCACCAGACCTCTCTAGACAGC-3′	–	N/A
A-Key:	IDT	N/A
5’-CGTATCGCCTCCCTCGCGCCATCAG-3’	–	N/A
B-Key:	IDT	N/A
5’-CTATGCGCCTTGCCAGCCCGCTCAG-3’	–	N/A
JH1/4:	IDT	N/A
5’-CTTACCTGAGGAGACGGTGAC-3’	–	N/A
JH2/3:	IDT	N/A
5’-AGGACTCACCTGAGGAGAC-3’	–	N/A
JH2:	IDT	N/A
5’-AGGACTCACCTGCAGAGAC-3’	–	N/A
Vkdeg:	–	N/A
5’-GCTGCAGSTTCAGTGGCAGT GGRTCWGGRAC-3’	–	N/A
Jk2AR:	IDT	N/A
5’-TTAGACTTAGTGAACAAGAGTTGAGAA-3’	–	N/A
Jk5BR:	IDT	N/A
5’-CGTCAACTGATAATGAGCCCTCTC-3’	–	N/A
MsVhe AH:	IDT	N/A
5’-TCGAGTTTTTCAGCAAGATGA GGTGCAGCTGCAGGAGTCTGG-3’	–	N/A
Jh4:	IDT	N/A
5’-CTGAGGAGACGGTGACTGAGG-3’	–	N/A
MsVhe AH_short (sequencing primer)	Eurofins Genomics EU	N/A
5’-TCAGCAAGATGAGGTGCAGC-3’	–	N/A
Vkdeg_short (sequencing primer)	Eurofins Genomics EU	N/A
5’-TTCAGTGGCAGTGG-3’	–	N/A
Software and algorithms		
GraphPad Prism v7-10	GraphPad Software	https://www.graphpad.com
FlowJo v10	FlowJo	https://www.flowjo.com
DESeq2 v1.30.1	Bioconductor;Love et al.[104]	https://doi.org/10.18129/B9.bioc.DESeq2

(*Continued on next page*)

Continued

REAGENT or RESOURCE	SOURCE	IDENTIFIER
GSEA v4.1.0	Broad Institute, Inc., MIT; Subramanian et al.[94]	http://www.gsea-msigdb.org
ImageJ v1.51	National Institutes of Health (NIH)	https://imagej.nih.gov
R (v 4.2.1 or v 3.4.4)	The R Foundation	https://www.r-project.org
Lasergene	DNASTAR	https://www.dnastar.com/software/lasergene
Geneious Prime	Dotmatics	https://www.geneious.com
Photoshop	Adobe	https://www.adobe.com/products/photoshop
ImageScope (v12.4.3.4008)	Leica Biosystems	https://www.leicabiosystems.com
Python (v.3.9.7)	Python Software Foundation	Python (v.3.9.7)
Scanpy toolkit (v 1.8.2)	Python Software Foundation	https://pypi.org/project/scanpy
Seaborn data visualization (v.0.11.2)	Python Software Foundation	https://pypi.org/project/seaborn/
bbknn package (v 1.5.1)	Python Software Foundation	https://pypi.org/project/bbknn
Leiden algorithm (v 0.8.8)	Python Software Foundation	https://pypi.org/project/leidenalg
CellRanger (v 6.0.0)	10x Genomics	https://support.10xgenomics.com
LIMMA	Bioconductor; Ritchie et al.[92]	https://doi.org/10.1093/nar/gkv007
ROAST	Wu et al.[93]	https://rdrr.io/bioc/limma/man/roast.html
Drop-seq (v1.12)	Macosko et al.[83]	https://github.com/broadinstitute/Drop-seq/releases
affy package (v 3.16)	Bioconductor; Gautier et al.[95]	https://www.bioconductor.org/packages/release/bioc/html/affy.html
Gene annotation Release M25 (GRCm38.p6) and Genome sequence	Gencode Consortium	https://www.gencodegenes.org/mouse/release_M18.html
Other		
Anti-mouse Gzmk AF568 PrimeFlow Probe	Thermo Fisher	AssayID: VB10-3285985-PF; Cat#: PF-210
Anti-mouse Gzmb AF568 PrimeFlow Probe	Thermo Fisher	AssayID: VB10-3282422-PF; Cat#: PF-204
Anti-mouse Perforin1 AF568 PrimeFlow Probe	Thermo Fisher	AssayID: VB10-3287008-PF; Cat#: PF-210
Microvette 500	Sarstedt	Cat#: 20.1343.100
MicroWell™ 96-Well Plates (V-Bottom, conical)	Nunc	Cat#: 249570
Cell Strainer with 35μm nylon mesh	Corning	Cat#: 352235
MaxiSorp™ 96-Well Flat Bottom ELISA plates	Nunc	Cat#: 44-2404-21
Agencourt AMPure XP magnetic beads	Beckman Coulter	Cat#: 10453438
Multiscreen HTS 96 HV Filter Plate	Millipore	Cat#: MSHVN4B10

EXPERIMENTAL MODEL AND SUBJECT DETAILS

Mice

Control mouse cohorts always contained appropriate Cre controls, also in case of transgene control cohorts. C57BL/6-*Gt(ROSA)26Sor*$^{tm6(Map3k14)Rsky}$/J (B-Nik$^{tg\ 41}$), *Tnfaip3*/A20 conditional knockout mice on a mixed C57BL/6x129Sv genetic background (*Tnfaip3*$^{tm1.1Lpq}$, A20$^{F/F}$[73]: for Figures 1A–1C and S1A–S1E), *Tnfaip3*$^{tm1.1Gvl}$(A20$^{F/F}$[74]: for all other figures), Iμ*HABCL6*,[29] Tg(Emu-BCL2L1)87Nnz (B-BclxL^{tg}[75]), B6.129P2(C)-*Cd19*$^{tm1(cre)Cgn}$/J (CD19-Cre[76]), B6.129P2(Cg)-*Ighg1*$^{tm1(cre)Cgn}$/J (Cγ1-Cre[77]) and B6.129P2-*Aicda*$^{tm1(cre)Mnz}$/J (AID-Cre[103]) mice were published and provided by the authors. *CD3e*^{tm1Mal}(CD3ε$^{-/-}$[78]) were provided by Bernard Malissen and Tg(Tnfsf13b)1Fma mice (BAFF-transgenic, Baff^{tg}[38]) by Susan Kalled and Jeffrey L. Browning. Baff^{tg} were employed as single copy transgene, as opposed to many other studies where homozygous Baff^{tg} mice were analyzed. Baff^{tg} mice develop B cell hyperplasia, but the occurrence of autoimmune pathology strongly differs between genetic backgrounds, hygiene and microbiome status. Male Baff^{tg} mice produce significantly more BAFF (over 10-fold) compared to females, most likely resulting from sexual dimorphism in expression in the kidneys of the α1-antitrypsin (AAT) driven BAFF transgene.[39] In our cohort, female Baff^{tg} mice had a shorter lifespan compared to female controls and developed glomerular pathology (Figures 3C and S3D), however, they did not produce higher IgG ANA nor α-CL antibodies levels compared to control mice (Figures 3B and S3C). Wild-type C57BL/6J and C57BL/6-*Prf1*^{tm1Sdz}/J (Perf1$^{-/-}$)[79] mice are from the Jackson Laboratory.

All the mice used in this project were housed in a specific pathogen-free (SPF) or specific and opportunistic pathogen free (SOPF) condition, according to the legislation of the European Union and the Region of Upper Bavaria. Mice were bred and housed in mouse facilities in the Max-Planck institute of Biochemistry, Charles River Calco (Italy), in the Center for Preclinical Research of the MRI (Zentrum für Präklinisches Forschung (ZPF), Munich) and mouse facility at the Faculty of Medicine, University of Rijeka, Croatia. Except for crosses involving $A20^{F/F}$[73] mice, all the mouse strains used in this project were generated on or later backcrossed to a C57BL/6 genetic background. All animal procedures were approved by the Regierung of Oberbayern, the University of Rijeka Medical Faculty Ethics Committee and Croatian Ministry of Agriculture, Veterinary and Food Safety Directorate or the Columbia University Institutional Animal Care and Use Committee and conducted in accordance with the international guidelines for animal care and experimental use.

METHOD DETAILS

Organ collection and fixation or single cell suspension generation

Spleens, lymph nodes, Peyer's patches, livers, kidneys, salivary glands and bones (femurs) were collected, placed in a tube containing CB buffer (PBS + 2% FBS (Gibco), 0.4% EDTA (Invitrogen)) and kept on ice.

For FACS analysis blood was aspirated with a syringe from the heart directly after euthanasia or living mice were bled through puncturing the facial vein. The blood was then transferred to a 50 ml tube or microtube containing 50 μl of heparin (20 U/ml), mixed and diluted with 20 ml or 2 ml of CB buffer. For serum generation blood was aspirated with a syringe from the heart directly after euthanasia. The blood was then placed in a 0.5 ml microvette (Sarstedt) inverted and incubated for 30 - 60 minutes at room temperature. Tubes were centrifuged at 10000 rpm for 10 minutes in a microcentrifuge, serum was carefully aspirated and transferred to a new tube.

For generation of single cell suspensions, spleens, lymph nodes and Peyer's patches were dissociated between two microscopic glass slides. The single cell suspension was resuspended in CB buffer and filtered. Bones were flushed with medium (RPMI-1640, 10% FBS (Gibco), 10 mM HEPES (Gibco), 2 mM L-glutamine (Gibco), 1 mM sodium pyruvate (Gibco), 0.1 mM non-essential amino acids (Gibco), 0.05 mM 2-mercaptoethanol (Gibco), Penicillin/Streptomycin (Gibco)) or CB buffer to extract bone marrow cells.

To lyse erythrocytes from organ single cell suspensions and blood samples, after centrifugation and resuspending in 1 ml CB buffer, 5 ml of Gey's solution or ACK lysing buffer (Gibco), respectively, was added and incubated for 5 minutes on ice. The solution was neutralized through addition of 20 ml CB buffer. Only for blood, samples were centrifuged and the procedure was repeated. Living cells were counted using a Neubauer counting chamber and Trypan Blue (Gibco).

Flow cytometry

One to eight million cells were stained in 96 well V-bottom plates (Nunc) for flow cytometry analyses. First, cells were washed twice with PBS and stained with Live/Dead™ Fixable Near-IR dead cell staining kit (Invitrogen) or fixable live-dead dye iFluor™ 840 maleimide (BioConnect, AAT Bioquest) and anti-mouse CD16/CD32 monoclonal antibodies, used for blocking the unspecific binding of antibodies to Fc receptors (25 min, 4°C). Cells were then washed with FACS buffer (DPBS (Gibco), 0.5% BSA (GE Healthcare), 0.1% NaN3, 2μM EDTA (Invitrogen)) and stained with fluorochrome-labeled or biotinylated primary antibodies binding extracellular markers (15 min, 4°C). All antibodies are listed in the key resources table.

In the case of biotinylated antibodies, a 2-step staining was performed. The samples were incubated with biotinylated antibodies (15 min, 4°C), washed with FACS buffer and subsequently stained with the extracellular marker antibody mixture containing a streptavidin coupled fluorochrome.

For intracellular staining cells were then washed and fixed with either Foxp3/Transcription Factor Staining Buffer Set (eBioscience, 30 min or overnight, 4°C) or with a solution of 2% Roti®-Histofix (Carl-Roth, 45min, 4°C). After the incubation time, cells were washed with Permeabilization Buffer (eBioscience) and blocked with anti-mouse CD16/CD32 monoclonal antibodies (15 min, 4°C). After washing with Permeabilization Buffer (eBioscience), samples were stained with fluorochrome-labeled or biotinylated antibodies binding intracellular markers (1 hour, 4°C), washed with FACS buffer and stored in the fridge. In case of Roti®-Histofix fixation, the cells were stained intracellularly overnight.

For staining of apoptotic cells, the CaspGlow active caspase staining kit (fluorescein or red, BioVision) was combined with 7-AAD (eBioscience) and the Annexin V apoptosis detection kit (APC, eBioscience) and stainings were performed according to manufacturers' instructions.

Samples were acquired in BD FACS Canto™, Beckman Coulter CytoFLEX S™ or CytoFLEX LX™ flow cytometers.

RNA flow cytometry (PrimeFlow)

RNA flow cytometry was performed using the PrimeFlow™ RNA Assay (Invitrogen) according to the manufacturer's instructions. Briefly, 5 to 10 million cells were transferred to a 96 well V-bottom plate and stained with fixable live-dead dye, blocked with anti-mouse CD16/CD32 monoclonal antibody and subsequently stained for extracellular markers as described above. Cells were then fixed and permeabilized with the respective buffers according to manufacturer's protocol, and stained for intracellular markers for 30 min at 4°C. Following additional fixation, hybridization of the target probes Granzyme K-AF568, Granzyme B-AF568 or Perforin1-AF568 (Thermo Fisher) was performed according to the manufacturer's protocol with a Thermomix with 96-well plate

adapter and the plate was subsequently stored in the fridge overnight. The following day, signal amplification was performed according to the manufacturer's protocol. Samples were acquired with a Beckman Coulter CytoFLEX LX™ flow cytometer.

Flow-cytometry based purification of cells

For bulk RNA sequencing target cells were sometimes pre-enriched by AutoMACS Pro (Miltenyi) positive or negative selection. The enriched fraction was subsequently stained with extracellular marker antibodies according to the sorting panel. Cells were then re-suspended in a solution of FACS Buffer containing the live-dead dye 7-AAD (eBioscience) and 35 μm nylon mesh (Corning). The sorting was performed with a BD FACS Aria™ II, BD FACS Aria™ III or BD FACS Aria™ Fusion. Per sample 1000 cells were sorted into each well of a 96-well PCR plate pre-filled with 5μl RLT lysis buffer. When possible, 3 wells (technical replicates) were sorted for each population. Plates were then sealed, centrifuged and stored at -80°C.

For bulk RNA sequencing of B-BclxL^{tg} cells and controls, splenocytes were stained with LIVE/DEAD fixable Near-IR dye (Invitrogen) and anti-mouse CD16/CD32 monoclonal antibody (eBioscience) on ice for 30 minutes. Cells were then washed with FACS buffer, stained with the fluorochrome-labeled antibody mix, and washed again in FACS buffer. The stained single cell suspension was then filtered through a 35 μm nylon mesh (Corning) and sorted for single, living follicular B cells (CD138$^-$ TCRβ$^-$ B220$^+$ CD19$^+$ CD38$^+$ CD95^{low}), germinal center B cells (CD138$^-$ TCRβ$^-$ B220$^+$ CD19$^+$ CD38^{low} CD95^{high}) and plasmacytic cells (CD138$^+$ B220$^-$) in the BD FACSAria™ II. Per sample 1000 cells were sorted into each well of a 96-well PCR plate pre-filled with 5μl RLT lysis buffer (Qiagen). Whenever possible, two wells (technical replicates) were sorted for each population. Plates were then sealed, centrifuged and stored at -80°C.

For bulk RNA sequencing of CD3ε$^{-/-}$ B-Nik^{tg} cells and controls, splenocytes were stained with LIVE/DEAD fixable Near-IR dye (Invitrogen) and anti-mouse CD16/CD32 monoclonal antibody (eBioscience) on ice for 30 minutes. Cells were then washed with CB buffer with 2μM EDTA (Gibco), stained with the fluorochrome-labeled antibody mix, and washed again in CB buffer with 2μM EDTA (Gibco). The stained single cell suspension was then filtered through a 35 μm nylon mesh (Corning) and sorted for single, living mature follicular B cells (CD138$^-$ B220$^+$ AA4.1^{low} CD21$^{int/low}$ CD1d$^{int/low}$ eGFP$^+$ and eGFP$^-$ for controls) and plasmacytic cells (CD138$^+$ B220$^-$ eGFP$^+$) in the BD FACSAria™ III machine. Sorted cells were spun and lysed with an adequate amount of RLT lysis buffer (Qiagen) according to the manufacturer's instruction. A lysate volume equivalent to 1000 cells was used for bulk RNA sequencing.

For scRNA sequencing cells were stained with LIVE/DEAD fixable Near-IR dye (Invitrogen) on ice and filtered through a 35 μm nylon mesh (Corning). Next, the stained cell-suspension was sorted for single, living cells in a BD FACSAria™ III machine. Sorted cells were stained with trypan blue (Gibco) and counted using a Neubauer counting chamber. Subsequently, 24,000 cells were centrifuged for 2 minutes at 2200 rpm, resuspended in 100 μl FACS buffer, and transferred to a 96-well plate for single-cell RNA-library construction.

Tumor phenotype

Single cell suspensions were stained as described above and acquired with a Beckman Coulter CytoFLEX LX™ flow cytometer. The relative expression of markers on tumorigenic B cells was assessed for each sample by classifying the signal intensity measured by flow cytometry as 1 = negative/lower than healthy control, 2 = equal to healthy control, 3 = higher than healthy control. If no healthy control was included in the analysis, signal intensity was classified as 1 = negative/low, 2 = intermediate, 3 = high by educated judgment of histograms. A mean expression value was calculated for each genotype and color coded (white = 1 to dark blue = 3).

ELISA

Serum isotype ELISAs were performed with Mouse Ig ELISA Quantitation kits (Bethyl Laboratories), according to manufacturer's protocol. The OD405 was measured with an enzyme-linked immunosorbent assay (ELISA)–photometer (Spectramax 340; Molecular Devices, Sunnyvale, CA or Spark, TECAN) and antibody concentrations were determined by comparison with a standard curve.

NP-specific antibodies were determined by ELISA as described previously.[80,81] Briefly, microtiter plates were coated with NP-BSA (Biosearch Technologies) or antibodies of known isotype in PBS at 4°C overnight, and subsequently blocked at room temperature for 30 minutes with PBS, 0.5% BSA, 0.01% azide (pH 7.2). Serially diluted serum samples were applied to the wells and incubated at 4°C overnight. The plates were then incubated with a secondary biotinylated anti-Ig antibody at 37°C for 1 hour, followed by the incubation with SA-conjugated alkaline phosphatase (AP; Roche) at room temperature for 30 minutes. The amount of bound AP was detected by incubation with p-nitrophenyl phosphate as substrate (Roche). Following each incubation step, unbound antibodies or SA-conjugated AP was removed by 3 washes with tap water. The OD405 was measured with a photometer (Spectramax 340; Molecular Devices, Sunnyvale, CA), and antibody concentrations were determined by comparison with a standard curve.

The detection of anti-nuclear (ANA), anti-cardiolipin, anti-serin-prothrombin and anti-ssDNA autoantibodies was performed by using commercially available ELISA Kits (Varelisa or IBL/Tecan). For detection of mouse antibodies, a secondary goat anti-mouse IgG-HRP (Southern Biotech) was diluted 1:4000 in Sample Diluent. The incubation of kit standards with secondary antibody and all other steps were performed according to manufacturer's instructions. Absorbance was measured at 450 nm with a plate reader (Spark, TECAN). For ANA and anti-ssDNA, absorbance values of samples were normalized by division through the absorbance value of the kit positive control. For all other autoantibodies, antibody concentrations were determined by comparison with a standard curve.

For detection of antibodies against dsDNA, MaxiSorp ELISA plates (Nunc) were coated with poly-l-lysine (Trevigen) and PBS (ratio 1:1) for 1 hour. Plates were washed with Tris-NaCl (50 mM Tris and 0.14 M NaCl, pH 7.5), and dsDNA from mouse embryonic stem cells was coated in saline-sodium citrate (SSC, pH 7.0) buffer overnight. After blocking with Tris-NaCl, 1% BSA for 30 minutes, diluted samples were added to the plate and incubated for 60 minutes. Sera from 24-week C57BL/6$^{lpr/lpr}$ and 24-week MRL$^{lpr/lpr}$

mice, as well as IgG-poor serum, were used as controls. HRP-conjugated antibody against mouse IgG (Bethyl Laboratories) was used as secondary antibody. Absorbance was measured at 450 nm with a Sunrise plate reader (TECAN).

ELISA based quantification of serum BAFF concentration was performed with Mouse BAFF/BLyS/TNFSF13B Quantikine kit (R&D Biosystems). Samples were diluted 1:10 and the procedure was performed according to the manufacturer's instructions.

Albuminuria

The kidney function of mice from every group was determined by measuring creatinine levels determined by the Jaffe method following the manufacturer's instructions (DiaSys Diagnostic Systems). Albuminuria was determined via Mouse Albumin Quantitation Set (Bethyl Laboratories) as described below and albumin creatinine ratio (ACR) was calculated. Urinary albumin excretion was evaluated by a double-sandwich ELISA. First, 96-well plates were coated with purified goat anti-mouse albumin antibody (Bethyl Laboratories), and plates were incubated overnight at 4°C. After blocking at room temperature in 0.5% BSA in PBS with 0.05% Tween20, urine samples and mouse albumin standard (Sigma-Aldrich) were added on the plate in triplicates and incubated for 2 hours. Mouse urine samples were diluted in serial dilutions ranging from $1:10^2$ to $1:10^7$. As a secondary antibody, HRP-conjugated anti-mouse albumin antibody (Bethyl Laboratories) was used.

Total protein content in urine

Urine was collected into a microtube and urine protein concentration was measured using a Pierce™ BCA Protein Assay Kit (Thermo Scientific).

BUN

Blood urea nitrogen was measured by standard method for quantitative *in vitro* determination of urea on photometric systems following the manufacturer's instructions (DiaSys Diagnostic Systems).

Legendplex assay

Cytokine concentrations in serum were measured using Legendplex™ kits (BioLegend) for B cells or custom produced. Serum samples were diluted 1:2 for all analytes and processed according to manufacturer's instructions.

3' RNA and single cell RNA sequencing

For bulk 3'-sequencing of poly(A)-RNA library preparation was done as described previously.[82] Briefly, frozen cell lysates from sorted cell populations (mature follicular B cells, germinal center B cells or plasma cells) were thawed and RNA was isolated using Agencourt AMPure XP magnetic beads. Barcoded cDNA of each sample was generated with Maxima RT polymerase (Thermo Fisher) using oligo-dT primer containing barcodes, unique molecular identifiers (UMIs) and an adapter. 5' ends of the cDNAs were extended by a template switch oligo (TSO) and full-length cDNA was amplified with primers binding to the TSO-site and the adaptor. NEBNext Ultra II FS kit (NEB) was used to fragment cDNA. After end repair and A-tailing a TruSeq adapter was ligated and 3'-end-fragments were finally amplified using primers with Illumina P5 and P7 overhangs. In comparison to Parekh et al.[82], the P5 and P7 sites were exchanged to allow sequencing of the cDNA in read1 and barcodes and UMIs in read2 to achieve a better cluster recognition. The library was sequenced on a NextSeq 500 (Illumina) with 59 cycles for the cDNA in read1 and 16 cycles for the barcodes and UMIs in read2. Data was processed using the published Drop-seq pipeline (v1.0) to generate sample- and gene-wise UMI tables.[83] Reference genome (GRCm38) was used for alignment. Transcript and gene definitions were used according to the GENCODE version M25.

For single-cell RNA-library construction the Chromium Controller and Chromium Next GEM Single Cell 3' Kit (v3.1) were used according to the manufacturer's protocol (10x Genomics). For quality control, quantification of the concentration and determination of the average fragment size the Agilent High Sensitivity DNA Kit on an Agilent Bioanalyzer 2100 (Agilent) was used. Sequencing of the single index libraries was performed on an Illumina NovaSeq 6000 System (Paired-End 100 Bp S4).

Lymphoma clonality assessment

Immunoglobulin heavy-chain (IGH) amplicon sequencing and Southern Blot for lymphoma clonality

Immunoglobulin heavy chain VDJ rearrangements were PCR amplified essentially as published.[84] Three different amplification reactions were run in which primer VHE was paired with primers JH1/4, JH2/3 or JH2 to yield a product of around 400 Bp. The primers carried adaptors (A, B) and identifier sequences (MID) for amplicon sequencing: A-Key-MID-VHE: 5'-CGTATCGCCTCCCTCGCG CCATCAG-MID-GAGGTGCAGCTGCAGGAGTCTGG-3' and B-Key-MID-JH: 5'-CTATGCGCCTTGCCAGCCCGCTCAG-3' (JH1/4 5'-CTTACCTGAGGAGACGGTGAC-3', JH2/3 5'-AGGACTCACCTGAGGAGAC-3', JH2 5'-AGGACTCACCTGCAGAGAC-3'). Thermal cycler conditions used were: 98°C 3 min, 35 cycles of 98°C for 10 sec, 61°C for 30 sec, 72°C for 30 sec and 72°C for 5 min.

Amplicon sequencing was performed unidirectionally from the A adaptor (GS FLX with Titanium series chemistry) at Eurofins Genomics, Ebersberg. VDJ assignment and mutation rates were determined using the IGMT database (imgt.org/IMGTindex/IMGTHighV-QUEST.php) and Igblast (ncbi.nlm.nih.gov/igblast/).

Southern blotting for lymphoma clonality was performed with EcoRI-digested genomic DNA from splenocytes (Figure S1H) or frozen tissues (Figure S1E) using a JH probe spanning the JH4 exon and part of the downstream intronic sequence.[85]

Immunoglobulin heavy- and light-chain amplification for clonality assessment, followed by direct sequencing

To analyze IGH and IGK rearrangements, three different PCRs were performed on genomic DNA isolated either from dissociated cells or RNA stabilized tissue.

For analysis of IGVκ-IGJκ rearrangements, the thermal cycling conditions used were 94°C for 60 sec, 30 cycles: 94°C for 30 sec, 60°C for 90 sec, 72°C for 90 sec and 72°C for 42 sec (Vkdeg forward primer 5'-GGCTGCAGSTTCAGTGGCAGTGGRTCWGGRAC-3', Jk2AR reverse primer 5'-TTAGACTTAGTGAACAAGAGTTGAGAA-3', or alternatively Jk5BR reverse primer 5'-CGTCAACTG ATAA TGAGCCCTCTC-3').

Amplification of the IgH rearrangements for the different IGHJ gene segments (JH1-JH4) were performed using the following thermal cycler conditions: 98°C for 10 min, 35 cycles of 98°C for 10 sec, 67°C for 30 sec, 72°C for 30 sec and 72°C for 10 min (MsVhe AH forward primer 5'-TCGAGTTTTTCAGCAAGATGAGGTGCAGCTGCAGGAGTCTGG-3', Jh4 reverse primer 5'-CTGAGGAGACGG TGACTGAGG-3').

Based on the results of the above described PCRs, clonality of the B cells of tumors was classified into four different categories: - no evidence for clonality, PCR results similar to wildtype; + (poly)clonal, clear deviation from wildtype but still multiple amplicons detected and no clear dominating amplicon present in more than 1 PCR; ++ (poly)clonal, one clear dominating amplicon present in at least 2 of the 3 PCRs; +++ clonal, BCR sequenced: in order to identify the clonal rearrangements and estimate the extent of somatic hypermutation, IGH and IGK rearrangements were amplified with Q5 high fidelity polymerase. Amplicons representing suspected clones were cut from agarose gels, DNA was purified and sent for bulk sequencing to Eurofin Genomics EU. Sanger sequencing chromatograms were assessed for mixed samples (not clonal), SNPs (oligoclonal or parental/daughter clones) or clear clean single sequences (monoclonal) using Geneious Prime v8 (geneious.com). Consensus sequences from monoclonal samples were generated with at least 2 reads (forward and reverse sequencing primers), exported and annotated using the IMGT/HightV-Quest v 1.9.3 tool (imgt.org), including the IGVH and IGVK identities to germline.

Immunizations

For the analysis of T cell dependent responses in Figure S1A, age-matched 10-16-week-old mice were immunized by intraperitoneal injection of the T-cell dependent antigen sheep red blood cells (SRBC) (Cocalico Biologicals) (n = 500 million/mouse in PBS), followed by analysis after 10 days. Figure 1I: mice were immunized intraperitoneally with OVA/LPS in alum[86]: ovalbumin (100 μg per mouse, OVA, Sigma) and LPS (10 μg per mouse before washes, Sigma) in PBS were emulsified with equal amounts of alum. The OVA/alum/LPS precipitate was washed twice with PBS, which removes most of the LPS. Blood was taken for analysis by tail vein bleeding.

Antibody injections

For depletion of T cells (Figure S7G) , mice were intraperitoneally injected with a mixture of 300μg anti-CD8 (InVivoMab), anti-CD4 (InVivoMab) and anti-Thy1 (Absolute Antibody) antibody, each. Mice were first injected twice within 24 hours and subsequently twice a week for 15 days.

For inhibition of FAS-FASL interaction (Figures 7I and S7L), mice were intraperitoneally injected with 200μg anti-FASL antibody (InVivoMab) twice within 24 hours and subsequently every second day for 7 days. Control mice were injected with equal volume of PBS.

Bone marrow chimeras

BclxL^{tg} competitive BM chimeras (Figures 4I, S4M, and S4N): Bone marrow from CD19Cre BclxL^{tg}, CD19Cre BclxL^{tg} A20$^{wt/F}$ and CD19Cre BclxL^{tg} A20$^{F/F}$ mice was depleted from B, T and plasma cells by magnetic activated cell sorting. Bone marrow cells were labeled with PE conjugated antibodies targeting B220, CD19, TCRβ, CD138, subsequently incubated with anti-PE MicroBeads (Miltenyi, Cat. No. 130-048-801) and purified using an autoMACS® Separator (Miltenyi). Subsequently, equal numbers of bone marrow cells from two donor mice were mixed and 40,000 cells were transplanted into 6 to 8 weeks old sublethally irradiated (4.5 Gy) female Rag2$^{-/-}$ mice by injection into the tail vein. The recipient mice were treated with antibiotics for two weeks (Borgal® 24%, Virbak) diluted 1:250 in drinking water and analyzed 6 to 7 weeks after transplantation. In each pairwise cell mixture, the cells from one donor mouse conditionally expressed a truncated human coxsackie adenovirus receptor (CAR)[43] to enable their identification by flow cytometry. Each genotype was analyzed with and without CAR expression in the pairwise combinations, to address potential effects of the Cre-reporter.

Perforin 1 knockout and control mixed chimeras (Figures 7H and S7K): C57BL/6J mice were lethally irradiated with 9.5 Gy and one day later received 10^6 bone marrow cells previously isolated from CD3ε$^{-/-}$ CD19Cre Nik^{tg} A20$^{F/wt}$ or CD3ε$^{-/-}$ CD19Cre Nik^{tg} A20$^{F/F}$ mice, mixed in 1:1 ratio with bone marrow cells from *Perf1*$^{-/-}$ or control C57BL/6J mice. Recipients were treated with antibiotics (Enroxil 10%; Krka) diluted 1:250 in drinking water for 8–10 days following irradiation. Ten weeks after transplantation mice were bled to check for the B-cell lineage reconstitution and mice were analyzed four weeks later (14 weeks after bone marrow transfer).

Ferric(III)chloride induced thrombus formation in the murine carotid artery model

In anesthetized mice (fentanyl 0.05 mg/kg, midazolam 5.0 mg/kg and medetomidine 0.5 mg/kg i.p.) the right common carotid artery was surgically prepared and vessel injury was induced by application of $FeCl_3$ (1 μL of 10% $FeCl_3$ soaked in 1 mm^2 Whatman paper) for 2 minutes. For intravital microscopy, platelets were labeled by injection of a fluorescently labeled non-blocking platelet antibody (anti-mouse GPIbβ-X488, Emfret, 0.5 μl/g body weight) before application of $FeCl_3$. Vessel injury-induced thrombus

formation was monitored and imaged for 30 minutes by *in vivo* video fluorescence microscopy with a frequency of 1 picture per second (Zeiss Axio Zoom.V16 microscope equipped with a Zeiss AxioCam). Thrombus size was calculated from single images using ImageJ software.

Histopathological analyses

Histological and immunohistochemical analysis of suspected B cell expansions and lymphomas

Histological analysis of mouse organs was performed on 2-4 μm-thick FFPE tissue sections, stained with Hematoxylin & Eosin (Thermo Scientific) as described.[87] The following primary antibodies were used for immunohistochemical analyses: anti-BCL6 (1:300) (N3, rabbit polyclonal, Santa Cruz Biotechnology), anti-PAX5 (1:400) (rabbit polyclonal, Neomarker), anti-CD3 (1:800) (rabbit monoclonal, clone SP7, Neomarker), anti-B220 (1:400) (rat monoclonal, clone RA3-6B2, BD Biosciences), anti-IRF4 (1:200) (M-17, goat polyclonal, Santa Cruz Biotechnologies), and anti-CD138 (1:200) (rat monoclonal, clone 281-2, BD Biosciences) (Figures 1B and 1C). Anti-mouse B220 (BD Pharmingen), anti-mouse CD138 (BD Pharmingen), anti-human CD3 (clone sp7, Innovative Diagnostic System), anti-human/rat Ki67 (Lab Vision, Thermo Fisher Scientific) (Figures S1F and S1G). Anti-mouse BCL6 (Cell Signaling, 1:100), Anti-mouse B220 (BD, 1:50), anti-mouse CD138 (BD, 1:100), anti-mouse/human/rat IBA1 (Wako, 1:500), anti-mouse/human/rat IRF4 (Santa Cruz, 1:1000) or anti-mouse/human/rat Ki-67 (Abcam, 1:50) (Figures 5B, S3M, and S5D). Antibody binding was detected by using the Dako REAL detection system or a polymer refine detection kit without post primary reagent and visualized with DAB as a dark brown precipitate. For primary antibodies derived from species other than rabbits, secondary antibodies were used: rabbit anti rat (Vector Laboratories, 1:400), rabbit anti goat (Vector Laboratories, 1:200). Counterstaining was done with hematoxylin.

Diagnosis of murine lymphoid tumors

Lymphoproliferative diseases developing in the compound Cγ1Cre cohorts (Figures 1B, 1C, and S1E) were diagnosed independently by two hemato-pathologists (G.B. and D.D-S.) based on morphology, phenotype, and clonality according to the following criteria, in analogy to the classification of human lymphoma: i) DLBCL: complete effacement of the lymphoid organ architecture due to the expansion of large cells, with occasional infiltration beyond the capsule into the surrounding soft tissues; expression of GC (BCL6) or post-GC (IRF4) B cell markers, and evidence of clonal IG rearrangements; ii) lymphoproliferative disease (LPD), defined by the initial obliteration of the follicular architecture by cells expressing B220, in the absence of clonal rearrangements. The genotype of the animal was not disclosed to the pathologists. Tissue samples from the remaining cohorts were histopathologically assessed in a blinded fashion by two experienced comparative pathologists (K.S., and M.R.: Figures 1E, S1F, S1G, S3E, S3M, S5D, and S5G) and classified according to the consensus classification of lymphoid neoplasms in mice.[88] The most recent immunohistochemical phenotyping description of rodent lymphoid tissue,[89] and the classification of non-nonproliferative and proliferative lesions of the rat and mouse hematolymphoid system by INHAND (International Harmonization of Nomenclature and Diagnostic Criteria for Lesions in Rat and Mice)[90] were considered: splenic marginal zone B cell hyperplasia (MZBCH) were characterized by small lymphocytes widening and bridging of marginal zones without an occurrence of germinal center hyperplasia. Lymphomas of large B cells (LBL): showed a proliferation of medium- to large sized neoplastic B cells ($CD45R/B220^{+}/CD138^{-}$) with a diffuse growth pattern and either round-to-oval vesicular nuclei containing multiple small nucleoli and a small rim of cytoplasm or nuclei with a single prominent amphophilic nucleolus and abundant cytoplasm. Plasma cell neoplasms were heterogeneous tumors consisting of a mixture of (predominantly) mature and immature plasma cells ($CD45R/B220^{-}/CD138^{+}$), with mainly small nuclei with clumped chromatin, abundant cytoplasm and, frequently, a perinuclear halo as well as rare mitoses. Plasmacytosis/plasma cell hyperplasia was characterized by an increased amount of a morphologically homogeneous population of mature plasma cells, mitoses were absent.

Kidney analysis

Paraffin-embedded kidneys (Figures 2I, S2G, and S3D) were cut into 2 μm thick sections and stained with periodic acid-Schiff (PAS) according to a standard protocol. In brief, re-hydrated sections were incubated for 5 min in 1% (w/v) periodic acid (Merck) followed by washing in distilled water and incubation with Schiff's reagent (Sigma Aldrich) for 5 min. After washing, sections were incubated for 2 min with Mayer's hemalaun (Merck) followed by washing in tap water and dehydration for final covering with Entellan (Merck) and a coverslip. Renal histology changes were examined by light microscopy and assessed at a magnification of 200-400x. A sum score of pathologic changes assessed the presence of each of 7 characteristic glomerular changes in lupus nephritis. One point was given if 1. glomerular basement membrane was thickened, 2. mesangial matrix was enlarged, 3. hypercellularity occurred, 4. intracapillary thrombi were seen, 5. apoptotic cells, 6. extracellular proliferation, or 7. segmental sclerosis occurred, and points were summed up into a glomerular pathology score. Representative photomicrographs were taken using an upright BX60 light microscope with an XC30 camera (Olympus) at 300-fold magnification. Immunostaining for IgG was performed on 2 μm sections using biotinylated anti–mouse IgG (Vector Laboratories, 1:100). The degree of IgG deposition (Figure 2G) was scored semiquantitatively (grade 0 = no trace; grade 1 = mild; grade 2 = moderate; grade 3 = severe) in the mesangium and along the glomerular capillary loops. To assess immune cell infiltration (Figures S2F and S2O), the following antibodies were used: anti-mouse/human Mac2 (BioLegend, 1:3000), anti-mouse CD45 (BD, 1:100) and anti-mouse CD138 (BD Biosciences, 1:100). For quantitative analysis, glomerular cells were counted in 15-20 cortical glomeruli per section (from ''n'' mice in the group, as indicated in a figure) or were quantified using Photoshop CS6 Extended (Adobe) as % of stained high power field (%HPF).

iGB culture and FASL induced killing assay

The *in vitro* derived germinal center B cell (iGB) culture system was previously described.[32] Briefly, one day prior to the start of the iGB culture (day 0), 40LB feeder cells were irradiated (120 Gy, γ-rays) and seeded into petri dishes to form a confluent layer. On day 1,

Naïve B cells were purified from splenocytes by depletion of TCR, CD4, CD8a, CD11b, CD11c, CD43, CD93, CD95 and Ter119 expressing cells using AutoMACS (Miltenyi). Cells were seeded at a density of 20,000 cells/ml onto 40LB feeder layer in iGB medium (RPMI, 10% FBS Gold (GE Healthcare), 10 mM HEPES (Gibco), 2 mM L-Glutamine (Gibco), 1 mM Sodium Pyruvate (Gibco), 0.1 mM non-essential amino acids (Gibco), 0.05 mM 2-Mercaptoethanol (Gibco), Penicillin/Streptomycin (Gibco)), supplemented with 1 ng/ml IL-4 (Peprotech), and incubated at 37°C, 5% CO_2. After 72 hours (day 4) cells were dissociated from the plate by 5 minutes incubation with 37°C warm 2mM EDTA (Invitrogen) in DPBS, centrifuged 1200rpm for 10 minutes and resuspended in iGB medium. B cell numbers were counted and an replated at a density of 20,000 cells/ml onto a new plate with adherent irradiated 40LB feeder cells in iGB medium, supplemented with 10ng/ml IL-21 (Peprotech). The remaining harvested cells were processed for FACS analysis. Subsequently, the iGB cells were dissociated, diluted and re-seeded in IL-21 containing medium every second day until day 10. Theoretical cell numbers per measurement timepoint were calculated, assuming no dilution of iGB cells was being performed. For calculation of theoretical cell numbers, the number of cell divisions (n) of iGB cells between two measurement timepoints (t_1, t_0) was calculated from the cell number increase between two measurement timepoints (N_1, N_0): $n = (\log(N_t) - \log(N_0)) / \log(2)$. The theoretical cell number was then calculated as $N_{1\text{-theor}} = N_{0\text{-theor}} * 2^n$. To assess the sensitivity of iGB cells towards FASL induced cell death, FASL expressing 40LB feeder cells[33] were irradiated (120 Gy, γ-rays) and seeded into petri dishes to form a confluent layer. iGB cells which were previously kept in IL-4 containing iGB medium for 4 or 6 days, were seeded onto FASL expressing 40LB. The fraction of dead 7-AAD stained cells was assessed by flow cytometry after 4, 6, 8 and 20 hours.

In vitro cytotoxic T cell differentiation with primary B cells

Splenocytes from CD3ε$^{-/-}$ B-Nik^{tg}-A20$^{-/-}$, CD3ε$^{-/-}$ and CD19cre mice were depleted from CD11c, NK1.1, F4/80, TCRß, CD4 and CD8 expressing cells by magnetic activated cell sorting (MACS, Miltenyi) to purify B cells. The B cells were then stimulated with 2.5 μg/ml anti-CD40 (Leinco Technologies) for 48 hours and irradiated with 5 Gy. T cells were MACS purified from WT splenocytes using the Pan-T cell isolation kit II (Miltenyi). T cells were then plated with pre-stimulated irradiated B cells at a 1:1.5 and 1:3 ratios in 48-well plates and co-cultured in RPMI 1640 medium (Gibco) supplemented with 10% FBS (Gibco), 10 mM HEPES (Gibco), 2 mM L-glutamine (Gibco), 1 mM sodium pyruvate (Gibco), 0.1 mM non-essential amino acids (Gibco), 0.05 mM 2-mercaptoethanol (Gibco) and 1% Penicillin/Streptomycin (Gibco). For FACS analysis of T cells, co-cultured cells were harvested on day 3.

In vitro killing assays

Assays with primary T cells

T cells from B-Nik^{tg}-A20$^{-/-}$ and WT mice were isolated from splenocytes by MACS (Miltenyi) through positive selection of TCRβ$^+$ cells. TCRβ-depleted splenocytes were further depleted from CD11b, CD11c, F4/80 and NK1.1 expressing cells to obtain B cells. B cells were then stimulated overnight with 2.5 μg/ml anti-CD40 (Clone FGK45, Biolegend), 1 μg/ml hBAFF (Peprotech) and 10 ng/ml IL-4 (Peprotech) and T cells were kept overnight with 100 U/ml IL-2 (Peprotech). The culture medium was RPMI 1640 GlutaMAX™ medium (Gibco) supplemented with 10% FBS (Sigma), 10 mM HEPES (Gibco), 2 mM L-glutamine (Gibco), 1 mM sodium pyruvate (Gibco), 0.1 mM non-essential amino acids (Gibco), 0.05 mM 2-mercaptoethanol (Gibco) and 1% Penicillin/Streptomycin (Gibco). B cells were labeled with 5 μM CellTrace Violet (Thermo Scientific) in 2 % FBS / PBS for 10 minutes at room temperature. T cells were seeded into 96-well V-bottom plates and optionally incubated with 10 μg/ml anti-FASL (InVivoMab) or isotype control antibody (BioLegend) for 15 minutes at 37°C. 10,000 B cells were added to the T cells to achieve final T:B cell ratios of 5:1, 10:1 and 50:1 or seeded without T cells. Co-cultures were incubated for 18 hours at 37°C / 5 % CO_2. Subsequently, cells were stained with anti-CD19-AF700 (eBioscience) and live/dead marker (Promofluor840 maleimide, Bio-Connect) for 10 minutes at room temperature, fixed for 20 minutes (eBioscience, Fix/Perm), stained intracellularly with anti-active Caspase 3-PE (BD Biosciences) and analyzed by flow cytometry. Specific killing is defined as the difference between the fractions of active Caspase 3$^+$ B cells in T:B cell co-cultures and in cultures with only B cells.

Assays with educated T cells (in vitro cytotoxic instruction)

Long-term expanding NIK^{pos}-A20$^{-/-}$ and control iGB cells were generated through enforced Bach2 expression using a pMX-mu-Bach2-IRES-huCD8a retroviral plasmid as described previously.[91] Bach2^{tg} iGB cells were cultured on 40LB feeder[32] with IL-21 as published[91] for no longer than 6 weeks to avoid potential biases due to polyclonal outgrowth. iGB were harvested from the supernatant and adherent iGB cells were then dissociated from the LB40 feeder layer by 5 min incubation of 2 mM EDTA / 2 % FBS / PBS. For *in vitro* T cell cytotoxic T cell differentiation (education) T cells were isolated from splenocytes of wild-type mice by MACS (PanT isolation kit II, Miltenyi) and co-cultured with irradiated (5Gy) Bach2^{tg} NIK^{pos}-A20$^{-/-}$ iGB cells at a 2:1 ratio for 3 days. Subsequently, the irradiated iGB cells were depleted with anti-CD19$^+$ MACS beads and remaining educated T cells were seeded into 96-well V-bottom plates. Target NIK^{pos}-A20$^{-/-}$ and control iGB cells were labeled with 5 μM CellTrace Violet (CTV, Thermo Scientific) in 2 % FBS / PBS for 10 minutes at room temperature and 2,500 CTV$^+$ iGB cells were added to the T cells to achieve final T cell:iGB cell ratios of 5:1, 10:1 and 50:1. Co-cultures were incubated for 4 hours at 37°C / 5 % CO_2. Subsequently, cells were fixed for 20 minutes (BD Biosciences, Fix/Perm), stained intracellularly with anti-active Caspase 3-PE (BD Biosciences) and analyzed by flow cytometry. Specific killing is defined as the difference between the fraction of active Caspase 3$^+$ iGB cells in T:B cell co-cultures and in cultures with only iGB cells.

In vitro stimulation of B cells for RNA gene array analysis

Per biological replicate, splenocytes from three mice were pooled and follicular B cells were enriched by depletion of $CD9^+$ (marginal zone B) and $CD43^+$ (T) cells. 7 million cells were seeded in 1 ml B cell medium (RPMI, 10% FCS (Gibco), 10 mM HEPES (Gibco), 2 mM L-Glutamine (Gibco), 1 mM Sodium Pyruvate (Gibco), 0.1 mM non-essential amino acids (Gibco), 0.05 mM 2-Mercaptoethanol (Gibco), Penicillin/Streptomycin (Gibco)), supplemented with 10 μg/mL anti-IgM (Jackson ImmunoResearch Laboratories, polyclonal), 2.5 μg/ml anti-CD40 (eBioscience, clone HM40–3) or 20 μg/mL lipopolysaccharide (LPS; Sigma-Aldrich) or without supplement. After 3 hours or overnight incubation (14 hours), cells were harvested through pelleting, resuspended in 800μl Trizol and cell lysate was frozen until further processing. RNA was extracted using RNeasy Mini Kit (Qiagen) and eluted in RNAse-free water and analyzed using a GeneChip Mouse Genome 430A 2.0 Array (Affymetrix).

3' RNA and single cell RNA sequencing data analysis

Bulk RNAseq

For bulk RNA sequencing Gencode gene annotations M18 and the mouse reference genome GRCm38 were derived from the Gencode homepage (EMBL-EBI). Dropseq tools v1.12[83] was used for mapping raw sequencing data to the reference genome. The resulting UMI filtered count matrix was imported into R (v 3.4.4). Prior differential expression analysis of bulk RNA data from B-Nik^{tg} mice with Limma,[92] lowly expressed genes were removed from the dataset. Raw count data was CPM scaled data followed by a quantile normalization. Data was modeled using the genotype as explanatory variable and contrasts (pairwise comparisons) of interest were extracted from the model. A gene was determined to be differentially regulated if the adjusted p-value was below 0.01 and the $\log_2$ fold change was above 0.8. $\log_2$ fold changes were used as input for gene set enrichment analysis with compiled marker gene sets using ROAST[93] as implemented in Limma or GSEA[94] v4.1.0 ([build 27], Broad Institute, MIT, University of California) in the preranked mode with default parameters. For principal component analysis the 10 percent most variant (based on standard deviation) genes were selected after quantile normalization and the first two principal components are shown. All heatmaps display z-scaled data after quantile normalization.

Microarray data analysis

Microarray data was processed with the RMA method following quantile normalization as implemented in the affy package.[95] Probeset to gene annotations were downloaded from ENSEMBL GRCm38 v102. Probesets matching to multiple genes were discarded. For genes covered by more than two probesets the probeset with the highest standard variation across all samples was selected for downstream processing. Differential gene expression was analyzed with Limma.

Single Cell RNAseq

For single cell RNA sequencing reads were aligned to the mouse reference genome (mm10, release 108.20200622) using the CellRanger Software (10x Genomics, v 6.0.0). The generated HDF5 data files were imported in Python (v.3.9.7). Quality control and all downstream analyses were performed using the Python-based Scanpy toolkit (v 1.8.2). Subsequently, cells that had less than 1000 or more than 20.000 counts, as well as cells with less than 200 genes and those with a high mitochondrial content (>10%) were filtered out. Counts per-cell normalized and log+1 transformed. For batch correction the bbknn package (v 1.5.1) was applied. Cells were clustered into subgroups using the Leiden algorithm (v 0.8.8) and the number of Leiden clusters was adjusted according to the dataset. Uniform Manifold Approximation and Projection (UMAP) was used for dimensionality reduction. B cell clusters were selected based on CD79a expression and confirmed via CD19. T cell clusters were selected based on the expression of CD3e. To calculate the average expression of a set of genes (score) the *scanpy.tl.score_genes* function was applied, in which the reference gene set is randomly sampled from the gene pool. Annotation of B and T cell populations was performed manually based on a literature-based strategy, whereby gene expression was checked using the Gene Skyline Databrowser (ImmGen). Data on the top 30 differentially expressed genes of each cluster was extracted using the *scanpy.tl.rank_genes_groups* function.

Mutational analysis of follicular lymphoma

Clinical data was available from patients with symptomatic, advanced stage follicular lymphoma (FL) who had been enrolled in previously reported clinical trials: Hiddemann and Cheson[96] (GLSG2000), Marcus et al.,[97] (GALLIUM, NCT01332968)). Targeted DNA next-generation-sequencing (NGS) by hybridization capture (including *TNFAIP3*, *ARID1A* and *FAS*) of diagnostic FL biopsies was available from previously reported studies (Pastore et al.,[48] N = 278 (GLSG2000) and Jurinovic et al.,[47] N = 418 (GALLIUM)). All studies had been approved by relevant institutional regulatory boards in concordance with the Declaration of Helsinki. All patients had signed informed consent which included molecular analyses. TMB (Targeted Mutation Burden) indicates the number of somatic non-silent mutations per sample at allele frequencies $\geq$10% within the full coding regions of all captured genes. Genome-wide copy number alterations were inferred from the available sequencing data utilizing both targeted reads as well as off-target reads (CNVkit 0.9.5).[98] All subsequent analyses were performed with R (v4.2.1). Statistical significance was calculated using a chi-squared test.

Generation of gene lists

Plasma cell and GCB cell identity genes were extracted from Immgen RNA sequencing data using population comparisons as follows: For plasma cell identity genes group A (B_PB_Sp and B_PC_Sp) (ALWAYS) were compared to group B (B_Fo_Sp, B_MZ_Sp, B_GC_CB_Sp, B_GC_CC_Sp) (SOMETIMES). Genes over 30x upregulated in group A were taken. For GCB cell identity genes group A (B_GC_CB_Sp, B_GC_CC_Sp) (ALWAYS) were compared to group B (B_Fo_Sp, B_MZ_Sp, B_PB_Sp, B_PC_Sp) (SOMETIMES). Genes over 20x upregulated in group A were taken.

The activated B cell signature represents 200 genes with the highest significant (padj <0.05) fold change enriched in B cells activated 24h with LPS and anti-CD40 compared to naive B cells.[99] The SLE signature[69] represents genes significantly enriched in a SLE-specific B cell subcluster (B-SC5). For T cell analyses we used: a hand-curated list of genes strongly implicated in cytotoxicity; exhaustion/dysfunction[100]: Figure 7D; genes characterizing stem-like precursors of exhausted cells (Tpex)[45]: Tpex defining genes ("In mice, TPEX cells are defined by the co-expression of PD-1, the transcriptional regulators TCF1 and ID3 and the surface molecules CXCR5 and Ly108") plus Myb; immediate-early TCR-induced genes[101]: Figure 7E.

QUANTIFICATION AND STATISTICAL ANALYSIS

Boxplots extend from the 25th to 75th percentile, individual values are shown as circles and the median is highlighted with a thick line. If only mean values are shown, error bars represent the standard deviation (SD). If not stated otherwise, male and female mice were combined for the analyses. All information on age range, number of individual animals, number of independent experiments and statistical testing employed are listed in Table S1 and/or figure legends.

Briefly, normal distribution of the data was assessed by the Shapiro-Wilk test. If all groups followed a normal distribution, Unpaired t test with Welch's correction or Uncorrected Fisher's LSD for multiple population comparisons were performed. If one or more groups did not follow a normal distribution according to the Shapiro-Wilk test, Kolmogorov-Smirnov test or Uncorrected Dunn's test were performed.

Flow cytometry data was analyzed with FlowJo (v 10). Median Fluorescence Intensity (MFI) of specific markers assessed with flow cytometry was calculated with FlowJo (v 10) for B cell populations. The relative expression was calculated by dividing the MFI of experimental B-cell populations by the MFI of CD19Cre control B cell populations acquired in the same experiment. Relative expression values were transformed to $\log_2$ ($\log_2$ fold change) and the mean depicted in a heatmap.

Mutational analyses of follicular lymphoma were generated with R (v 4.2.1)/R Studio (v 2022.02.1 Build 461). Bulk and single cell RNA sequencing graphs were generated with R (v 4.2.1 or 3.4.4)/R Studio (version 1.3.959). All the other graphs were generated with GraphPad Prism (version 7. 0 to 9.4.1). scRNA seq UMAPs and plots were generated in Python (v 3.9.7) using Scanpy (v 1.8.2). Scatter plots of gene set scores were generated using Seaborn (v 0.11.2).